FACULDADE DE ENGENHARIA DA UNIVERSIDADE DO PORTO

NeuroFusion: Multimodal neuroimage fusion in pre-neurosurgical evaluation

Nádia Moreira da Silva

Integrated Master in Bioengineering - Biomedical Engineering

Supervisor: Prof. João Paulo Silva Cunha

July 28, 2013

NeuroFusion: Multimodal neuroimage fusion in pre-neurosurgical evaluation

Nádia Moreira da Silva

Integrated Master in Bioengineering - Biomedical Engineering

July 28, 2013

Abstract

The success of neurosurgery strongly depends on the pre-neurosurgical evaluation phase, in which the delineation of the areas to be removed or to be stimulated must be precise.

In the case of Epilepsy, the interpretation of the iEEG data can be enhanced by an exact detection of the position of the electrodes on the cortex. Therefore, the epileptogenic foci and the eloquent areas can be more accurately delineated. For patients undergoing deep brain stimulation, the delineation of the target areas prior to surgery and after the implantation is fundamental, as well as the confirmation of the electrodes implanted in these exact areas. Improvements in the identification of target areas and in electrodes positioning leads to a successful surgery and consequently improve the patient's outcome and quality of life.

For this study a collaboration was established with Dr. Ricardo Rego from Hospital São João, for the Epilepsy cases, and with Dr. Verena Rozanski from Munich University Hospital, for the patients with Parkinson and Dystonia, undergoing deep brain stimulation.

A pipeline and an interface were developed to accurately detect the subdural and deep brain electrodes, respectively. The positions of the deep brain electrodes were compared with the ones given by Dr. Verena Rozanski and differences of less than a voxel dimension were observed. Thus, the interface developed can be widely used to produce automatically the electrodes masks. The subdural electrodes were also accurately segmented without residues of skull, artefacts or even beam hardening. In order to enhance the visualization of the strips and grids over the cortex, cerebellum was removed.

Our tool was used in 3 iEEG epileptic patients and in the last one our results were part of the surgery decision procedure. A 3D model of MRI dataset, without cerebellum, overlaid with the subdural electrodes mask was created using MRIcron. The 3D model was used by HSJ for the pre-neurosurgical evaluation. The patient in which this approach was presurgically applied has being seizure-free since surgery, performed one month ago. More requests has been made by HSJ for future patients.

For the segmentation of the target areas for deep brain stimulation and others in the deep brain area, a recent automatic method available in FSL was used. The execution time of the automatic segmentation process, for each structure, was less than two minutes. The resulting structures masks were very congruent in shape and position with the corresponding area in the MRI dataset from the patient. Furthermore, the results obtained allows us to evaluate the performance and improve our knowledge of this recent method and therefore estimate their potential in future applications.

Resumo

O sucesso das neurocirurgias depende essencialmente da fase de avaliação pre-cirúrgica, onde a delineação das áreas a remover ou a estimular deve ser precisa. No caso da Epilepsia, a interpretação dos dados fornecidos pelo iEEG pode ser melhorada pela detecção exata dos elétrodos subdurais. Desta forma, o foco epilético e as área eloquentes podem ser delineadas com um maior rigor. Para os pacientes submetidos a estimulação cerebral profunda, a delineação das áreas alvo antes da cirurgia e após a implantação é fundamental, assim como a confirmação da colocação dos elétrodos nesses alvos. Por se melhorar a identificação das áreas alvo e a posição dos elétrodos é mais provável que a neurocirurgia seja bem sucedida, conduzindo a melhores resultados para o paciente e a um aumento da sua qualidade de vida.

Para este estudo, estabeleceu-se algumas colaborações clinicas, nomeadamente com o Dr. Ricardo Rego do Hospital de São João, para doentes de Epilepsia, e com a Dr. Verena Rozanski do Hospital Universitário de Munique, para o estudo de pacientes com Parkinson e Distonia, submetidos a estimulação profunda cerebral.

Desenvolveu-se um pipeline e uma interface para detectar com maior exatidão os elétrodos subdurais e profundos, respectivamente. As posições dos elétrodos profundos foram comparadas com as fornecidas pela Dr. Verena Rozanski, sendo que as diferenças encontradas foram menores que a dimensão um voxel. Logo conclui-se que esta interface pode ser amplamente usada para gerar automaticamente máscaras com as posições dos elétrodos. Os elétrodos subdurais foram também segmentados com bastante exatidão sem que se observasse a presença de resíduos de crânio, artefatos e beam hardening. Além disso, para melhorar a visualização destes sobre o cortex procedeu-se à remoção do cerebelo.

Seguidamente, as imagens de MRI sem a presença do cerebelo foram sobrepostas com as máscaras dos elétrodos numa visualização 3D, usando o MRIcron. Este método foi aplicado nos três pacientes de Epilepsia e no último os resultados obtidos fizeram parte do procedimento de delineação pre-cirúrgica. O paciente no qual o nosso método foi usado, demonstrou resultados pós-cirúrgicos positivos, não demostrando quaisquer crises desde a cirurgia. Dado estes resultados, mais pedidos foram feitos pelo Hospital para futuros pacientes.

Para a segmentação das áreas alvo da estimulação cerebral profunda e outras na sua vizinhança foi aplicado um método recente e automático disponível na plataforma FSL. Para cada estrutura o tempo de segmentação foi menor que dois minutos. As máscaras resultantes permitem-nos avaliar a performance e melhorar o nosso conhecimento deste novo método de segmentação e consequentemente estimar o seu potencial para futuras aplicações.

Acknowledgements

I would like to express my deepest gratitude to my supervisor for the opportunity to work in a neuroscience research, a theme that I really like. I thank him also for all his guidance and encouragement throughout this semester.

A special thanks I give to Dr. Ricardo Rego and Dr. Verena Rozanski for all the indispensable material for this work and the availability to discuss the results.

Furthermore, I would also like to thank to Eng. Sergio Tafula for all the technical support, even when he was on vacation, so that I could have access to the clinical data.

Finally, I would like to express my gratitude to my mother and colleagues for their endless support.

Nádia Moreira da Silva

"Lulled in the countless chambers of the brain, our thoughts are linked by many a hidden chain;
awake but one, and in, what myriads rise"

Alexander Pope

Contents

List of Figures

LIST OF FIGURES

List of Tables

LIST OF TABLES

Abbreviations

AAM	Active Appearance model
AC	Anterior Comissure
ANIMAL	Automatic Nonlinear Image Matching and Anatomical Labelling
ASM	Active Shape model
BG	Basal Ganglia
BET	Brain Extraction Tool
BT	Bottom Tip
CSF	Cerebrospinal Fluid
CT	Computed Tomography
DoF	Degrees of Freedom
DBS	Deep Brain Stimulation
DBs	Deep Brain structures
DTI	Diffusion Tensor Imaging
EEG	Electroencephalography
FLIRT	FMRIB's Linear Image Registration Tool
FNIRT	FMRIB's Nonlinear Image Registration Tool
FIRST	FMRIB's Integrated Registration and Segmentation Tool
FAST	FMRIB's Automated Segmentation Tool
FSL	FMRIB Software Library
fMRI	Functional Magnetic Resonance Imaging
GP	Globus Pallidus
GPi	Globus Pallidus internus
HSJ	Hospital São João
IPG	Implantable pulse generator
iEEG	intra electroencephalography
L-dopa	Levodopa
MRI	Magnetic Resonance Imaging
MNI	Montreal Neurological Institute
NMI	Normalized Mutual Information
PD	Parkinson's Disease
PC	Posterior Comissure
PET	Positron Emission Tomography
ROIs	Regions of interest
STN	Subthalamic nucleus
SPM	Statistical Parametric Mapping
SPECT	Single-photon Emission Computed Tomography
Syn	Symmetric Image normalization
UT	Upper Tip
WHO	World Health Organization

Chapter 1

Introduction

1.1 Context

Multimodal data fusion is the combination of different imaging modalities to provide a more useful and accurate information for clinical decision support.

This project is integrated in the Brain imaging network (www.brainimaging.pt) to easily access databases and toolboxes. An interdisciplinary collaboration of researchers working on this subject has been established for the achievement of this investigation. The main clinical collaborators are Dr. Ricardo Rego from Hospital São João (HSJ) and Dr. Verena Rozanski from Klinikum Großhadern of the Ludwig Maximilians University of Munich.

This investigation will be supporting HSJ and Klinikum Großhadern in pre-neurosurgical evaluation for Epilepsy and Parkinson or Dystonia patients, respectively.

1.2 Background

Movement disorders usually lead to a loss of independence for the patients and costs for the health system [9]. Parkinson's disease (PD) is one of the most common diagnosed movement disorders, with symptoms such as essential tremor, rigidity and akinesia. Less frequently diagnosed is Dystonia, which is characterized by a sustained muscle contractions producing writhing movements and abnormal postures.[6]

When pharmaceutical treatments lose effectiveness, normally in Parkinson and dystonic patients with longstanding administration of drugs, a neurosurgery is required. In this surgery, deep brain electrodes are implanted in substructures of basal ganglia (BG) such as the subthalamic nucleus (STN), globus pallidus internus (GPi) and caudal part of the thalamic ventral lateral nucleus. The stimulation carried by the electrodes allows the inhibition of the activity of these target structures. After the surgery, the motor and neuropsychological outcomes will depend on the precise location and trajectory of the electrodes.[6, 10]

Epilepsy is characterized by an abnormal mental status, uncontrolled movements, seizures and other psychic phenomena. As in PD, epileptic patients may show drugs resistance and neurosurgery is required. In an initial phase, a clinical electroencephalography (EEG) recording with scalp electrodes is performed to detect the epileptic focus. However, when no epileptic focus is identified, intracranial electrodes are implanted for a intra electroencephalography recording (iEEG).[10, 11, 12]

Following the implantation, the electric activity is correlated with neuroimaging data for pre-neurosurgical evaluation, and resection boundaries around epileptogenic zones are planned to remove the epileptic lesion, and consequently stop the seizures. In this procedure, the success of the patient's outcome depends on the exact delineation of the epileptic focus and the surrounding cortical areas.[13]

1.3 Motivation and objectives

In accordance with World Health Organization (WHO), neurological disorders have become a significant and growing issue, affecting, in 2010, more than 450 million persons worldwide.[14] PD and Epilepsy are the most common neurological diseases. Epilepsy reaches 1 in 140 persons worldwide, which suggests that around 75,000 people in Portugal have this condition and 30% had refractory epilepsy, requiring at the moment a resection neurosurgery [15]. For Parkinson, the worldwide epidemiological numbers are less disturbing, since 1 in 1000 individuals suffer from this disease and, in Portugal around 10,500 persons have this disorder. However, the WHO lists the neurological degenerative disorders, such as Parkinson, among the most costly group of disorders since financial costs mostly in terms of drugs and care are extremely high.[16, 14, 17]

Regarding Dystonia, recent epidemiologic studies are not available since this disease is usually associated with other diseases such as Parkinson, Huntington's and Wilson's disease. The established treatment for refractory dystonia is invasive methods such as pallidotomy and thalamotomies, in which globus pallidus and thalamus are destroyed. Although dystonic patients have shown improvements with ablative methods, it has been found after years of the procedure a disease progression and a decline of the movement functions [18]. GPi deep brain stimulation (DBS) may be an alternative procedure in comparison with the common invasive approach, considering that basal ganglia structures are stimulated rather than destroyed. In addition, this procedure has been shown to be safe with minimal adverse effects. [19]

Therefore, it is implied that more attention and efforts must be performed to enhance the actual clinical procedures and consequently improve the patients' quality of life, as well as reducing the costs associated with drugs and care.

In focal Epilepsy surgeries, patients' recovery depends highly on the exact position of subdural electrodes for the interpretation of iEEG data, which will lead to a higher accurate identification of the epileptic lesions as well as the surrounding cortical areas. At the moment, promising advances in structural and functional multimodal imaging allow neurosurgeons to maximize the resection of the epileptogenic area and preserve the eloquent cortex. These advances lead to a reduction

in surgery complications, a better outcome and the possibility to localize previously undisclosed cortical abnormalities, for instance subtle focal cortical dysplasia.[13, 25]

As referred in section 1.2, DBS patients' outcome depends on the accuracy of nucleus targeting by the implanted electrodes during surgery. Thus, brain atlases and atlas-based segmentation have been developed to easily target the deep brain structures (DBs) and the exact anatomic location of the electrodes.[20, 21, 22] Several authors have described an improvement in the target accuracy by using multimodal techniques with the fusion of anatomical and functional information. Such studies integrate in a common space segmented substructures of BG and the coordinates of the electrodes, using spatial normalization techniques. Although, few studies have correlated the patients' outcome with the anatomic position of the electrodes.[22, 23, 24]

Thereby, two major scenarios were identified to assist in pre-neurosurgical evaluation, that constitutes this thesis.

Can we develop intra-craned electrode accurate positioning method and easily target deep brain structures based on multimodal brain imaging fusion that can be applied in Epilepsy and DBS pre-neurosurgical evaluation?

For the Epilepsy scenario, a 3D model of the subdural electrodes will be defined on the cortex, in order to assist the visualization of the electrodes in relation to brain landmarks and therefore support the delineation of resection borders for the surgery. The removal of cerebellum from the structural images can improve the 3D visualization of some subdural electrodes positioned near this structure. Thereby, the segmentation of cerebellum to be removed from the structural datasets is other goal proposed for the Epilepsy study.

From the DBS point of view, the aim of this work is to fusion the data of several techniques to integrate in a common space the exact position of the DBS electrodes and substructures of BG. In addition, the distance of each DBS electrode to each structure under study will be determined and consequently related with patients' outcomes, since few studies have made this correlation.

1.4 Contributions

Considering the objectives proposed a tool will be used to segment DBs for the two scenarios presented here, using standard parameters validated in previous works.

For the segmentation of the subdural electrodes, several tools will be used by adjusting some parameters. In case of DBS electrodes segmentation, an algorithm will be designed to estimate the position of each electrode from the DBS lead. The estimation of DBS electrodes will be achievable either using a automatic or semiautomatic approach.

1.5 Dissertation Structure

In addition to the introduction, this dissertation contains 5 more chapters.

The chapter 2, provides a background to understand the principles and procedures used in this thesis, and present previous works of interest.

Chapter 3 presents the method applied for DBs segmentation either for Epilepsy scenario or for DBS scenario.

In chapters 4 and 5, the methods adopted to meet the goals proposed for Epilepsy and DBS cases are described, respectively, as well as the discussion of the results.

The conclusions of this investigation and future work are presented in the final chapter, 6.

Chapter 2

State of art

This chapter provides a background on concepts and procedures required for the understanding of the work presented in this thesis. In addition, some of previous works in the field of pre-neurosurgical evaluation are presented, as well as a detailed proposal of the several steps required for this work.

2.1 Epilepsy

2.1.1 Pathophysiology

Epilepsy is defined as an uncontrolled brain activity, when basal electrical activity rises above a critical thresholding. This disturbance may occur in one part or in the entire central nervous system, ceasing spontaneously but with a tendency to recur. Most often this disorder is accompanied by seizures, which may be focal or generalized.

In focal epileptic seizures, the discharge occurs in only one part of the brain and propagates to other areas of the brain cortex. In opposition, generalized seizures are characterized by an abnormal activity involving, from the beginning, large areas of the brain.

Since focal epilepsy is a consequence of a localized lesion or a functional abnormality, such residual scar tissue, tumors and local disturbed circuits, the resection surgery is usually recommended for these cases.[1]

2.1.2 Clinical Procedure

In order to isolate the epileptic focus in focal epilepsy, either a scalp EEG or a long-term video-EEG monitoring are performed and correlated with magnetic resonance imaging (MRI) information. The epileptic focus includes the exact location of seizure onset, but may even include tissue recruited for seizure generation (epileptic zone).[26] Usually the resection of this area is sufficient to prevent the seizures. However when the epileptic zone cannot be determined, or the data from

EEG is not in agreement with MRI, invasive recordings such iEEG are recommended.[10, 12, 11] This invasive procedure is also recommended in the situations at which the epileptic zone is adjacent to eloquent cortex.

In the surgery the electrodes which can be arranged in grids and strips are stereotactically implanted and electrically stimulated. The electric stimulation is crucial to locate and lateralize the eloquent cortex, which includes motor, somatosensory, language and memory functions. For the eloquent cortex identification and its lateralization, Wada test and the identification of Broca and Wernicke areas are usually used. Broca area is associated to the speech production and Wernicke to the understanding of written and spoken language. This is a decisive requirement to plan the resection surgery.[27]

Noninvasive tests such CT or 1.5T MRI are taken after surgery to confirm the placement of the grid or the position of the strip using anatomical landmarks. The accurate positioning of iEEG electrodes and inspection of the electric activity in the cortex is a means to detect lesions and correlate it with the eloquent cortex in the vicinity.[28] As a result, eloquent functions/areas are mapped and resection boundaries around epileptogenic zones are planned.[11, 29]

2.2 Parkinson

2.2.1 Pathophysiology

Parkinson pathophysiology is characterized by a generalized degeneration of dopamine cells of the substantia nigra; each is responsible to send dopaminergic nerve fibers to putamen and the caudate nucleus, two structures belonging to the BG. Dopamine acts as an inhibitory neurotransmitter of excitatory signals to the corticospinal motor control system. Thus, in the absence of dopamine the muscles are excited leading to akinesia and a state of rigidity characteristic of Parkinson.

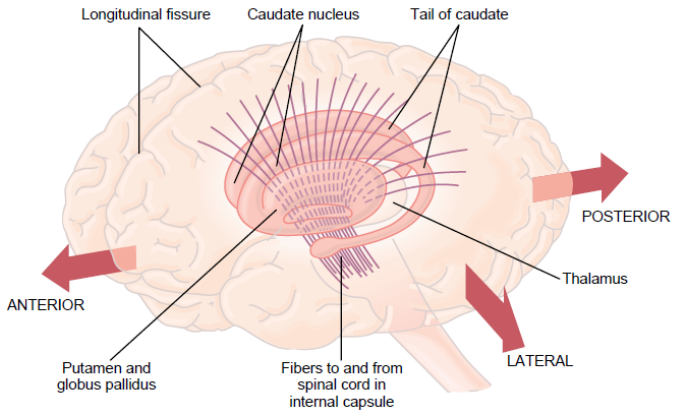

Figure 2.1: Anatomical relation of BG, cerebral cortex and thalamus [1].

The BG are a motor accessory system that works along with the cerebral cortex and the corticospinal motor system. Anatomically is composed by GPi, substantia nigra, STN, caudate nucleus

and putamen. These structures have numerous interconnections with each other and with the motor cortex. As seen in figure 2.1, the association between BG and the corticospinal motor system is made by nervous fibers that connect the two structures. The area of nerve fibers is known as internal capsule of the brain.[10, 1]

2.2.2 Clinical Procedure

Most interventions aimed at controlling the symptoms of PD rely on the use of drugs. The common used drugs are levodopa (L-dopa) and dopamine agonists, but others may also be used since each person react to medication in different ways.[30]

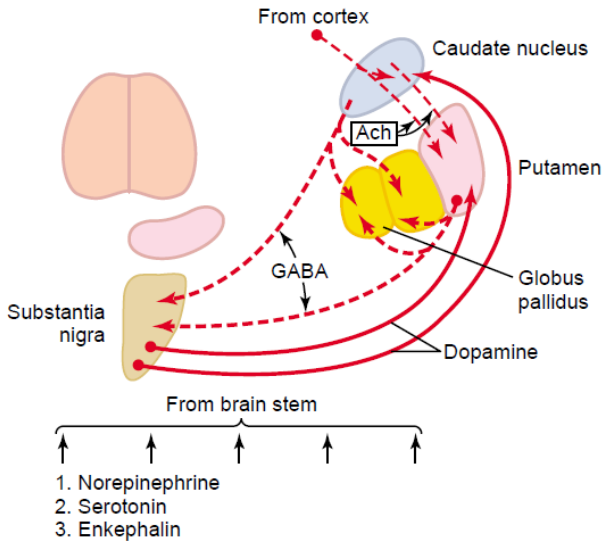

Figure 2.2: Neuronal networks of substantia nigra [1].

Recently, Parkinson patients who present motor fluctuations and dyskinesias, despite the maximal dose of drugs, may be indicated to DBS. Neurostimulation has similar effects to ablative surgery but does not cause irreversible lesions.

DBS promote functional inhibition as the dopamine, in the BG motor system. In STN stimulation, DBS leads to the substantial dose reduction or even withdrawal of L-dopa. In addition, GPi stimulation allows to increase the dosage of L-dopa with the alleviation of peak-dose dyskinesias. The stimulation in other substructures of BG can reduce some of the symptoms, however the most significant effects were seen with STN and GPi stimulation.[10]

The significant effects in these substructures can be explained by the neuronal networks in BG. (see annex, figure A.1) The substantia nigra is connected to several substructures of BG by neural networks, operating as an inhibitory stimulation motor. When this substructure is degenerated the following substructures in the neuronal network, remain in a state of excitation. As described in 2.2, the substantia nigra has dopamine networks to GPi and putamen. The putamen is responsible for inhibiting the STN and GPi, which control the stimulation in the thalamus. (see annex, figure

A.2) Since thalamus is directed connected to corticospinal motor control, their stimulation by STN or GPi is fundamental to control the symptoms of PD. However the knowledge of these networks in the basal ganglia is not yet fully understood which may explain the different outcomes and advantages obtained by STN and GPi.[1]

Figure 2.3: DBS Lead Model 3389 with 4 electrodes at the tip [2].

The common procedure for DBS neurosurgery starts with the definition of the STN area, prior surgery, using a MRI image as well as standard coordinates in relation to the anterior commissure (AC) and posterior commissure (PC). [31]

Then the patient enters in the operating room to define with higher precision the STN target previous deduced. To this purpose, microrecordings and microstimulation are performed. Microrecordings and microstimulation allows the identification of specific structures based on the patterns of neuronal activity when the patient is doing specific tasks movements. [31]

Once the final target is identified, DBS lead is implanted and the electrodes position on the STN are confirmed by a CT scan. The figure 2.3 shows an example of a DBS lead with four electrodes at the tip. Each electrode is connected to a contact in the upper tip of the lead, which is attached to the implantable pulse generator (IPG). Each electrode is tested for clinical efficacy and side effects, and only the one with best efficacy and largest therapeutic width is chosen to be stimulated by IPG. Electrodes closed to structures, such pyramidal tract, the corticobulbar tract and optic tract among others, promote acute side effects such as evoking excitation rather than inhibition.[10, 32] Therefore, accurate localization of electrodes after the surgery is crucial to confirm that they are not near the above described structure and to choose the one which is stimulating the target area.

Atlas such as the Schaltenbrand-Wahren, figure 2.4, are used by neurosurgeons to define the electrodes anatomic position and define the target area to stimulate.[33, 34, 4]

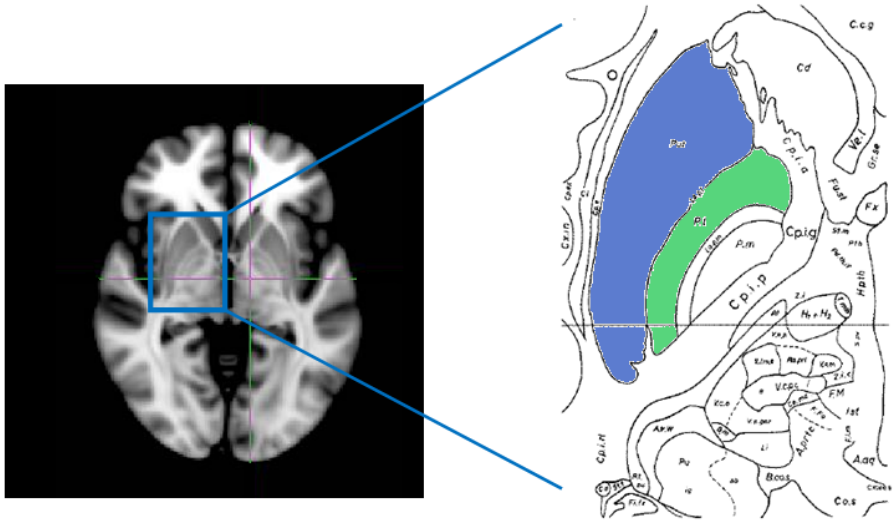

Figure 2.4: Axial view from the Schaltenbrand-Wahren atlas provided by Dr. Verena Rozanski zoomed in relation to a axial MRI image from the montreal neurological institute (MNI) space. The figure shows some structures of BG in particular putamen (blue) and GPi (green).

2.3 Dystonia

2.3.1 Pathophysiology

Dystonia is defined as a neurological movement disorder, which main pathophysiological feature is co-contraction (when opposing muscles are contracted simultaneously), leading to twisting and repetitive movements or abnormal postures. During voluntary movements, the symptoms may become more apparent.

This condition may be due to a derangement of the spinal cord or cortical mechanism. Although, these derangements are not fully understood, studies suggest that, at the cord level, abnormalities of the normal coordinate inhibition between agonist and antagonist are the leading cause. A reduced presynaptic inhibition of the afferent muscle to the inhibitory interneuron was identified, possibly due to a abnormal descending control or an alteration in the tonic afferent input to the interneuron from cutaneous and muscle afferents [35].

On the other hand, the abnormal descending control on the presynaptic inhibition is being related with an irregular neurochemical transmission in the BG, brainstem, or both. The irregular transmissions were observed mainly in putamen, globus pallidus (GP), thalamus, motor cortex and somatosensory cortex. [3]

2.3.2 Clinical Procedure

The main treatment for Dystonia is the intramuscular injection of botulinum toxin to denervate the affected muscles and increase the presynaptic inhibition [35]. According with literature, the toxin changes the tonic sensory inflow from the injected muscles, improving the derangements seen at the spinal cord motor system. However, this approach is quite limited when several muscles are

involved, the movement pattern is complex or in the presence of neutralizing antibodies [36, 35]. Surgical approach such as DBS is an alternative to these cases.

Studies have found a correlation between Dystonia and an activity reduction in the cortical inhibitory circuits of BG, the red lines found in the figure 2.5. The activity reduction of inhibitory circuits is being related to an overactivity or hyperfunction of lentiform nucleus (putamen and GP) [35]. In addition, GPi stimulation was found to be effective for dyskinesias in PD, one of the symptoms similar to Dystonia.

Therefore, GPi stimulation is currently used for dystonic patients, since a good outcomes with GPi as target was verified and this stimulation may control the hyperfunction identified due to the disruption of BG inhibitory control [36, 37].

Most interestingly, there is a difference between ventral and dorsal GPi and the direct and the indirect motor systems, (figure 2.5), which may explain the co-contraction symptom [38].

The putamen affects differently the motor output, depending on the activated motor systems. In the direct pathway or system, when the putamen is stimulated, inhibits the GPi and this latter will disinhibit the thalamus. Then cortex is excited by the disinhibited thalamus. In opposition, in the indirect pathway, putamen stimulation inhibits the globus pallidus externus which in turn will disinhibit the STN. When being disinhibited, STN excites the GPi which will inhibit the thalamus, and consequently reduce the cortical excitation.[3]

When a disruption of BG inhibitory circuits of the two pathways is created, an imbalance is induced between the direct and indirect motor systems, and therefore the excitation or inhibition of the cortex may cause the co-contraction, indicative of Dystonia syndrome. In the literature, different symptoms of dystonia has been connected with either overactivity in the direct pathway or in the indirect pathway, suggesting once again that this disease is caused by abnormal BG circuits which create an imbalance between the direct and indirect pathways.[35, 3]

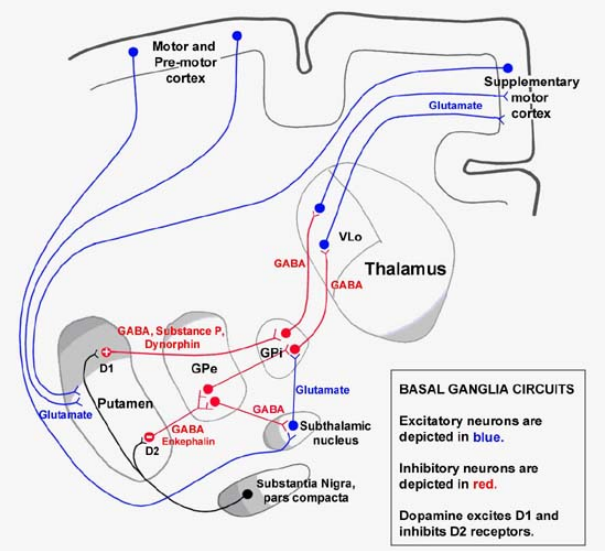

Figure 2.5: BG interconnections, describing the direct and indirect pathway between putamen and cortex.[3]

The DBS clinical procedure for dystonic patients is the same as Parkinson's, with GPi as the target structure.

2.4 Spatial Normalization

2.4.1 Co-registration

Co-registration is defined as a method for realigning images either for motion correction or for overlaying images from different modalities, as can be depicted in figure 2.6. It is a useful approach to visualize implanted electrodes on a structural image or detect lesions that were unable to be differentiated from adjacent normal brain.

Brain warping or registration is the technique used for realigning images, in which brain landmarks are mapped by applying geometric transformations to corresponding points on different images. Some geometric transformations include global scaling, affine transformation, linear, nonlinear and local deformations. Each one redefines the spatial relationship between points on the brain images by establish a set of transformation parameters. These parameters contain information of region similarity and difference between the data, which may allow the analysis of anatomic regional deformations and consequently brain alterations.

A wide variety of 3D image warping approaches have been designed to handle neuroanatomic data, such intensity-driven and model-driven approach.[39] Intensity-driven method is based in the measurement of an intensity similarity between the data, which is then maximized. This measurement may include cross-correlation, squared differences in pixel intensities among others. In contrast, model-driven approach use anatomical landmarks between the data to be matched. Some of these landmarks may be sulcral-ventricular curve, gyral crests or functionally surfaces.

In both strategies, the elements of the original image can dilate, twist or rotate to match to the reference data, although these transformations are limited by the method used. In rigid body transformations, such affine transformation, only linear transformations are allowed. As opposed, nonlinear transformations considered that the original image is embedded in a 3D elastic medium, obeying to the laws of continuum mechanics, such Navier-Stokes equilibrium equation for linear elasticity. A nonlinear transformation guarantees the topological integrity of the original image.[39]

Partial volume effect, a consequence of anisotropic voxels, may be a drawback of co-registration, since the fused image resulted by the co-registration may appear flattened or elongated on certain views. As a result, the image may be blurred, even when anisotropic voxels are geometrically transformed in relation to an isotropic voxel. In order to obtain isotropic voxels and overcome this issue, the time required for image acquision may need to be increased. However, in such cases, the patient is motionless for a long time and the risk of motion artifacts increases.[40, 41, 42]

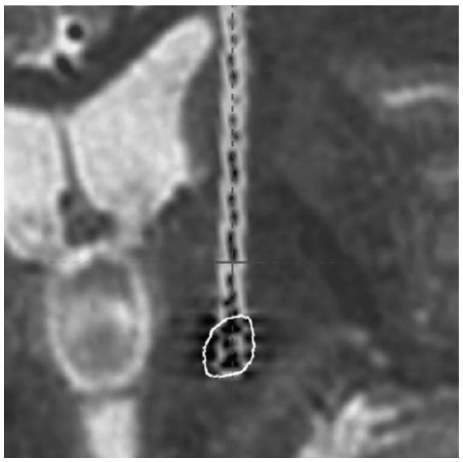

Figure 2.6: An example of computed tomography (CT) and MRI co-registration, showing DBS lead in the structural image [4].

2.4.2 Warping to a template

Brain warping can also be applied to realign images of individual segmented brains in relation to a standard template or coordinate system.

To construct a brain template, co-registration algorithms are used to align brain MRI images in relation to a reference brain image. The common templates apply linear followed by a non-linear registration to overcome the inter-subject anatomical differences in shape, size, and relative orientation. Therefore, anatomical variability is reduced and is feasible to achieve better functional correspondence of homologous brain regions across patients.[43] There are essentially two types of atlas: deformable and probabilistic atlases. Deformable atlases are based on the anatomy of brain structures. The anatomic volumes of the individual data are elastically deformed, in accordance with Navier-Stokes equation, to adapt to the shape of the atlas. This approach can be helpful to detect pathologies in epilepsy and the detection of substructures in BG, since atlas deformations contain pre-segmented anatomic models.[44] These models can be applied in the individual new data, automatically labeling their anatomy. Probabilistic atlases are adequate in the representation of specific subpopulations, since it contains information of structural and functional variation on different populations. These atlases are being used in diagnostic for the detection of structural brain anomalies. [39]

Therefore, warping individual brain data into a common stereotactic space can be useful in pre-neurosurgical evaluation and in the detection of anomalies.

2.4.3 Brain atlases

In the last decades, several brain atlases was been developed providing data of normal and pathological brains. The most well known atlas are Talairach & Tournoiix and MNI, which differ in features such the number of the subjects, registration procedure, spatial transformation among others.[43, 44]

Nevertheless, only the MNI-152 atlas will be focused in this section since is the one that will be effectively used for this work.

MNI-152 template was obtained from 3D brain MRI images of 152 normal subjects. For the registration procedure a linear 9-parameter affine transformation was applied to a target image followed by a non-linear registration, to avoid the inter-subject anatomical differences. This template was the advantage of providing a full head coverage.[43]

A review of structural brain atlases can be found at [43].

2.5 Brain Imaging Software Tool

Several applications of data processing and visualization were studied as tools for the proposed goals. Some of these applications are listed below:

- 3D Slicer;
- BrainVoyager;
- Osirix;
- MRIcro;
- MRIcron;
- FMRIB Software Library (FSL);
- Statistical Parametric Mapping (SPM).

3D Slicer

3D Slicer is an application of visualization, segmentation, co-registration and quantification in medical data, such as measure distances, angles, surface areas and volumes in different modalities. Furthermore, allows the user to extract surfaces and create 3D models. This software supports a few formats such as DICOM, NIfTi and Analyze.[45, 46]

BrainVoyager

BrainVoyager is a software package for the analysis and visualization of functional and structural MRI data. Methods for automatic brain segmentation, surface reconstruction and cortex-based inter-subject alignment are accessible to the user. The software integrates tools for volume and surface rendering as well.[47]

Osirix

OsiriX is essencially a DICOM images viewer. It integrates several visualization 3D tools for medical images such 3D surface or volume rendering. For processing, ROIs and co-registration tools can be applied both in 2D and in 3D view.[48]

MRIcro

MRIcro is a tool for image visualization, in which the user has the possibility to generate 3D volumes and select regions of interest (ROIs). In addition, overlays of different modalities

are normally used to confirm the co-registration of two images. This software can also convert DICOM to Analyse format.[49]

MRIcron

MRIcron is basically the MRIcro but with additional features. This application only supports the NIfTI format as opposed to MRIcro and allows the conversion of DICOM files to NIfTI.[49]

FSL

This software has several tools for brain imaging analysis, visualization and processing. Tools such as Brain Extraction Tool (BET), FMRIB's Linear Image Registration Tool (FLIRT), FMRIB's Nonlinear Image Registration Tool (FNIRT), FMRIB's Integrated Registration and Segmentation Tool (FIRST), FMRIB's Automated Segmentation Tool (FAST), fslroi, fslstats and others allow the user to generate 3D regions of interest, to extract the brain, to segment subcortical brain structures, to apply co-registration in different image modalities and warping the images in distinct templates. NIfTI format are the common format used as input and output.[50]

SPM

SPM software is a set of MATLAB functions which allow, for instance, the realignment, spatial normalization to a standard space and smoothing of a sequence of images of different modalities such functional MRI (fMRI), positron emission tomography (PET), single-photon emission CT (SPECT), EEG and magnetoencephalography. In addition, it uses the NIfTI file format, a format incompatible with standard MATLAB software and commonly used to store medical image data.[51, 46]

A more detailed information for these tools and others not mentioned here can be found at [46].

2.6 Neuroimaging Techniques

In the pre-neurosurgical evaluation, several modalities are used by physicians in the area of neuroscience. The non-invasive techniques are listed below:

- EEG;
- MRI;
- CT;
- PET;
- SPECT;
- Video-EEG monitoring;
- Diffusion tensor imaging (DTI);
- Neuropsychological tests.

In this section will only focus on the techniques that are effectively used for this work.

MRI is the modality most frequently used in neuroanatomical studies since the resulted images allow a better understanding of the brain organization and structure, useful for the detection of pathologies.

In MRI images, each point depends on the magnetic properties of the tissue in that position. Since different tissues have different local magnetic properties, images acquired with MRI have higher sensitivity to anatomic variations and consequently higher contrast than conventional radiology and CT.[52] Given these characteristics it is usually used as anatomical reference for co-registration with others modalities.[46] Despite these advantages, 3T MRI exhibit artifacts when in presence of metal, as the electrodes used in epilepsy, Parkinson and Dystonia surgery, hindering their detection.

There are two main MRI contrasts scans, T1-weighted and T2-weighted MRI, which will be the ones used in this work (figure 2.7). Fluids such cerebrospinal fluid (CSF) in T2 images appear brighter, as opposed to the T1-images. These differences in the CSF but also in others tissues, allows for instance to improve the contrast in the borders on different deep brain structures.

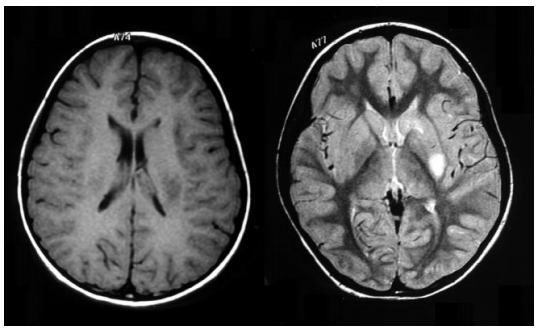

Figure 2.7: Example of a T2-MRI scan (right) and T1-MRI scan (left).

In **CT** several projections are acquired around the area of interest and processed by the computer, after the patient is exposed to X-rays. Compared with conventional radiography, CT has worse spatial resolution but better contrast resolution, which makes this technique more suited to perform spatial characterization of bone tissue or other dense materials such as electrodes.[53, 46]

Therefore, only a CT or 1.5T MRI are recommended for the detection of electrodes.

A review of these modalities can be found in the [53].

2.7 3D visualization

To reconstruct a 3D human brain model, either surface or volume rendering are suitable approaches.

Surface rendering do not retain information deep to the surface, providing a data suitable only for morphometric measurement. This approach, uses geometric primitives such as polygon meshes prior to the viewing and shading stages. The surface is represented as a set of discrete nodes which are connected to one another to form the mesh that will be deformed to the desired shape of the

brain. Three strategies have been used to generate surface models, which differ in initial surface model delineation, volume segmentation, contour delineation and surface deformation.[39]

The choice of the layer for surface representation depends on the strategy selected. The most common layers are the pial surface and gray-white boundary, (the external and internal surfaces of the cortical gray matter). Although none of them provides an optimal representation of the cortex surface. Using gray-white boundary, surface reconstruction underemphasizes gyral regions and overemphasizes sulcal regions near their fundi. In contrast, the opposite occurs using a pial surface reconstruction. As described in literature, using the midway between the gray-white border and pia as a layer is advantageous because it ensures that each surface unit has the same volume of cortex. However, this layer may be difficult to delineate, especially in structural MRI images.[39]

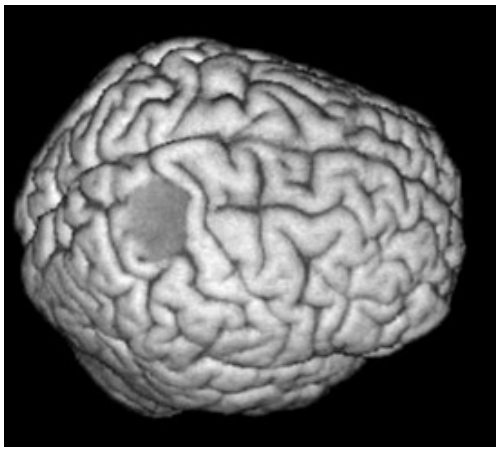

Figure 2.8: Surface Rendering example: showing a brain tumor in the right parietal lobe [5].

Usually, **Volume rendering** projects volume primitives such as spheres and boxes directly for shading and viewing.[39] There are three main approaches to do volume rendering: segmentation, classification and direct visualization. In segmentation, the image volume is divided in different homogeneous regions based on criteria, which can be binary or fuzzy. Binary methods are disadvantageous, since they assume that each voxel belongs to an exact region, not taking into account the cases in which an object takes up only a fraction of a voxel. As opposed, in fuzzy segmentation a set of region probabilities are assigned to every voxel.

Classification methods can also be applied to segment the data into components for inclusion or exclusion in a given view and identified or labeled the regions.

Direct volume visualization, creates the images directly from the volume data, allowing a combined display of different aspects such as opaque and semitransparent surfaces, cuts, and maximum intensity projections. For each voxel, a color and opacity is assigned. Opacity is the result of the product of an object-weighting function and a gradient-weighting function. The object-weighting function is often dependent on an intensity or a fuzzy segmentation algorithm. The gradient-weighting function is applied to enhance the surface smoothness. This procedure is useful since binary decisions are avoided and the resulting images are very smooth and show a lot of fine details. Furthermore, spatial perception is improved since the entire information of

the dataset is retained and used for the visualization. However, the approach depends highly of the parameters for the weighting functions, which, in automatic software's algorithms can be a drawback.[5]

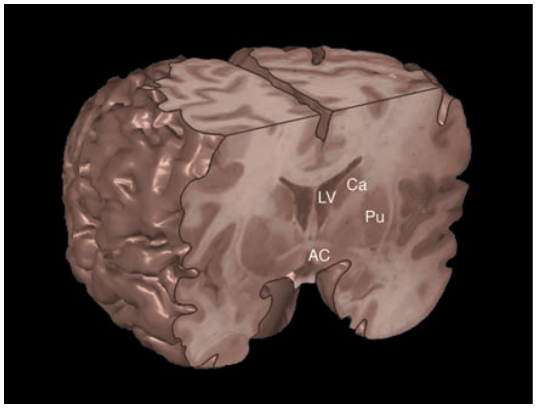

Figure 2.9: Volume Rendering: coronal view through the AC, exposing the caudate nucleus, putamen and lateral ventricles [5].

Examples of Surface and Volume rendering can be seen in figure 2.8 and 2.9, respectively. A review of this theme can be found in [5].

2.8 Multimodal data fusion

According to the literature, imaging techniques used alone have poor diagnostic accuracy in comparison with a multimodal approach. This approach, as referred in section 1.3, has been improving the pre-neurosurgical evaluation, either in Parkinson, Dystonia or Epilepsy, in the detection of brain substructures or pathologies, and in the localization of electrodes position.

The combination of CT with MRI, allows the physician to analyze anatomical structures with better resolution and with a more accurate position for the electrodes. Better symptom relief and low morbidity is seen in the patients whose electrodes were accurately detected.[29, 54] Furthermore, CT and MRI fusion images are described to allow optimized electrodes positioning and lead to a more easily and quicker reprogramming of stimulation parameters in DBS cases.[24, 55]

However, multimodality is not restricted to CT-MRI fusion. Although this study is focused in these techniques, multimodality has been widely applied in others techniques, especially in cases of Epilepsy. In some cases, even with CT-MRI fusion, the epileptic lesions are not identified, probably due to white matter abnormalities, which can't be detectable by MRI. DTI and techniques such 18F-fluorodeoxyglucose PET or 11C-flumazenil PET and ictal-interical subtraction SPECT have been showing positive results, even showing lesions that were not present in abnormal MRI.[29, 25]

Furthermore, EEG-fMRI fusion has been used as a tool to localize primary motor, somatosensory and language areas, thereby being useful to predict the effects of lobe resection on language and memory impairment. [29]

Regarding Parkinson, DTI-MRI fusion is described as a potential tool for detection of Parkinson in early stages. Based on the known neuromotor fibers and Schaltenbrand-Wahren atlas, some of BG substructures are being outlined, such thalamus, corpus callosum, putamen, substancia nigra, STN and GPi [56, 57, 58]. The relation of the proximity of fibers to the DBS electrodes and the substructures will be a remarkable step for neuroscience, to understand better the patients' outcome.

As suggest in 2.3, the pathophysiology in Dystonia is largely unclear. DTI-MRI fusion is being used to enhance the current knowledge of the motor circuits connecting the cortex, BG and cerebellum, and thereby improve patients' outcome in the future. [59, 38]

2.9 Proposal

After an analysis of the goals, referred in section 1.3, and the various requirements or considerations to meet them, discussed in this chapter, the various steps and tools to the achievement of this work were determined.

For the multimodal fusion of electrodes positioning with the DBs for Dystonia and Parkinson patients, several steps are required, including the choice of the template to define a common stereotactic space, segmentation of target structures on the template, accurate segmentation of the DBS lead and the corresponding electrodes, co-registration of the patient's multimodal image data and alignment of the patient's image data into the common space for comparison with electrodes position. The relation of the patient's outcome with the electrodes position will be based on the segmented masks of the electrodes and the structures estimated by the multimodal fusion method.

Since Parkinson and Dystonia research was being developed in FSL by Dr. Verena Rozanski, our clinical partner at the University of Munich, this toolbox was preferred. In addition, as compared with the other tools referred above, FSL is functionally more extensive regarding spatial normalization. SPM and MATLAB were also chosen owing to its built-in functions that allow for efficient development of algorithms and manipulation of images.

To develop the multimodal imaging pipeline for Epilepsy scenario, FSL were selected since, as cited above, has a tool to extract the brain which is essential for the visualization of the electrodes over the cortex in a 3D model and has more co-registration options. MRIcron was chosen since allows the user to generate 3D renderings and runs in Windows system, in contrast to others software mentioned above. Furthermore, MRIcron reads NIfTI files which is the output files format by FSL.

Chapter 3

Automatic segmentation method for deep brain structures

In this chapter some of the current automatic segmentation methods for deep brain structures will be discussed as well as a detailed description of the selected method used either to segment the cerebellum for the Epilepsy scenario or others deep brain structures for DBS scenario.

3.1 Automatic procedures

The most common methods of segmentation are based on the intensity information and its variation within a specific structure. However, for DBs the intensity segmentation methods fails due to the loss of contrast in this region [7].

Therefore, other methods were developed based in a prior knowledge of the shape and position of these structures. Non-linear and linear registration-based approaches are the major examples of these procedures.

In the non-linear registration method manual masks are delineated in a template by an expert, with prior knowledge of the intensity and shape of the specific structures, then the masks or labels are warped from the template to the individual MRI image using non-linear registration transformation. There are several non-linear algorithms to perform this spatial warping transformations such as Automatic Nonlinear image Matching and Anatomical Labelling (ANIMAL) and Symmetric Image Normalization (Syn).[6]

These procedures are widely used since the segmentation results for the subcortical structures are very accurate. However, the registration step can take hours.[6]

In contrary, despite linear registration methods do not lead to the accurate results as seen in the non-linear procedures, the registration step only lasts a few minutes.[6, 60] In linear registration procedure, manual masks are outlined in the individual space and linear registered to the template to be used as a labelling templates for each structure. When a new MRI image is added

the previous linear registration step is applied and the neighbourhood of each voxel of the MRI image is compared with similar neighbourhoods of the labelling templates. In the patch-based segmentation, a recent linear registration procedure with good performances, use the neighbourhood similarities across all the templates as an weight label function to segment each voxel and consequently the structures. [60]

FIRST, a tool already referred in section 2.5, is another example of an automatic segmentation method based on linear registration.

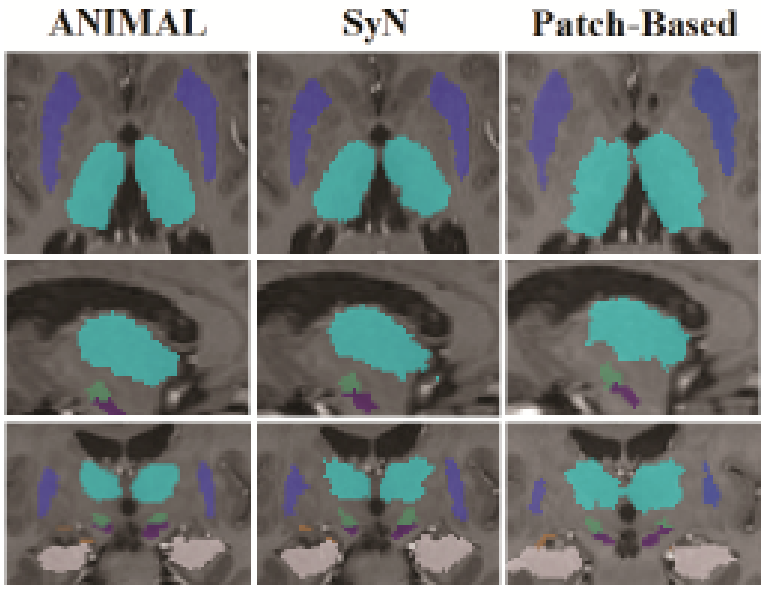

Figure 3.1: Examples of masks obtained by ANIMAL registration, SyN registration and patch-based method for deep brain structures [6].

3.2 FIRST

FIRST allows the segmentation of some BG structures such as caudate nucleus, putamen, pallidum, nucleus accubens and other DBs such thalamus, amygdala, hippocampus and cerebellum. The main steps of this algorithm will be discussed in this section.

Basically, this tool combines intensity and shape information of a training dataset to develop a 3D mean model of each structure which is then adjusted by an iterative process to the target structure of the subject. For the shape and appearance/intensity model development, the principles of the Active Shape (ASM) and Active Appearance models (AAM) are applied as well as a Bayesian framework, to obtain intra and inter-structure variability information. [61]

3.2.1 Training dataset

The model resulted by ASM and AAM was trained using 336 manually-labelled T1-MRI, which comprises data from normal and pathological brains (schizophrenia, Alzheimer's disease, attention

deficit disorder and prenatal cocaine exposure). Furthermore, MRI images belongs to children, adults and elderly subjects. [62]

The variability information for the Bayesian framework is inferred by the models of each structure of the 336 T1-MRI previously defined and manually segmented by the Center for Morphometric Analysis in Boston.

3.2.2 Registration

The training dataset was aligned to the MNI-152 space using a linear subcortical registration, to lead to a more accurate alignment of the subcortical structures. Therefore, two-stage affine registration to MNI-152 space at 1mm resolution was developed by the FIRST developers and applied in each T1-MRI from the training dataset. In the first stage, an affine registration of the T1-MRI to the non-linear MNI-152 template was performed using 12 degrees of freedom (DoF). For the second stage the T1-MRI dataset previously aligned with the MNI-152 template was linearly transformed with a subcortical mask defined in the MNI space as a reference. These subcortical masks were obtained from the average of 127 labels of the training dataset, after a standard affine registration (figure 3.2). [7] These second stage allows to exclude some voxels outside the subcortical masks and concentrate the registration only in the subcortical alignments.

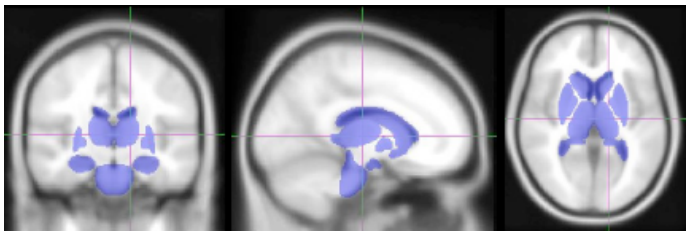

Figure 3.2: Subcortical mask (blue) used in the second step of the registration overlaid with the MNI-152 template [7].

For cerebellum segmentation the corresponding subcortical mask is not yet available, so a brain mask is normally used to exclude voxels outside of the brain and then the cerebellum.

After the training dataset was linearly registered to the MNI space, the intra and inter-structure variability information of shape and intensity across all the dataset was estimated for the 3D model development, as detailed in the next section.

3.2.3 Segmentation

As in ASM, FIRST models the surface of each structure by a set of connected vertices. The vertex location variation across all the training dataset allows to obtain a statistical distribution inter-vertex, i.e, holds information regarding how vertices vary across the dataset and with respect to each other for the same subject. This variation is represented as a multivariate Gaussian by two components, the mean shape and a covariance matrix or modes of variation. The maximum number of modes of variation available is 336 since the training set comprises 336 T1-MRI images. [7]

In addition, as in AAM, to develop a model the intensity distribution along the surface normals is represented by a mean value and a set of modes of variation as in ASM, after an intensity normalization step.

The intensity normalization was performed in two steps, a global scaling and an subtraction of the mode of the intensities within a specified structure. Although for same cases, the mode of intensities of neighbourhood structures are used to normalize a specific structure. Since caudate nucleus, hippocampus and amygdala are susceptible to atrophy in the pathological brains of the dataset, their intensity mode would vary with their shape/size. Considering that the intensity normalization is performed within the average models, a constrained shape, the use of mode intensities of others structures such thalamus is favourable. [7] The 3D average model is the average model from 127 subjects of the training dataset.

The combination of the mean shapes and modes of variations in a Bayesian framework allows to establish probabilistic relationships between shape and intensity variations among the structures and within each structure.[61, 62]

When a new image is used to be segmented by FIRST the 3D average model is adjusted within the variations found with AAM and ASM but limited by the probabilistic relationships between them.

The segmentation masks resulted by FIRST are labelled with a value for interior voxels and +100 value for boundary voxels. The classification of the boundary voxels in the volumetric structure is available in FIRST options. FAST, a FSL tool for tissue segmentation may be selected for boundary classification and, consequently, deduce a more accurate border to the structures, since they have borders with grey matter, white matter and CSF. Thereby, FAST classifies the boundary voxels of the mask on white matter, grey matter or CSF and depending of the result the voxels can be converted into interior voxels of the structure.

3.2.4 Implementation

FIRST performance was validated using a leave-one-out crossvalidation. Validation provides the necessary information to estimate the parameters that will lead to a better segmentation for each structure.

In the table 3.1 is presented the better parameters combination for each structure, estimated by FIRST developers in previous works. The number of modes of variation on the table were establish to achieve a good compromise between including enough variation, to capture the structural details, and avoiding too many modes, which can complicate the optimization stage and significantly increase the computational cost [62].

The implementation of FIRST for the Epilepsy and DBS scenarios will be carried using the default values and options presented in the table 3.1. The principles of the algorithm described in this chapter will be helpful to understand and discuss the results obtained using this recent tool.

Table 3.1: Number of modes of variation, boundary correction method and the structure to normalize the intensities. [7, 62]

Structures	Modes of Variation	Boundary Correction	Intensity Normalization
Amygdala	50	FAST	Thalamus
Caudate nucleus	30	FAST	Thalamus
Cerebellum	40	none	Putamen
Hippocampus	30	FAST	Thalamus
Nucleus Accubens	50	FAST	Self
Pallidum	40	none	Self
Putamen	40	none	Self
Thalamus	40	none	Self

Chapter 4

Epilepsy Scenario

For the Epilepsy it was intended to establish a 3D model with the subdural electrodes over the cortex, to assist the clinical group from HSJ in the delineation of the epileptic focus and eloquent areas. The procedure adopted to segment the electrodes and visualize them over the cortex, on a 3D view, is described below, as well as the discussion of the results.

4.1 Methods

Three patients with refractory Epilepsy undergoing surgical implantation of subdural electrodes for epileptic zone localization were selected by HSJ for this study. All the data provided was anonymized to preserve the patient's personal information. The diagnosis and treatment plan for each patient can be consulted in the section A.2, in the annex. For patient 1 and 2, a post-operative whole head T1-MRI images were acquired using a 1.5T MRI unit (SIEMENS, Magnetom Symphony Tim) with a voxel size of 0.875 x 0.875 x 0.88mm for patient 1 and 1.09 x 1.09 x 1.09mm for patient 2. The electrodes position were confirmed by a CT unit (SIEMENS, Somatom Emotion Duo) with a voxel size of 0.547 x 0.547 x 1mm. In the case of patient 3, two imaging studies were acquired, before and after the implantation. Structural pre-operative whole head T1-MRI images were gathered using a 3T MRI unit (SIEMENS, Magnetom Trio Tim) with a voxel size of 1.09 x 1.09 x 1.09mm. To confirm the electrodes position, a CT scan (PHILIPS, Brilliance 16) was acquired with a voxel size of 0.547 x 0.547 x 1mm.

In order to meet the proposed goals, a method was designed based on FSL and MRIcron for the pre-processing, processing and 3D visualization stages. The workflow adopted is summarized in the diagram 4.1. In the section A.3 of the annex the several steps of the workflow adopted can be consulted in more detail.

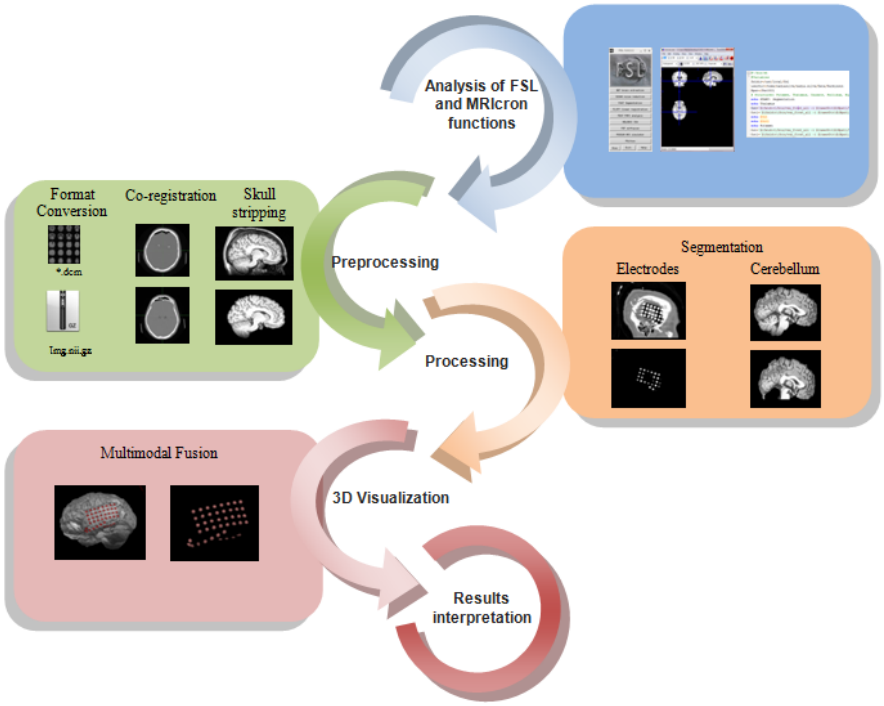

Figure 4.1: Workflow adopted for the Epilepsy cases, describing the several steps performed and inspired in [8].

4.1.1 Preprocessing

All the data provided were converted from Dicom to NIfTI format using MRIcron, since FSL does not support Dicom files.

As in the present study is intended to obtain a 3D cortical surface model, the automated skull-stripping tool BET was used in T1-MRI. BET uses a deformable model that fits to the brain's surface, using locally adaptive model forces. Furthermore, the extraction depends highly on the fractional intensity threshold, which controls the distinction of brain from non-brain and, consequently the centre-of-gravity of the head in which the model surface is initialized. During this process inner and outer skull surfaces, and outer scalp surface, in the case of a high quality T1, are also estimated. [63]

Different fractional intensity thresholds were tested to get highly accurate results. Lower

Table 4.1: Comparison between the default values and the ones applied in the Epilepsy pipeline for the preprocessing and processing stages, using BET and FLIRT tools.

	BET	FLIRT			
	Intensity Threshold	Geometric transform	Angular range	Cost function	Reslicing method
Default	0,5	Affine (12DoF)	-90 to 90	Correlation ratio	trilinear
Applied	0,3	Rigid body (6Dof)	-30 to 30	NMI	trilinear

thresholds were preferred in relation to the default value, as seen in the table 4.1, for the post-operative T1 scans, since they produce larger brain estimation and, consequently, preserve the visualization of the electrodes which were implanted over the cortex. By keeping the visualization of electrodes on the brain of the post-operative images, the physician can compare the electrodes' position with the ones given by the electrodes masks, estimated from CT data in the next section.

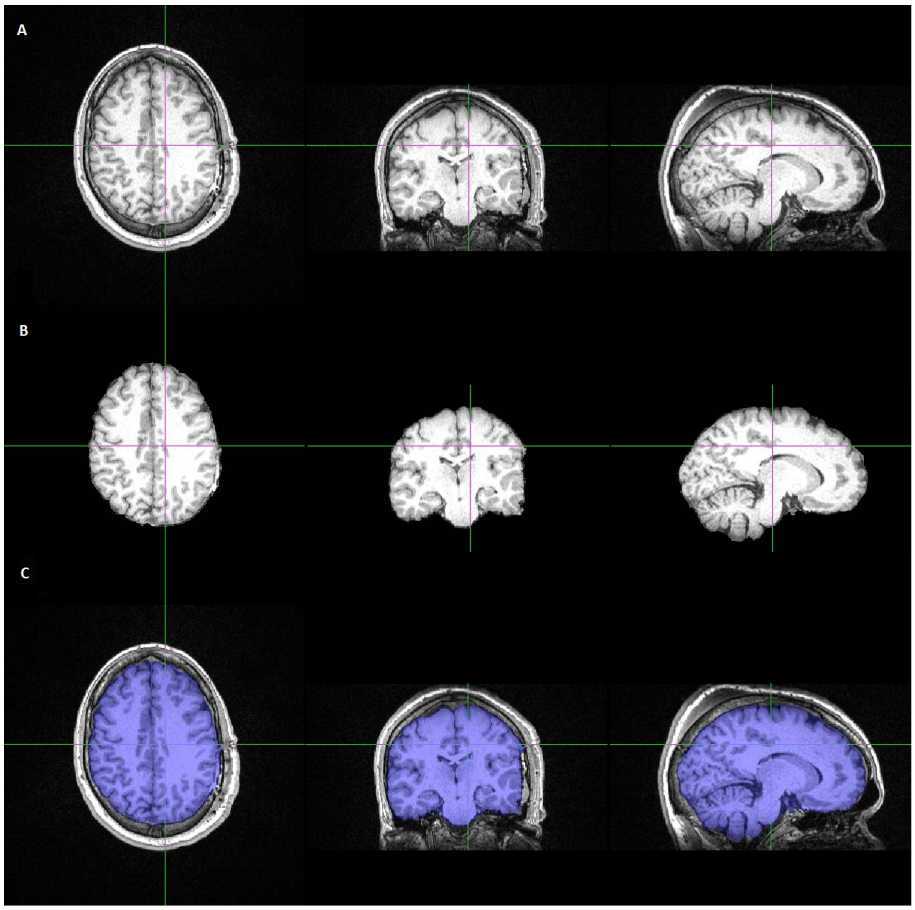

Figure 4.2: **A** - Post-operative T1-MRI; **B** - T1-MRI after skull stripping using BET and **C** - Fusion of the images in **A** and **B**, where the extracted brain is displayed in blue

4.1.2 Processing

4.1.2.1 Electrodes Segmentation

Co-registration of CT and skull-stripped T1-MRI were applied using a rigid body transformation with 6 DoF. The geometric transformation was applied using FLIRT with T1 as reference image.

Several parameters were needed to be defined, in order to provide a more accurate CT-MRI co-registration, as suggested in table 4.1. The angular range over which the initial optimization search stage is performed was set between -30 to 30 for the x, y and z axes. Since the motion between images was not significant, the chosen search values were lower to limit the image reorientation and thereby prevent unreasonable orientations. The cost function chosen responsible to

measure the difference between the two images and then minimizing it, was the normalized mutual information (NMI), an entropy-based cost function used for inter-modal alignment. Among the others cost functions provided in FSL, NMI is described as the one with more accurate results for inter-modal alignment and rigid multimodal registration [64].

Finally, for the final step in volume registration, the reslicing of the volume of interest, the interpolation method was not adjusted from the default option, since trilinear interpolation has been showing good results and a faster performance in other studies. [65, 66]

As a result, a CT dataset aligned with T1-MRI data was obtained as well as the transformation matrix which includes the x, y, and z translation, pitch, roll and yaw transformations. The accuracy of the co-registration was visually verified by flicking between the output and the reference images.

CT data was then thresholded and binarized to limit the image information to the electrodes only, which are shown in red in Figure 4.3. The threshold value was set to eliminate streak (beam hardening) artifact from the electrodes, brain and the skull.

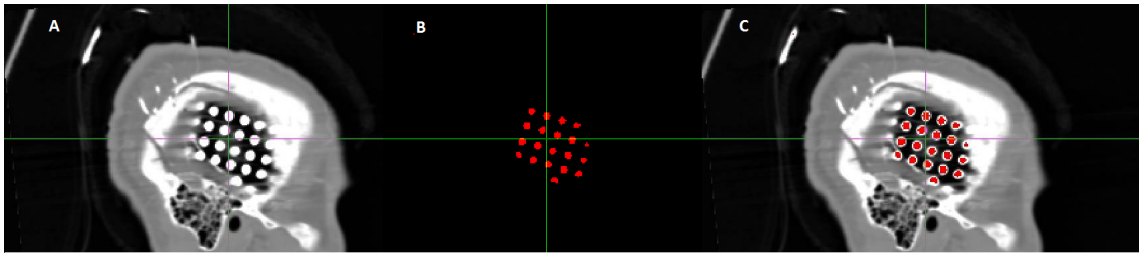

Figure 4.3: **A** - CT image with whole head; **B** - CT mask, after the thresholding and binarization **C** - Fusion of CT dataset with CT mask.

4.1.2.2 Cerebellum Segmentation

As cited in the introduction, cerebellum extraction was requested by HSJ to improve the visualization of the electrodes on the cortex.

To segment the cerebellum FIRST was used by selecting the values and options presented in the table 3.1.

Therefore, FIRST was implemented using the whole head T1-MRI image, the transformation matrix resulted by the two-stage affine registration, the mode of intensities of putamen for the intensity normalization and, specifying, 40 modes of variation for the optimization step.

The segmentation cerebellum mask resulted by FIRST was labelled with a value for interior voxels and +100 value for boundary voxels. For the classification of the boundary voxels, no boundary correction was selected as suggested in table 3.1. After that, the resulted image was marked with a single label and binarized.

To obtain a T1-MRI images without cerebellum the resulting masks, from left and right cerebellum were multiplied by T1-MRI dataset and then, subtracted to the same images.

In some cases the cerebellum mask doesn't cover the entire cerebellum and some of the bottom borders remain, after the subtraction step. This can be overcome with an addition tool, fslroi, to extract the resulted brain without the bottom borders.

4.1.3 3D multimodal fusion

For 3D visualization, T1-brain without cerebellum and electrodes mask were added to the MRIcron. Thereafter, the volume render option was selected to render a 2D projection of the 3D dataset.

In particular, in patient 3, some MRIcron options such as search depth and air/skin thresholding were studied more thoroughly for a better visualization of the electrodes.

4.2 Results and Discussion

As suggested by figure 4.2, when comparing skull-stripped T1-MRI (in blue) with the whole head it is observed that even using lower fractional intensity threshold to preserve the electrodes on the cortex skull removal was accurate performed. Although, in some slices some traces of CSF were observed. In cases in which pre-operative MRI is used and therefore, there are no electrodes, the threshold can be set to higher values. Figure 4.4 show the differences in the pre-operative T1 using different thresholds.

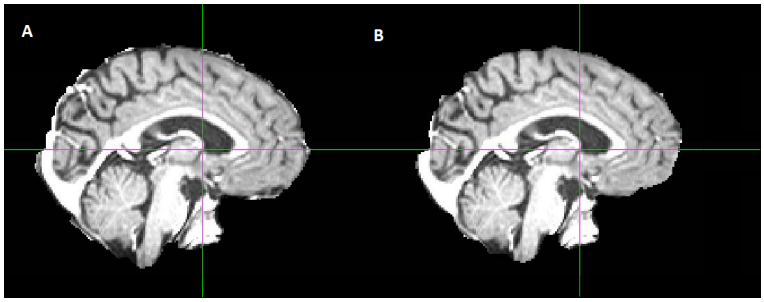

Figure 4.4: Skull-stripped pre-operative MRI from Patient 3 using **A** - a lower threshold and **B** - a higher threshold.

An example of resulting images of CT-MRI co-registration can be depicted in figure 4.5 (A). The figure suggests a fine alignment between CT and T1 datasets, as deduced at the frontal crest. Therefore, the choices made in the selection of the geometric transform, angular search range and cost function can be used in future FLIRT applications for CT-MRI co-registration.

Despite the developers of FLIRT tool have pointed failures in the alignment in the presence of large ventricles, the differences were not significant. As seen in figure 4.5 (B), the patient 3 has extremely large ventricles, so it would be expected a significant misalignment. However, the worst misalignment, seen at frontal crest in the slice presented in the figure, were not so distinguished. This suggests once again that the procedure adopted here for co-registration can be widely used, even in the presence of large ventricles.

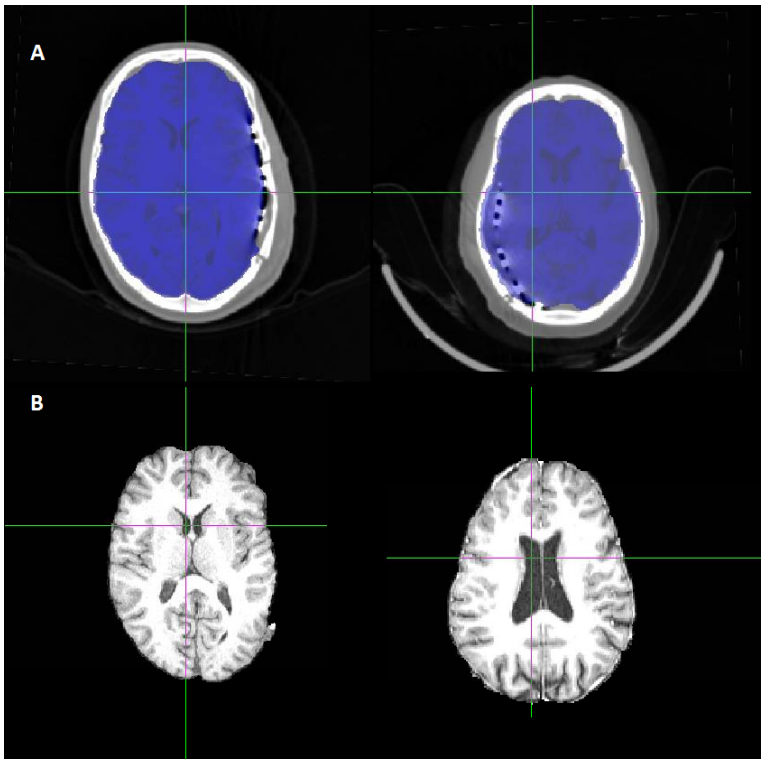

Figure 4.5: **A** - CT-MRI co-registration, using FLIRT, (left) in patient 1 and (right) in patient 3; **B** - T1 image, showing the size of the ventricles, in the corresponding patients.

The CT image aligned with T1 was then used for electrodes segmentation. The electrodes masks obtained for all the patients can be seen in figure 4.6. As evidenced by the figure, electrodes were correctly segmented from the CT images. The threshold used was capable to remove streak (beam hardening) artifact from the electrodes, brain and skull. The beam hardening removal is specially confirmed in the sagital view of patient 3.

Although, in this patient the threshold was set to a lower value in order to obtain the same accuracy of segmentation that was obtained with the other patients. Probably, the correction of the threshold was inevitable, as the imaging acquisition for this patient was carried in a different CT machine. Furthermore, in patient 2, an extra pre-processing step was performed. The values of the intensities were swapped, as shown in Figure 4.7 , so it was necessary to change the sign of the intensities. The swapped intensities may be due to a mistake taken by the software during the acquisition of the scans.

As previously mentioned to extract the cerebellum FIRST was used, in which it was indispensable the adjustment of some parameters. As shown in Figure 4.8, the cerebellum was not completely excluded. The masks resulted from FIRST didn't cover all the bottom borders of cerebellum. However, the upper borders, i.e., the ones in contact with the brain were correctly removed. In order to exclude the bottom borders, the additional tool, fslroi, was applied, as shown in Figure 4.9.

There are many possibilities that may have interfered in the cerebellum segmentation. First,

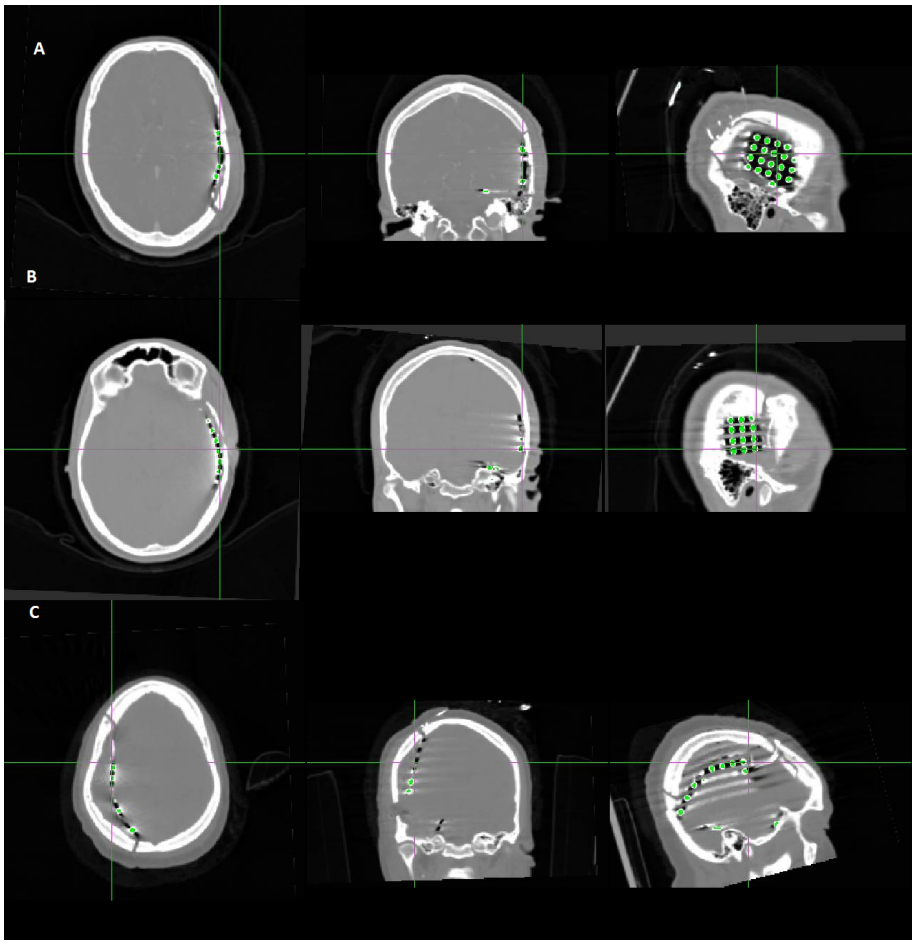

Figure 4.6: Fusion of CT dataset with CT mask, for **(A)** patient 1, **(B)** patient 2 and **(C)** patient 3 data.

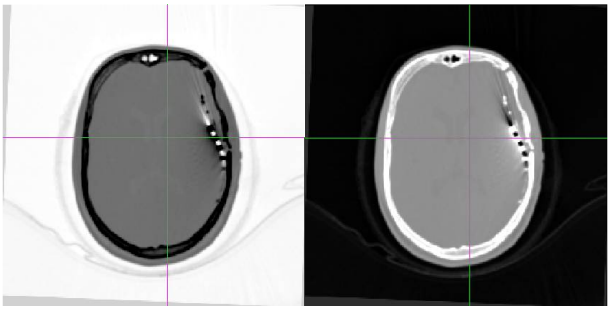

Figure 4.7: CT dataset from Patient 2. (Left) - Original CT image (Right) - CT image, after the correction of the sign of intensities.

FIRST uses a deformable model based in the variations presented in the 336 training images. Thus, the model can't represent variations in shape and intensity that are not explicit in the training data, so the topology of cerebellum may be constrained. Second, the performance of FIRST may be affected by several algorithm factors, such as: the ability of the multivariate Gaussian model represent correctly the shape/intensity probabilities; the ability of the optimization method;

mismatches between the real underlying ground truth and the manual labellings and the number of modes used in the fitting [62]. Finally, considering that for cerebellum the corresponding subcortical mask was not available the registration stage was incapable to concentrate only on the subcortical alignment, and the vertex positions of the 3D mean model and the corresponding cerebellum in the MRI of the patient may have been misaligned. Since to each vertex of the shape is associated a statistical variation, the variation of the bottom misaligned vertices may have limit the model adjustment for this region and therefore the resulting masks.

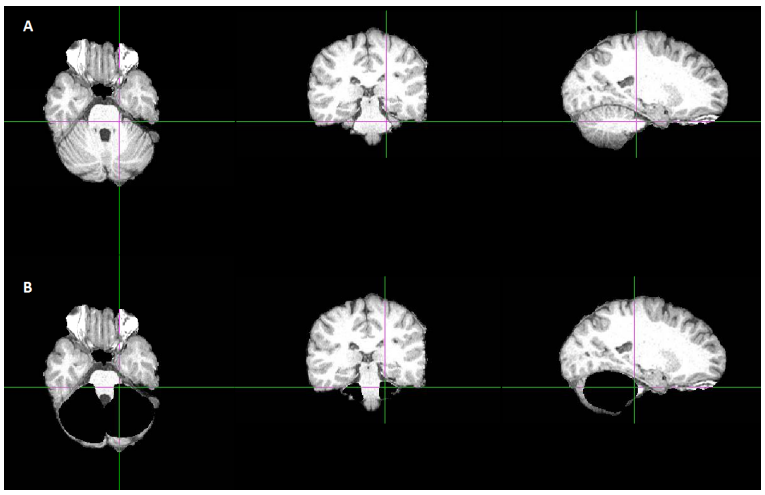

Figure 4.8: Cerebellum extraction: axial, coronal and sagital view of **(A)** the initial MRI **(B)** and the MRI, after FIRST segmentation and cerebellum removal.

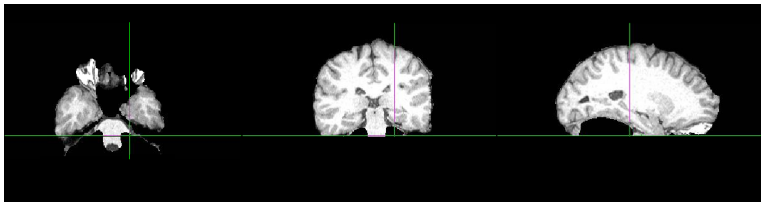

Figure 4.9: MRI without cerebellum: axial, coronal and sagital view of MRI after fslroi was applied.

At last, MR and CT datasets resulted by the above processing were used to create a 3D combined data model (Figure 4.10), using MRIcron. The results were approved by Dr. Ricardo Rego, as can be seen in section A.4, in the annex. The only setback was the loss of resolution, when displaying 3D by MRIcron, possibly due to the application of a Gaussian filter by the software. In addition, as referred in section 2.7, volume rendering depends highly of the parameters of the weighting functions, which in automatic rendering software such MRIcron is a drawback to the image quality. since no adjustments to these functions can be done.

In patient 3, the CT image showed a large swelling at the position where the electrodes were placed and therefore, the brain was compressed, as seen in Figure 4.6. Since T1-MRI image

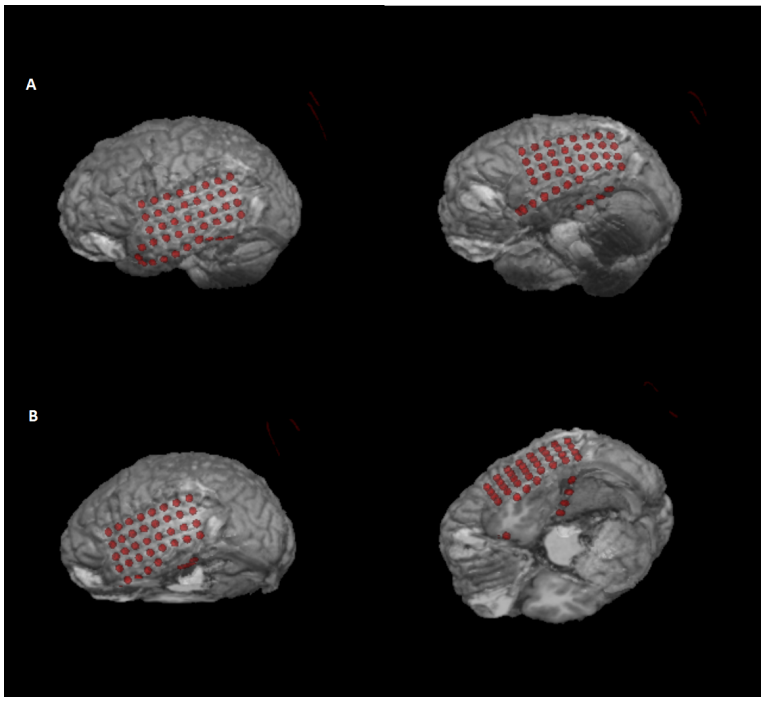

Figure 4.10: **A** - 3D visualization, using MRIcron, of skull-stripped T1-MRI, from the patient 1, with the electrodes mask. **B** - 3D visualization of skull-stripped T1-MRI without cerebellum, from the patient 1, with the electrodes mask.

used was pre-operative and so no edema was present the overlay of the electrodes, from post-operative CT mask, on the cortex, from pre-operative T1 dataset, in a 3D model was limiting the visualization of the electrodes position in relation to the surrounding tissues. However, varying the search depth of the overlay, (Figure 4.11), in MRIcron, made possible to the physician to see the electrodes and therefore, do the anatomic relation of electrodes position with the surrounding tissues.

From all the data used in the Epilepsy scenario, our results were not used in the first two patients for the clinical decisions since they were used as test examples to validate the pipeline. After the validation, our results were used for patient 3 in the pre-neurosurgical evaluation. Patient 3 who had, on average, more than a seizure a week, since surgery, performed one month ago, has been seizure-free.

This outcome is an excellent result for the pipeline developed, since the patient 3, when compared with the others patients results, was the one in which the 3D representation was more limited by the presence of the edema.

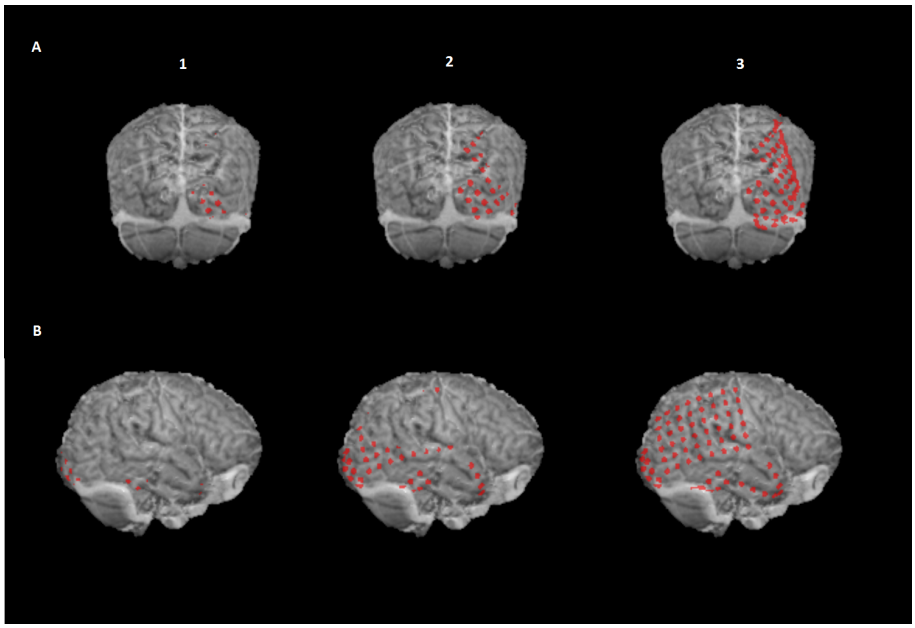

Figure 4.11: 3D model for patient 3 dataset, using MRIcron, where **(A)** corresponds to an posterior view and **(B)** a lateral view of brain. **(1)**, **(2)** and **(3)** corresponds to different search depths, 2mm, 12mm and infinitive depth, respectively.

Chapter 5

DBS Scenario

For the DBS patients it was intended to delineate STN and GPi to support in the pre-neurosurgical evaluation prior implantation and to confirm the position of the electrodes in these target areas after the surgery. Furthermore, it was proposed to determine the proximity of each electrode to the target areas and others in the deep brain area to establish a correlation with the patients' outcome. In this chapter it will be explained the several steps for the detection of the DBS electrodes and for the segmentation of DBs as well as a detailed discussion of the results.

5.1 Methods

Eight patients with advanced PD and eight patients with focal Dystonia, undergoing DBS were chosen to this study. The patients were operated under local anesthesia and the electrodes were implanted in the STN or GPi by MRI-guided stereotaxy. All the patients had electrodes implanted bilaterally.

The DBS lead position was confirmed by a post-operative CT or T2 scans. A pre-operative whole head T1-MRI with 0.98 x 0.98 x 1mm of voxel size was also acquired to guide the surgery and to visualize the target structure. The MRI images were gathered by a 3T-MRI unit(Sigma Exite MD GE). CT scans were acquired by GE scanner, Brightspeed16 unit. For the implantation a quadripolar electrode array was used (model 3389, Medtronic Neurological Division,Minnesota, USA) with 4 electrodes at the tip, spaced 0.5mm apart, delivering stimulation individually or in combination.

The workflow adopted is summarized in the diagram 5.1, which was inspired in [8]. Section A.5 of the annex presents in more detail the several steps of the workflow.

5.1.1 Preprocessing

FSL was used to perform co-registration and skul stripping. Considering that FSL does not support Dicom files all the data provided were converted to NIfTI format using MRIcron.

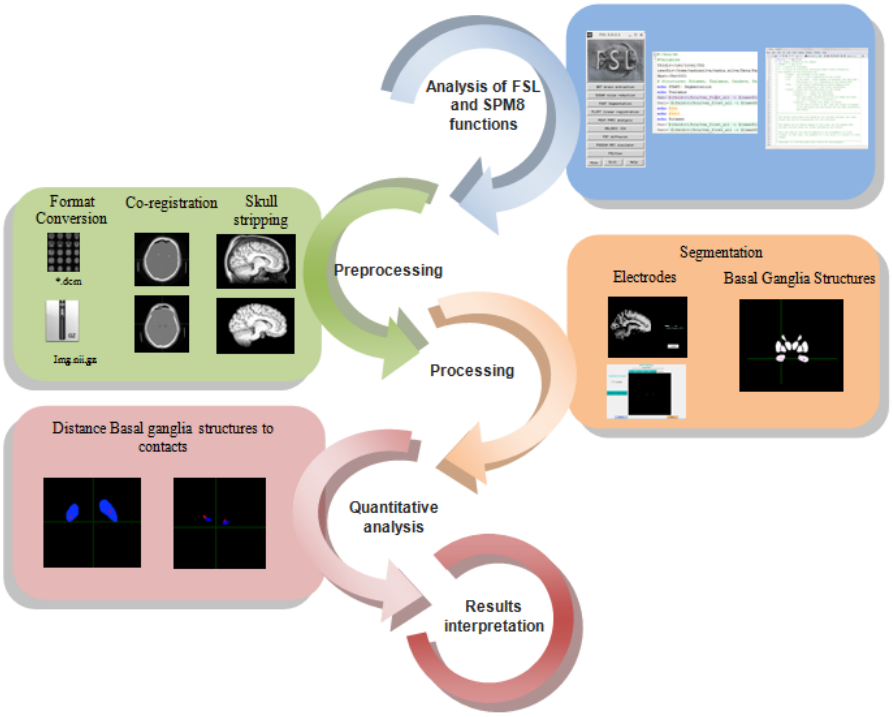

Figure 5.1: Workflow adopted for the DBS cases, describing the several steps performed.

For co-registration of CT or T2 scans with T1 as reference image, FLIRT was applied using a rigid body transformation with 6 DoF. Parameters such angular range search, cost function and interpolation method were the same as in Epilepsy study. No adaptations were performed in the procedure since, as in Epilepsy scenario, the motion between images was not significant, NMI method results in a better inter-modal alignment using rigid body registration and trilinear interpolation is the fastest method.

Nonetheless, before co-registration BET was applied in the T1 datasets to extract the skull, which is a pivotal step prior FLIRT application, since FLIRT algorithm only run with brain extracted images. Different fractional intensity thresholds were tested to get a highly accurate skull removal. Lower thresholds were incapable to remove the skull completely and higher threshold were leading to the loss of some brain tissue, in particular cortex. Therefore, a medium threshold was preferred.

5.1.2 Processing

For DBS lead segmentation and consequently the detection of its electrodes, MATLAB was chosen as the appropriate platform to develop the required algorithms, since the data can be easily manipulated.

Considering that the files resulted from FSL during the pre-processing stage were in NIfti format, and no function in MATLAB is capable to read this type of data, SPM package was loaded. Using SPM the header and the image dataset of each NIfTi file was read.

Enhancement of the images can be achieved using different types of operators, namely the punctual operators known as intensity transformation functions. In order to improve the contrast of the provided images a linear stretching was applied to CT and T2 images. For T1 datasets the linear stretching was defined to promote the expansion of the higher intensities and thereby enhance the visualization of the different structures in the brain. Furthermore, a median filter was used on T1 images to reduce salt and pepper noise. No filters were implemented in CT and T2 datasets due to the induced blur that was promoting the disguise of the bottom tip (BT) of the DBS lead.

5.1.2.1 DBS lead Segmentation

A binary mask with only the DBS lead is crucial to detect its BT and thereby each position of the electrodes. An automatic algorithm was developed to do the DBS lead segmentation. The algorithm can be divided in two main steps, as listed below:

- Intensity threshold and skull removal;
- 3D labelling connected components algorithm.

In the first step all the CT or T2 images were binarized by an intensity threshold, chosen after an inspection of the histogram. Since in T2 the lower intensities correspond to the DBS lead, as opposed in CT images, a morphological operator was applied. Therefore dilation was carried in the T2 masks, resulted from the threshold, to obtain a brain mask without the lead. To this mask the original binary mask was subtracted, and consequently an DBS lead segmented image was obtain, as in CT images (figure 5.2 (B)).

The application of the threshold should allow the extraction of the DBS lead and the removal of brain and skull. Nevertheless, skull was not completely eliminated due to is similar intensities with the lead. As a result an additional step was required.

For each binary image of the dataset, (figure 5.2 (B)), a new image was estimated, in which a label was assigned for each connected component. The area and solidity of each label were determined. The connected components with larger area and with a solidity above 0.5, refined after some tests, were assumed to be skull and consequently removed from the binary image. In T2-MRI case, this process was repeated two times to remove inner skull and outer skull. As opposed in CT datasets, where inner skull and outer skull are not distinguishable, and therefore the procedure was only performed one time. Although this process almost removed the whole skull, some residues of skull and other structures remained, specially in T2-MRI (figure 5.2 (C)). Considering that the aim of DBS lead segmentation is to obtain a mask in which only the lead is present in order to detect its BT, the second step of the automatic segmentation was developed, a 3D labelling connected components algorithm.

In this algorithm the DBS lead 3D mask is estimated based on the principle that the position of the lead varies slightly from slice to slice. The main steps for the development of this algorithm are listed below:

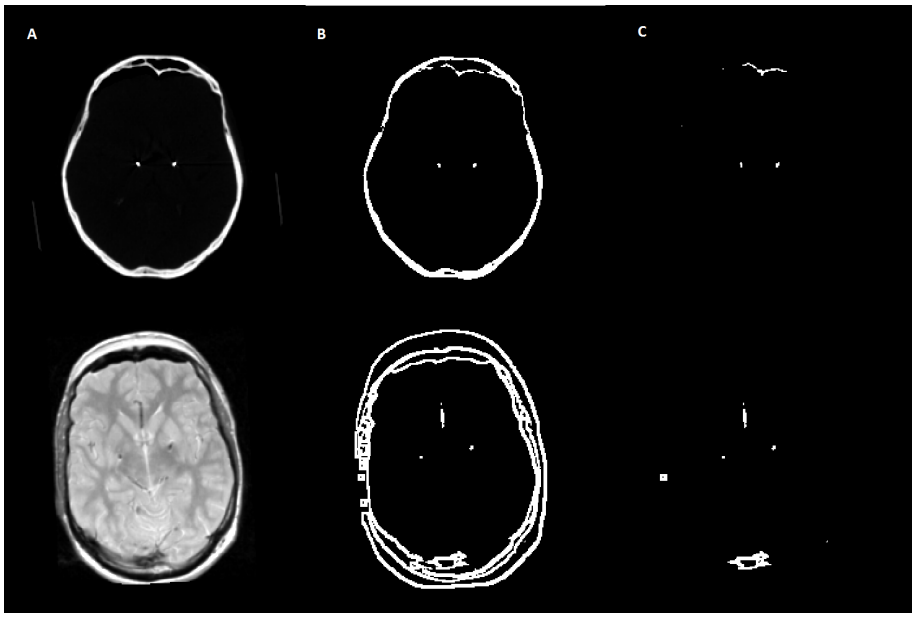

Figure 5.2: CT (above) and T2-MRI (below) **(A)** after the enhancement process; **(B)** after the intensity threshold was applied and, for the case of T2 datasets, after the intensity threshold and the subtraction of the brain mask were performed; **(C)** after the skull removal, based on solidity and area of the 2D connected components.

- Centroid estimation;
- Distance of each centroid to the centroids in the following slice;
- Keep the combination with minimum distance;
- Distance thresholding;
- Isolated centroids combination removal;
- Centroid connectivity;
- 3D labelling connected components establishment;
- Selection of DBS lead connected components or labels.

First, the centroid of each label on each slice of the segmented mask, (figure 5.2 (C)), was estimated. The Euclidean distance between centroids from consecutive slices was determined for every possible combination, as suggested in figure 5.3 (A). However, only the combination with minimum distance was saved, such that each centroid is only connected to a single centroid in the following slice, (figure 5.3 (B)). The combination of consecutive centroids that might represent the 3D lead mask are not missed by keeping only the combination with minimum distance, since the position of the lead varies slightly from slice to slice. In addition, this condition makes the computational cost of the process in the following steps less expensive and feasible in terms of time and memory.

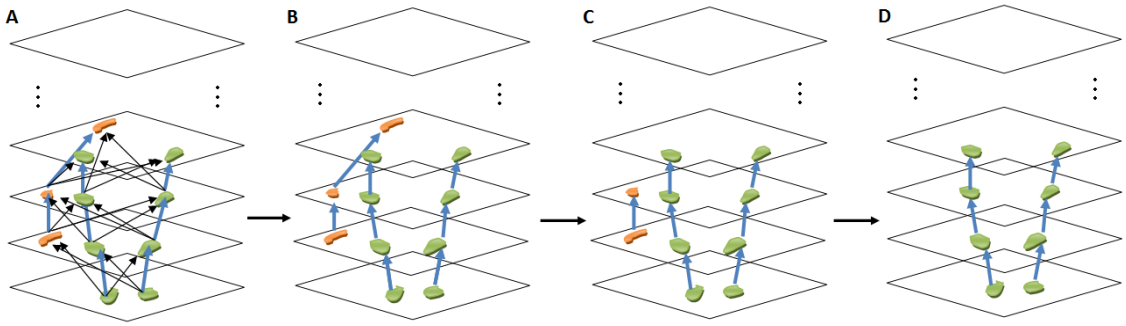

Figure 5.3: Illustration of the five initial steps of the algorithm **A** - Representation of the distances of the centroid of each connect component to the ones in the follow slices; **B** - The combination of centroids with minimum distances; **C** - Combination of the centroids after the distance thresholding was applied; **D** - Removal of the combination of centroids which were isolated, without connectivity.

Then, a distance thresholding was applied to eliminate 3D centroids combinations which are far apart and has no meaning for this work. As a result some centroids lose the connectivity to the following slice, leading to isolated centroids combination, which were then removed, as represented in figure 5.3 (C) and (D).

After the centroid connectivity between successive slices was established, a recursive function connected the centroids based in their relation to the following slices and sets up the 3D connected components, each one with a different label assigned. Since each centroid is connected to only one centroid in the following slice, the issue of having centroids repeated in different connected components is avoided. The recursive function ends the set up of each connected component when a centroid has no connection with any centroids on the next slide. When all the centroids have a label assigned and thus integrated into a 3D component the recursive function cease.

3D labels which occupied more slices correspond usually to each DBS lead implanted, since the leads are localized almost along the entire brain, occupying more slices than others 3D labels, which were punctual residues that were not removed by the first step of the automatic algorithm.

Using this two steps algorithm a mask of the leads without any residues of skull and other structures can be selected from all the 3D connected components obtained. Then x, y and z voxel positions of the BT and upper tip (UT) of each lead is determined and used to generate a representative straight line of the DBS lead, which is required to measure each electrode position by a trigonometric deduction.

For the case of automatic segmentation does not produce accurate results, a semiautomatic segmentation was developed. In the semiautomatic method the user can examine the original CT or T2 scans and place a cursor over the BT and UT to select them. Then the x, y and z voxel coordinates resulted from the cursor selection are saved to be used for the measurement of each electrode position by a trigonometric deduction.

Voxel to mm space

Saved in the header of the NIfTI file is an 4x4 affine transformation matrix to convert the voxel coordinates in millimeter (mm) coordinates or vice-versa. Assuming the follow matrices, M and M^{-1}, as the 4x4 transformation matrix and its corresponding inverted matrix, the transformations between space coordinates are expressed in the equations 5.1 and 5.2.

$$\mathrm{M} = \begin{pmatrix} x_{1,1} & x_{1,2} & x_{1,3} & x_{1,4} \\ x_{2,1} & x_{2,2} & x_{2,3} & x_{2,4} \\ x_{3,1} & x_{3,2} & x_{3,3} & x_{3,4} \\ x_{4,1} & x_{4,2} & x_{4,3} & x_{4,4} \end{pmatrix} \qquad M^{-1} = \begin{pmatrix} x'_{1,1} & x'_{1,2} & x'_{1,3} & x'_{1,4} \\ x'_{2,1} & x'_{2,2} & x'_{2,3} & x'_{2,4} \\ x'_{3,1} & x'_{3,2} & x'_{3,3} & x'_{3,4} \\ x'_{4,1} & x'_{4,2} & x'_{4,3} & x'_{4,4} \end{pmatrix}$$

$$\begin{bmatrix} x_{mm} \\ y_{mm} \\ z_{mm} \end{bmatrix} = \begin{bmatrix} x_{voxel} \\ y_{voxel} \\ z_{voxel} \end{bmatrix} \times \begin{bmatrix} x_{1,1} & x_{1,2} & x_{1,3} \\ x_{2,1} & x_{2,2} & x_{2,3} \\ x_{3,1} & x_{3,2} & x_{3,3} \end{bmatrix} + \begin{bmatrix} x_{1,4} \\ x_{2,4} \\ x_{3,4} \end{bmatrix} \tag{5.1}$$

$$\begin{bmatrix} x_{voxel} & y_{voxel} & z_{voxel} \end{bmatrix} = \begin{bmatrix} x_{mm} & y_{mm} & z_{mm} \end{bmatrix} \times \begin{bmatrix} x'_{1,1} & x'_{1,2} & x'_{1,3} \\ x'_{2,1} & x'_{2,2} & x'_{2,3} \\ x'_{3,1} & x'_{3,2} & x'_{3,3} \end{bmatrix} + \begin{bmatrix} x'_{1,4} & x'_{2,4} & x'_{3,4} \end{bmatrix} \tag{5.2}$$

Electrodes Localization

After DBS lead segmentation the x, y and z voxel coordinates of its BT and UT are transformed to mm by the equation 5.1. In order to detect the exact position of the electrodes a trigonometric relation were deduced and illustrated in figure 5.4. Assuming that δx, δy and h are the distances in mm between the BT and UT in x, y and z axes and H is the direction of the DBS lead, it will be demonstrated the measurements required to determine the x, y and z positions for an figurative electrode, H1.

Therefore the equations performed to obtain the x, y and z mm coordinates, δx1, δy1 and h1, for the figurative H1 electrode are listed below:

$$\alpha = \tan\left(\frac{\delta y}{\delta x}\right)^{-1} \tag{5.3}$$

$$d = \frac{\delta x}{\cos(\alpha)} \tag{5.4}$$

$$\beta = \tan\left(\frac{h}{d}\right)^{-1} \tag{5.5}$$

$$H = \frac{d}{\cos(\beta)} \tag{5.6}$$

$$\varphi = \frac{h}{\cos(\varphi)} \tag{5.7}$$

$$d1 = \cos(\beta) \times H1 \tag{5.8}$$

$$\delta x1 = \cos(\alpha) \times d1 \tag{5.9}$$

$$\delta y1 = \sin(\alpha) \times d1 \tag{5.10}$$

$$h1 = \cos(\varphi) \times H1 \tag{5.11}$$

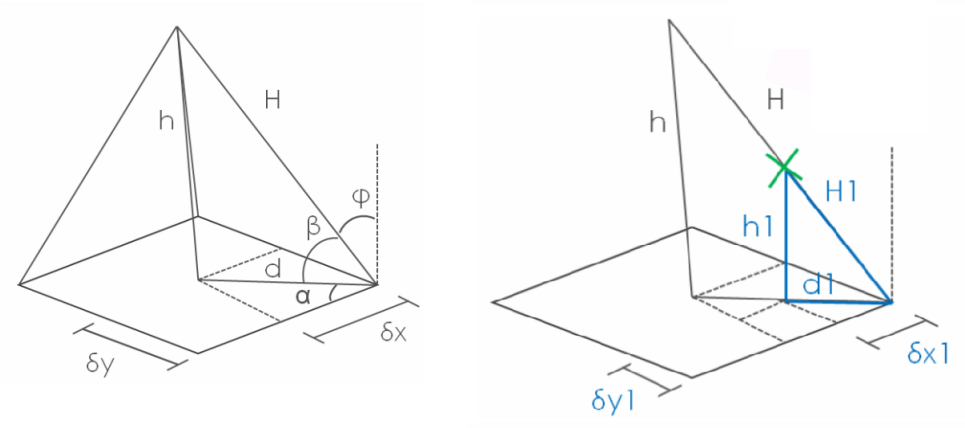

Figure 5.4: 3D representation of the relationships between the lengths and angles for the different sides of the DBS lead.

Based on the datasheet of the DBS lead used in this study, the distances along H for each electrode in relation to the BT are the follow: 2.25, 4.25, 6.25 and 8.25mm [2]. To determine the δx1, δy1 and h1 of each electrode, the value of H1 was adjusted in the above equations to each of these distances provided in the datasheet.

Then, the positions of each electrode are transformed to voxel coordinates, using equation 5.2. Since voxels only take integer values, the coordinates were rounded to the nearest value and then used to create a mask of the electrodes.

Considering that in the case of the automatic segmentation the DBS lead mask was estimated, only the z voxel coordinates (slice numbers) of each electrode was used to mark, in this mask, the labels which correspond effectively to the presence of the electrodes. Therefore, a new dataset of binary images was established in which only the slices of the DBS lead mask in which the electrodes were identified were marked.

As opposed in the semiautomatic segmentation, considering that no DBS lead mask was generated the x, y and z voxels coordinates of the centroid estimated for each electrode were used as center of the electrode. A circle was produced around this centre, with a radius of 1.38 in voxel coordinates. Such radius corresponds to the mm radius of the electrode given by the datasheet.

Furthermore, since the values for H1 are estimated in relation to the BT, the precise localization of this tip is essential for the accurate localization of each electrode. In addition a precise identification of the UT is not vital, since by selecting other point on the DBS lead is also possible to estimate its trajectory.

5.1.2.2 Interface

Additionally to the objectives proposed it has become necessary to create an interface in MATLAB to assist the user in several tasks such as: the choice on the type of image to process, the type of segmentation to use and the adjustment of some parameters to optimize the process.

Thus the developed interface provides the following options:

- Reading and pre-processing the datasets;
- Automatic or semiautomatic segmentation;
- Estimation of the masks of the electrodes;
- Exporting datasets;
- Optimization of parameters.

The first task allows the user to choose the type of data to read (CT, T1 or T2) and apply the pre-processing stage. After reading the dataset the user can analyse it, for instance by verifying the position of the BT. The images can be explored by passing one slice at a time or by passing 10 slices at once, using the upper buttons. In this initially phase the user can also export the contrasted images (figure 5.5).

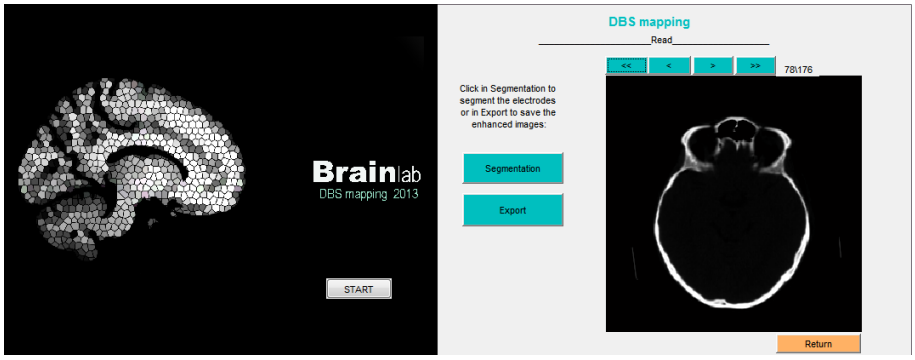

Figure 5.5: (Left) The initial window of the interface (Right) Interface after the choice of the of dataset, in which the upper buttons can be used to pass the slices and the lateral ones to proceed to segmentation or exportation.

If the automatic segmentation is chosen the program will run the algorithm described in section 5.1.2.1, exposing visually the UT and BT estimated for each lead (figure 5.6 (left)). If the user agrees with the suggestion given automatically, the mask of the electrodes are generated and presented for exportation. However, if the tip does not match the BT checked by the user initially, an adjustment of parameters for the automatic segmentation is available. Nevertheless, semiautomatic segmentation can also be chosen if the user is not satisfied with the suggestion given by the automatic algorithm.

When the semiautomatic segmentation is chosen the user can select the UT and BT directly on the slices, and the mask of the electrodes are automatically generated (figure 5.6 (right)). Thereafter, the masks can be exported as Dicom files. The interface also allows the user to overlap the structural T1-MRI image with the DBS lead and/or electrodes masks for a better verification of the segmentation step, figure 5.7. This overlapping is possible since CT images were initially aligned with T1 using FLIRT, as referred in section 5.1.1. Furthermore, there is in the program an instruction panel to assist the user in the several options of this interface.

Figure 5.6: (Left) Interface window after the automatic segmentation is performed, in which the user can verify the DBS lead segmentation and the positions of the BT and UP; (Right) Interface for semiautomatic segmentation, in which the user press in the lateral buttons and using the cursor selects the BT and UP.

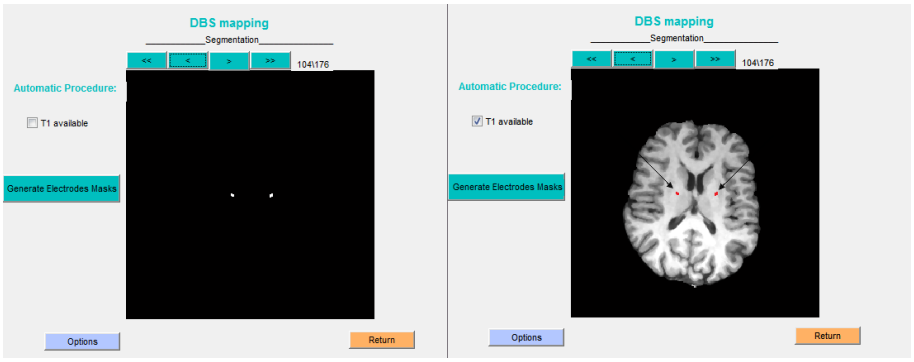

Figure 5.7: Automatic segmentation: Electrodes mask (Left) without the corresponding T1-MRI and (Right) overlaid with T1-MRI.

As shown in figure 5.8, for the optimization of the process the intensity threshold used in the first step of the automatic segmentation of the DBS lead can be adjusted as well as some specifications of the lead, such electrode length, electrode spacing, electrode distance, distal tip, lead diameter and length lead.

Figure 5.8: Interface window with several options to optimize DBS lead segmentation or change the DBS lead specifications for (Left) the automatic or (Right) the semiautomatic segmentation.

Image exportation

To export the resulting images and masks, a function was developed to write the 3D data as a stack of 2D slices in separate Dicom files with the header of the original NIfTI file.

5.1.2.3 Deep Brain Structures Segmentation

As in section 4.1.2.2, FIRST was used to segment some DBs, namely amygadala, caudate nucleus, hippocampus, nucleus accubens, pallidum, putamen and thalamus. The parameters prior verified by FIRST developers which lead to accurate results and listed in the table 3.1 were used for this work. [61, 62]

In opposition to cerebellum segmentation, the second stage of the affine registration of T1-MRI to the MNI-152 space was carried using subcortical masks, allowing the exclusion of voxels outside the subcortical regions and a better subcortical alignment.

The centre-of-gravity or centroid of each structure on each side of the brain was estimated to compare with the positions of the electrodes and then with patients' outcome. For this estimation, fslstats, a volumetric analysis tool of FSL was used.

Since in the pre-neurosurgical evaluation some physicians prefer the information in a common template, all the segmented structures were warped to the MNI space.

Therefore, T1-MRI datasets were warped to the MNI template using a linear followed by a non-linear registration to overcome the inter-subject anatomical differences in shape, size, and relative orientation, as referred in section 2.4.2. This registration was carried out using an affine transformation with 12 DoF to guarantee the topological integrity of the original image, as cited in section 2.4.1. For the linear transformation, trilinear interpolation, NMI cost function and a angular search range of -30 to 30 were used due to the reasons mentioned for CT-MRI or T2-T1 co-registration. FNIRT was applied in the T1-MRI datasets using the matrix resulted from the affine transformation with 12 DoF, in order to obtain a warp-field, which is basically a set the displacements to place the initial T1-MRI in the MNI space. Then, the warp-field was applied in the segmented structures to warp them to the MNI space.

5.2 Results and Discussion

As depicted in figure 5.9, when comparing skull-stripped T1-MRI (in blue) with the whole head it is deduced that the threshold defined to these datasets was capable to preserve the cortex and remove completely the skull.

Figure 5.10 revealed a fine alignment between T1 and T2 or CT images. Therefore, the parameters chosen for the co-registration are recommended for inter-modal alignments, rigid body transformations and datasets in which the motion is not significant.

Despite the patients of this study were elderly and therefore more susceptible to present large ventricles, no failures were seen in FLIRT performance.

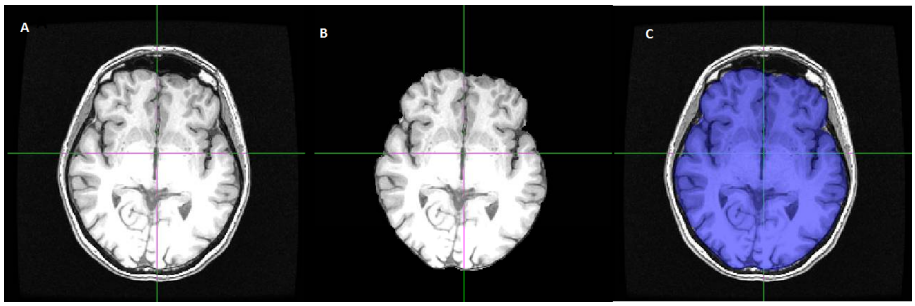

Figure 5.9: **A** - Pre-operative T1-MRI; **B** - T1-MRI after skull stripping using BET and **C** - Fusion of the images in **A** and **B**, where the extracted brain is displayed in blue.

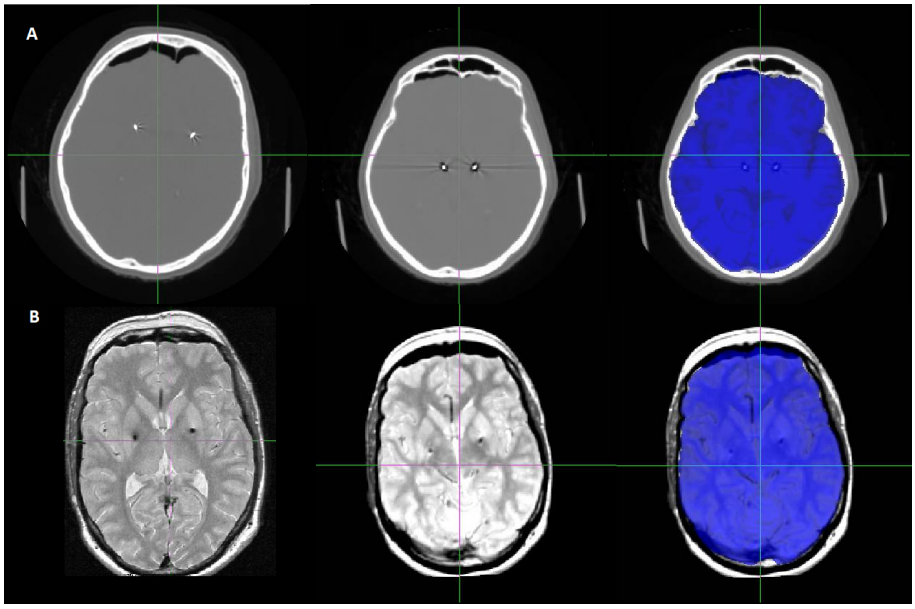

Figure 5.10: Co-registration of **(A)** CT with T1 datasets and **(B)** T2 with T1 datasets. (Left) Original CT and T2 images; (Center) CT and T2 images aligned with T1 using FLIRT; (Right) Fusion of CT or T2 images with T1, which is displayed in blue.

Electrodes Segmentation

The CT or T2 datasets aligned with T1 was then used in MATLAB for electrodes segmentation. As verified in figure 5.11 (A), 3D labelling connected components algorithm was efficient to produce a mask with only DBS lead data. For the CT images, no residues of other structures distinguished in the figure 5.2 (C) were seen in the DBS lead mask, after the appliance of the second step of the automatic algorithm. Nevertheless, in the case of DBS lead segmentation for T2 datasets, it was observed that usually the segmentation for one of the leads implanted of the brain was correctly performed but the other lead was not identified and mistaken with other brain region, as shown in figure 5.12. The principle in which 3D labels that occupied more slices correspond to the leads is not observed in T2 datasets, probably due to an ineffective performance by the first step of the automatic algorithm to remove the maximum of skull and structures not belonging to the DBS lead. In the majority of the cases, the other 3D connected component seen after the automatic

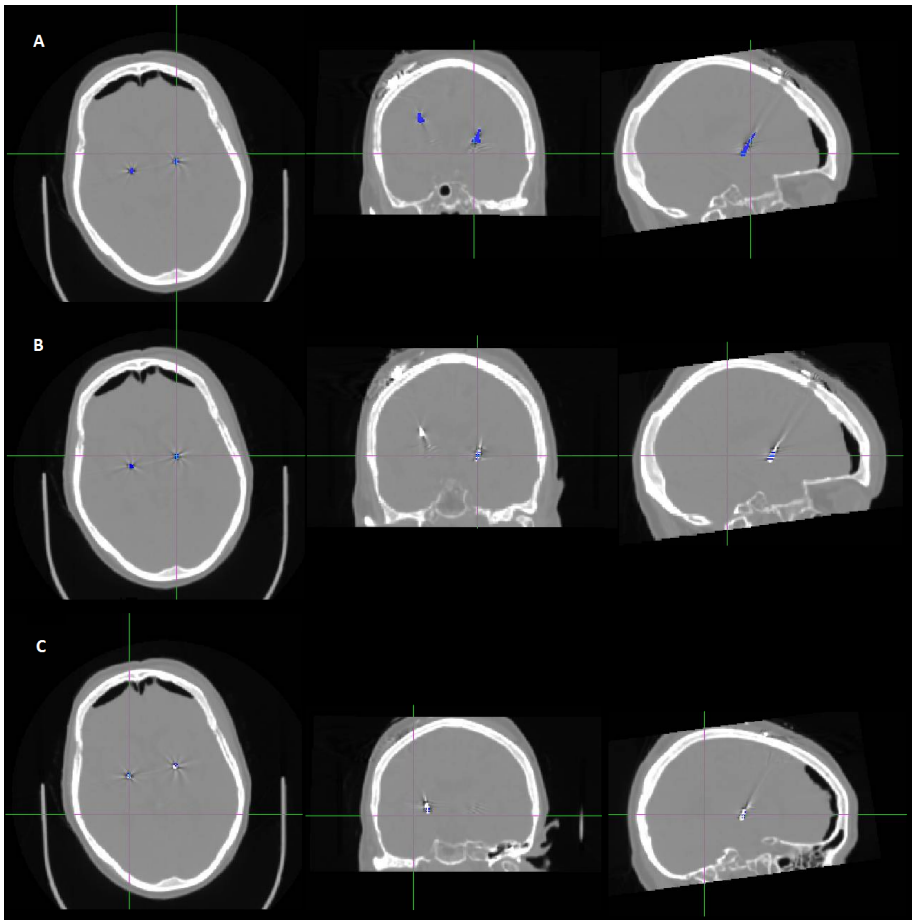

Figure 5.11: Fusion of CT images with: **(A)** The DBS lead mask obtained after the 3D labelling connect components algorithm; **(B)** electrodes mask obtained by the automatic algorithm; **(C)** electrodes mask obtained by the semiautomatic algorithm.

segmentation algorithm was a region near the occipital skull with lower intensities. Thereby, for T2 datasets only the semiautomatic segmentation was used to generate the electrodes mask. For CT images the automatic segmentation method provided good results.

Some examples of electrodes mask overlaid with CT image are presented in 5.11 (B) and (C). As depicted in the figure 5.11, in particular in axial view, when using the automatic method the electrodes are correctly overlaid on the lead of the CT image. In contrary, the electrodes resulted from the semiautomatic method show some displacements in relation to the lead.

As the electrodes are displaced from the DBS lead, it can be concluded that the representative straight line of the lead produced after the selection of the UT and BT was not precise. This imprecision may be due to random errors introduced by the user in the selection of the tips and systematic errors due to the voxel resolution, restricting the selection of the center of the tips by the cursor.

Regarding the automatic method the line representative of the DBS lead was produced based on the tips of the DBS lead mask returned by the algorithm. However, since in the upper slices a increased beam hardening has identified is possible to conclude that the estimation of the cen-

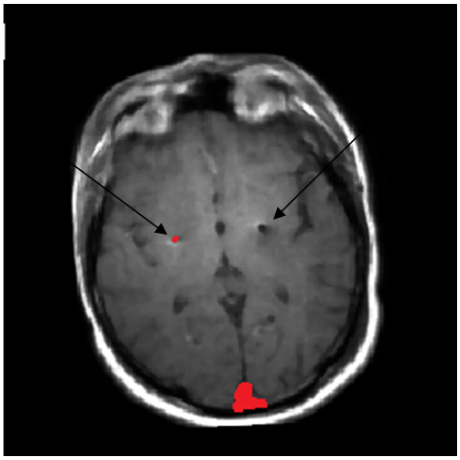

Figure 5.12: Overlay of T2 images with the DBS lead mask obtained with the 3D labelling connected components algorithm.

troid for the UT was affected and leading to some errors in the representation of the trajectory of the lead, and therefore in the estimation of each electrode position. However, no displacements between the electrodes mask and the DBS lead were seen, when the automatic method was used, since the electrodes mask was created based on the DBS lead mask for the z position or slices in which each electrode was found.

The electrodes position were also estimated by Dr. Verena Rozanski. Using the FSL viewer environment the BT coordinates were identified manually as well as the angles between the DBS trajectory and the horizontal plane and sagital plane. Then, the electrodes position were estimated by a set of trigonometric relations.

The electrodes position given by MATLAB and the estimated by Dr. Verena were compared, in order to validate the MATLAB algorithm.

Primarily, it was observed a systematic difference in the identification of the BT for some cases. The parameters chosen for the automatic segmentation were defined to assume the presence of the BT at the first identification of the lead. Similarly, using the semiautomatic method, the manual selection was always made in the slice in which the first evidence of the lead was detected. However, this consideration was not assumed by the collaborated physician in this study, since in her opinion the first slices may correspond to artefacts and not to the lead. As can be seen in figure 5.13, the manual identification of the BT in FSL by the physician was systematically higher by 1,2 or 3 mm than the considered in MATLAB.

As suggested by the figure 5.13, the automatic algorithm is very sensible for the detection of the BT as the first point with higher intensities. Although, in the case of the first slices may correspond to artefacts, they can be avoided by adjusting the intensity threshold on the options of the interface, and therefore diminish the sensibility in the detection of the BT, assumed by the interface developers.

Due to these systematic differences, a "normalization" step was performed in the electrodes position given by MATLAB and by Dr. Verena Rozanski for an appropriate validation of the MAT-

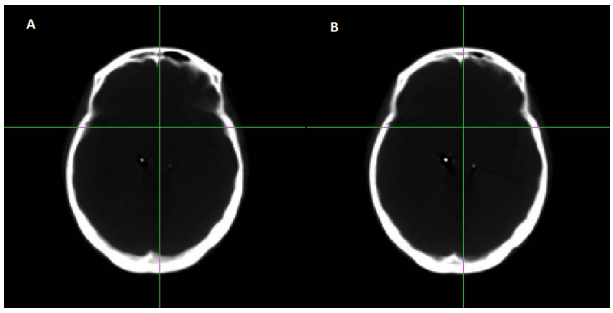

Figure 5.13: Left BT location: **(A)** detected by the automatic algorithm and **(B)** estimated in the FSL viewer environment by the expert. In this case, the bottom tip estimated by the MATLAB was 2mm above the one defined manually.

LAB algorithm. All the x, y and z coordinates of electrodes were subtracted to the coordinates of the BT, in order to obtain normalization distances for each axis and each electrode, regardless of the BTs selected. Then the normalization distances obtained with MATLAB were subtracted to the normalized ones by Dr. Verena Rozanski. The absolute value of these differences can be examined in the tables 5.1 and 5.2.

Table 5.1: The mean and standard deviation of the absolute differences estimated from all dataset, regardless the method of segmentation used for the electrodes mask establishment.

	x (mm)	y (mm)	z (mm)
Mean	0,507	0,592	0,444
Standard deviation	0,337	0,426	0,366

Table 5.2: The mean and standard deviation of the absolute differences estimated with the automatic and semiautomatic method.

	Semiautomatic			Automatic		
	x (mm)	y (mm)	z (mm)	x (mm)	y (mm)	z (mm)
Mean	0,581	0,557	0,359	0,385	0,678	0,587
Standard deviation	0,362	0,358	0,316	0,258	0,530	0,413

Through the analysis of these tables it is concluded that the differences between the electrodes measured by Dr. Verena Rozanski and the ones resulted by MATLAB are very low. The semiautomatic segmentation shown better results for the y and z directions when compared with the automatic method, probably due to the trajectory of the DBS lead that was less imprecise. Although, using the automatic algorithm and therefore the DBS mask to create the electrodes mask, the x directions is less affected.

Despite these considerations, the trajectory imprecisions, either with automatic method or the semiautomatic, are not significant since the differences are lower than the image resolution, 0.98 x

0.98 x 1mm and thereby less than a voxel dimension. The normalization distances acquired with MATLAB and Dr. Verena Rozanski can be consulted in the section A.6 of the annex.

Deep Brain Structures Segmentation

Concerning BG segmentation, the main results are presented in the figures 5.14 and 5.15. In general, the masks were larger than the corresponding structures, in particular for the thalamus. The shape of the mask and the structures are very congruent, as shown in 5.14 for the caudate nucleus and putamen and in 5.15 for the hippocampus, nucleus accubens and pallidum.

Some structures such pallidum and amygdala are almost imperceptible in the individual space and even after the two-stage affine registration to MNI-152 space. Nevertheless, they were accurately segmented possibly due to the Bayesian framework. Since it allows to do probabilistic relationships between shape and intensity variations across the training stage, the pallidum and amygdala segmentation were possibly estimated based on the shape and position of others structures more well defined such putamen and hippocampus.

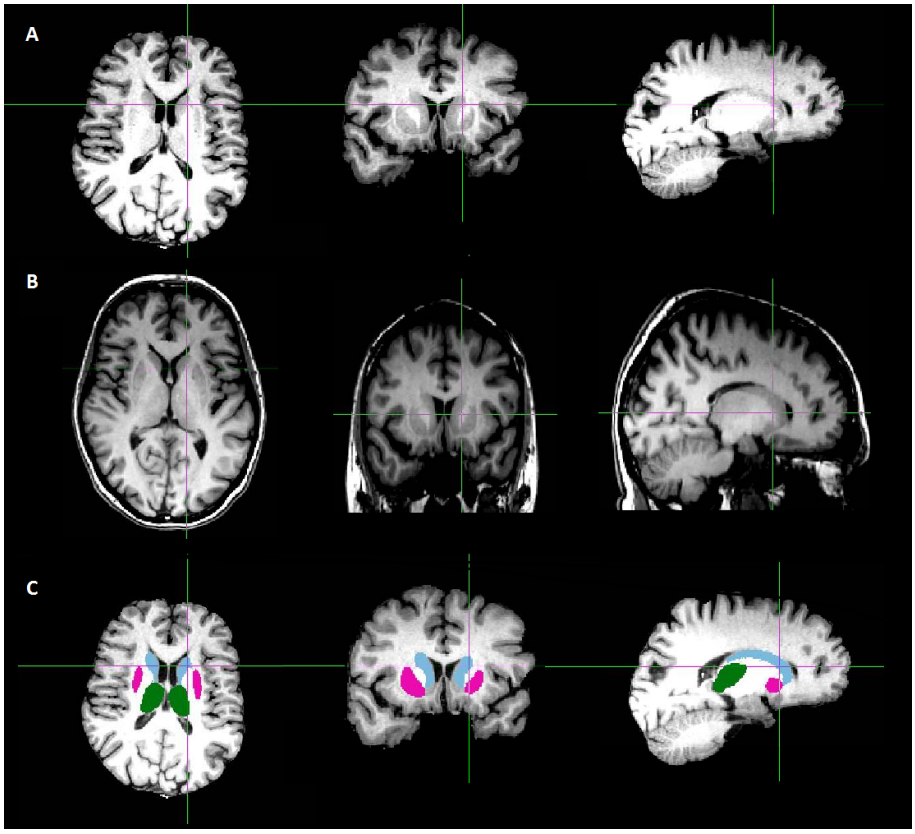

Figure 5.14: **A** - MRI image with a contrast enhancement for better distinction of BG structures; **B** - T1-MRI image after two-stage affine registration to the MNI space; **C** - Fusion of the MRI enhancement images with the caudate nucleus (light blue), thalamus (green) and putamen (pink) masks estimated with FIRST from Patient 1.

As depicted in figure 5.14 (B) and 5.15 (B), the linearly registration of the T1-MRI to the MNI space result in a set of images in which the structures are much larger than the individual space,

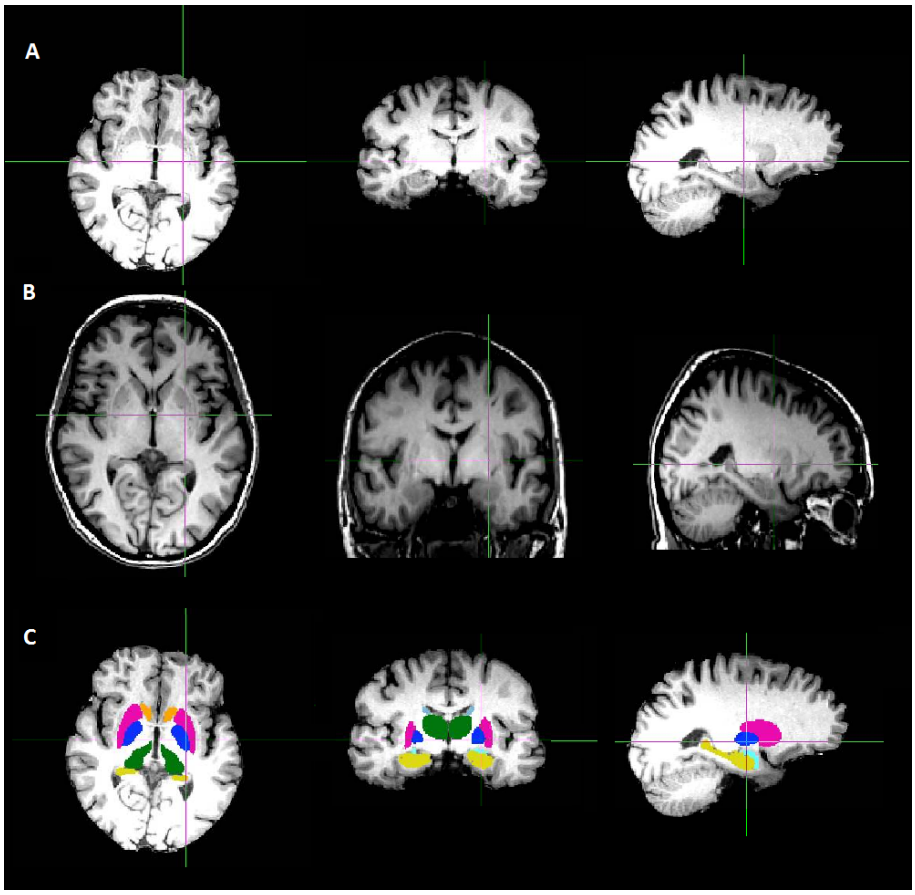

Figure 5.15: **A** - MRI image with a contrast enhancement for better distinction of basal ganglia structures; **B** - T1-MRI image after two-stage affine registration to the MNI space; **C** - Fusion of the MRI enhancement images with the caudate nucleus (light blue), thalamus (green), putamen (pink), pallidum (blue), hippocampus (yellow), nucleus accubens (orange) and amygdala (fluorescent light blue) masks estimated with FIRST from Patient 1.

possibly due to the inherent smoothness of the 152 T1-MRI images of the template (figure 5.16 (A)). Considering that this registration procedure was the same performed in the training dataset for FIRST development, the variation information on shape and intensity estimated across all the training dataset to establish the probabilistic relationships in a 3D model, may have been biased to overestimate the structures masks.

Therefore, the smoothness of the template which leads to larger structures in the MNI space may have affected the variation estimations for each vertex of each structure across the training set, limiting the 3D models vertex combinations to larger masks.

From all the structures the thalamus in the warped T1 images is the one which the MNI smoothness induce a largest area. This is in accordance with the FIRST results in figures 5.14 (C) and 5.15 (C), since the resulted thalamus masks were much larger than the corresponding structures in the individual space.

An example of BG structures masks in the MNI-152 space is shown in the figure 5.16.

On the average, the manual segmentation of DBs, such as the ones segmented by FIRST, takes

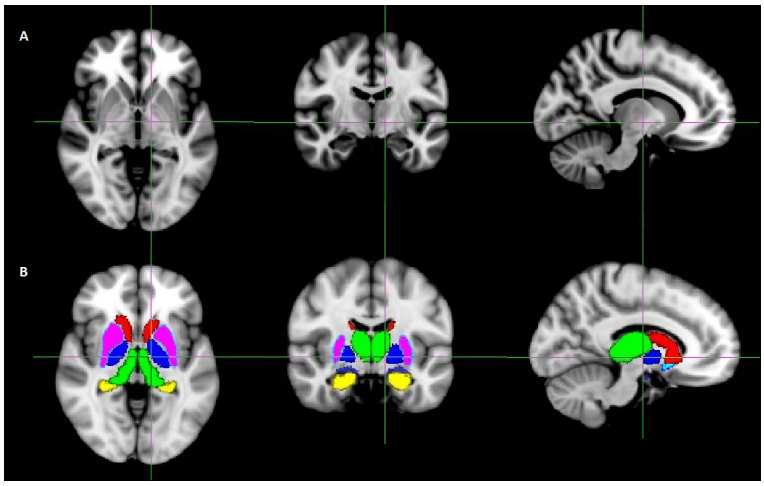

Figure 5.16: **A** - MNI-152 T1 1-mm brain images. **B** - Fusion of the MNI152 images with the caudate nucleus (red), thalamus (green), putamen (pink), pallidum (blue), hippocampus (yellow), nucleus accubens (light blue) and amygdala (purple) masks estimated with FIRST, from Patient 6, and transformed to the MNI space.

5.26 minutes per structure by an expert.[6] Using FIRST, the execution time of the registration and segmentation step for each of the 14 structures (7 bilateral structures) was around 1.20 minutes. In the literature, the execution time of automatic segmentation methods varies considerably, and is highly dependent on the registration method. Using non-linear registrations the execution time varies between 30 minutes to 3 hours.[6] In contrary, using linear registration the execution time only requires 1 minute and the segmentation 40 seconds.[6, 60] Therefore, using FIRST the execution time is even lower by a seconds than recent linear methods of segmentation and despite the overestimated masks, the results were very congruent.

Clinical outcome associated with electrodes positioning in relation to BG structures

In order to establish a relation between patient's outcome and the structures stimulation by the electrodes, the centroid of the mask for each structure were estimated in the individual space and compared with the position of the electrodes. Section A.7 , in the annex, present all the distances between each electrode to each structure for each DBS patient. Since the target structure of DBS for Parkinson's patients was the STN and the segmentation of this nucleus is not available using FIRST, a manual mask was performed by Dr. Verena Rozanski and compared to the patients' outcome.

In relation to Dystonia patients, the distance between the electrode, which lead to a better patient's outcome, and the centroid of the target structure, pallidum, was on average 5,15$\pm$1,88mm. Nonetheless, as suggested by the high value of standard deviation, establishing a relation between this distance and a better patient's outcome is not clinically viable. The distances to the center of the pallidum which provide a good outcome ranged from 1.43 to 8.03mm. Therefore the DBS procedure for dystonia is not highly dependent on this distance but instead of the arrangement

of the fibers of the brain, which establish the interconnections of the basal ganglia, allowing to control the hyperfunction of the GPi [38].

For Parkinson, the distance between the electrodes which lead to a better patient's outcome and the centroid of the target structure was on average 6,47±1,31mm . However, there were at least three cases in which distances greater than 6,47 in the right side produced better outcomes than the electrodes placed at the estimated average distance. Thus, we can not assume that the distances around 6,47 are the optimum distances to the center of the structure, although on average may be the best. Considering that all the brains are different as well as the disposition of the fibers, the relation between this distance and the outcome may be inappropriate. Although, it was interesting to observe than none of the deepest electrodes closer to the center of the target structure, STN, were chosen since they produce the worst outcomes. Possibly at this closeness, the electric field produced by the electrodes were stimulating also the substancia nigra, a structure near the STN which when stimulated can induce hypomania [67, 68].

Regarding the other segmented structures by comparing the tables in section A.7, each electrode is well distanced from the amygdala, hippocampus, thalamus, nucleus accubens and caudate nucleus, so it is not possible to establish a correlation between the patient's outcome and the proximity of the electrode to each structure. Nevertheless, the segmentation of these structures are important to the work of Munich University in which this thesis is included, since in association of DTI information may improve our knowledge of BG interconnections.

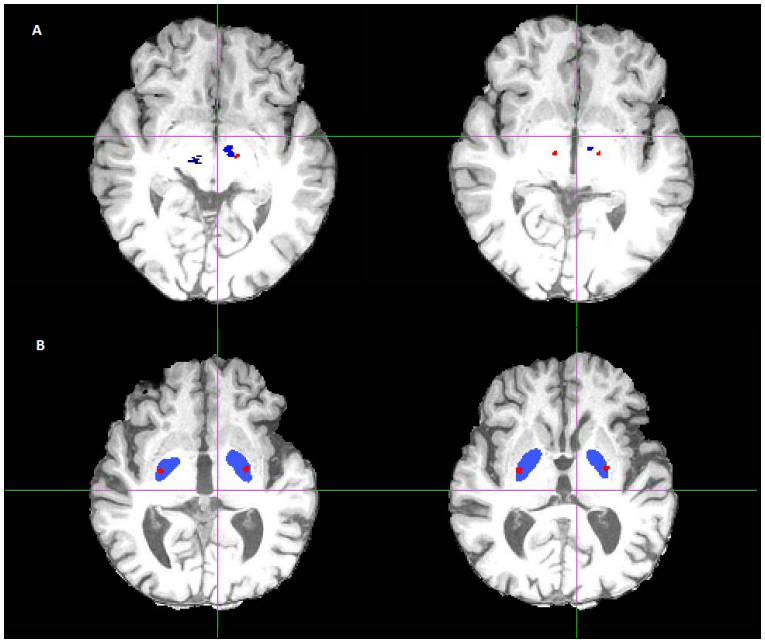

Figure 5.17: **A** - Electrodes mask overlaid with STN manual mask and T1 scan from patient 1 with Parkinson: (left) Worst patient's outcome by activating the deepest electrode on the left side; (right) Better patient's outcome by activating the 3^{rd} electrode on the left side. **B** - Electrodes mask overlaid with pallidum mask and T1 scan from patient 9 with Dystonia: (left) Worst patient's outcome by activating the deepest electrodes on both sides; (Right) Better patient's outcome by activating the 3^{rd} electrodes on both sides.

Chapter 6

Conclusions and Future Work

In this chapter is presented a review of the objectives and the work developed to meet these goals. Some suggestions for future work can also be found.

6.1 Review of Thesis Objectives

In this study, it was intended to develop a multimodal method for the detection of subdural and deep brain electrodes as well as deep brain structures to assist in the pre-neurosurgical evaluation of patients with Epilepsy and patients undergoing DBS.

The proposed assistance for the pre-neurosurgical evaluation of DBS patients was intended to support in the delineation of STN and GPi prior the DBS lead implantation and after the surgery to correlate the electrodes position with the proximity to these structures and others in the deep brain area. This guidance may improve the accuracy of the surgery and consequently the patient's outcome and quality of life.

For the Epilepsy, it was intended to establish a 3D model with the subdural electrodes over the cortex. A 3D visualization prior the resection surgery is useful to relate the iEEG data with the brain anatomical position of the electrodes and therefore delineate with higher precision the epileptic focus and the eloquent areas. As for DBS, this approach may lead to a more accurate identification of the potentially epileptogenic tissue and consequently improve the patient's outcome and quality of life.

6.2 Meeting Objectives: The contributions of the thesis

To meet the proposed goals a pre-processing pipeline was developed for multimodal co-registration and brain extraction, for the two diseases. Considering that the parameters chosen have resulted in fine alignments and an accurate brain extraction, the pipeline is recommended in future studies.

The processing for electrodes segmentation was different for Epilepsy and DBS cases. For the detection of the subdural electrodes in epileptic patients, a threshold in FSL was used to extract only the electrodes data. No beam hardening, artefacts or skull were identified after the intensity threshold was applied. Therefore, the electrodes mask were fused with the skull-stripping T1-MRI, without cerebellum, in a 3D representation using volume rendering in the MRIcron. The resulting T1 without the cerebellum is being useful to the physicians for the improvement of the visualization of the strips and grids in the 3D visualization. This approach was already tested by HSJ for one patient, which has been seizure free since surgery. More requests has been made by HSJ for future patients.

For the DBS cases, an interface in MATLAB was developed with several options such as the method used to segment the DBS lead, the dataset to be read and the adjustment of some parameters for a better performance. Prior the segmentation of the DBS electrodes, it is necessary to deduce a DBS mask and based on their BT stipulate the position of each electrode. A semiautomatic and an automatic methods were developed to obtain the DBS lead and then the BT coordinates. The electrodes positions estimated either using the automatic or semiautomatic method were compared by the ones given by Dr. Verena Rozanski. The differences found were less than a voxel size, so this interface can be useful in future DBS studies to produce automatically the electrodes masks.

In addition, the creation of the electrodes mask using our tool lasts around 1 minute, which when compared with the normal procedure by the physicians, which lasts around 40 min, is much faster. Normally, the physician need to determine manually the BT and some angles in relation to the DBS trajectory. Thus, the electrodes positions are estimated using for instance Excel, to do the trigonometric relations. The obtained coordinates for the electrodes are then used to create ROIs. This entire procedure is very time consuming when compared with the segmentation time of out tool.

An automatic segmentation procedure, available among FSL tools, was used for the segmentation of brain structures. This tool was the same used to segment the cerebellum in the epileptic patients. The masks resulted by these procedure are very congruent in shape and position to the ones in the individual space. Even when some structures were almost imperceptible in the individual space, such pallidum, the target area of DBS surgery for Dystonia, the procedure was capable to segment them correctly. However, the resulting masks, in general, were overestimated probably because they were biased by the MNI space smoothness. Unfortunately, the automatic segmentation procedure does not have the capacity to segment the STN, so manual masks were estimated by Dr. Verena Rozanski for the correlation with the electrodes position, specially for Parkinson cases.

Considering that there are several problems involved with manual segmentation of brain structures, automatic segmentation methods are most viable. The first issue of the manual segmentation is the time cost associated. For instance, manual brain/non-brain segmentation can lasts between 15 minutes to 2 hours for one patient [63]. In addition, it requires a expert with sufficient background of the shape and intensities of the brain structures to segment. Even in this cases,

subjectivity is always present.

Although the automatic method used in this work overestimates the area of some structures, it can be a good alternative to manual segmentation due to its fastest performance and a very congruent shape and position masks. Since the automatic method is based on a linear registration, the results were expected to be not so precise than the methods based on non-linear registration. However, by comparing the obtained structures with the ones by the non-linear methods, (figure 3.1), the differences are not significant.

The patient's outcome relation to the distance of each electrode to the target areas may be clinical infeasible due to the high values of standard deviation. Thereby, we conclude that outcomes are not only dependent in the distances to the structures, but it also depends of fibers arrangement of each individual patient.

Therefore, answering the questions raised in the introduction, a method for the detection of intra-craned electrodes was developed with success either for Epilepsy and Parkinson and an automatic segmentation method, available in FSL, was applied for the segmentation of some basal ganglia structures and others of the deep brain area. The discussion of the results obtained with this tool, allows to evaluate its performance and improve our knowledge about this automatic method and therefore estimate their potential in future applications.

6.3 Future Work

Further testing are necessary to validate with higher accuracy the pipeline developed for Epilepsy scenario. An interface in which the physician can run online automatically the pipeline might also be useful in the future. The interface should have several options such as listed below:

- exchange of the sign of the intensities, if necessary;
- adjustment of the fractional intensity threshold for brain extraction;
- visual verification of the extracted brain;
- visual inspection of the CT-MRI co-registration;
- adjustment of the intensity threshold for electrodes segmentation;
- selection of the ROI area to extract the bottom borders of cerebellum, if necessary.

If a post-operative T2-MRI image is available, the interface may also have an option, for the physician, to select directly on the image the center of each electrode and, based on the dimensions of the electrodes given by the datasheet, generate an electrodes mask. A intensity threshold for T2 scans to segment the electrodes can be less precise than this method since the electrodes placed over the cortex in the T2 scans show less contrast in relation to the medium between cortex and skull.

In addition, considering that a loss of resolution was seen in the 3D volume rendering, others software can be explored or even developed to substitute MRIcron in this task. However, since the volume rendering depends highly of the parameters for the weighting functions, which, in

automatic software's algorithms such MRIcron is a setback because they cannot be adjust, the software chosen or developed must have the possibility to adjust these parameters.

In relation to the DBS results, it would be interesting to compare the obtained masks segmented by the automatic procedures with manual masks marked by at least three experts. In order to find volumetric differences between manual and automatic masks, dice similarity coefficient would be recommended [6, 62]. For the structures in which the dice correlation result was lower, a MATLAB machine learning algorithm could be developed as well as for STN, since for this structure the automatic segmentation in FSL is not possible.

Furthermore, the development of a template with only Parkinson and Dystonia MRI data could lead to more precise structures segmentation or even using the French atlas, which covers with more detail deep brain regions and the contrast between grey and white matter is significant [43].

Regarding the DBS electrodes position, considering that electrodes induce a electric field in the neighbour tissues, it would be interesting correlate it with the neighbour structures and fibers. This is a currently emerging area to better understand the BG interconnections and patients' outcome.

The automatic procedure adopted in this work for structure segmentation has enough potential to study pathologies and improve the pre-neurosurgical evaluation. In addition to the segmentation, this tool allows to compare shape and volumetric differences among groups. So it would be interesting to use it to compare shape and volumetric differences between normal subjects and individuals with pathologies, not necessarily for Parkinson, Dystonia or Epilepsy.

The segmentation of some of the structures in this work, such nucleus accubens, hippocampus and amydgada can be also useful in the future for the target delineation prior to surgery in patients with resistant depression, schizophrenia and mood disorders, respectively [69, 70, 71].

Appendix A

Annex

A.1 Basal Ganglia Interconnections

The following images were taken from the reference [1].

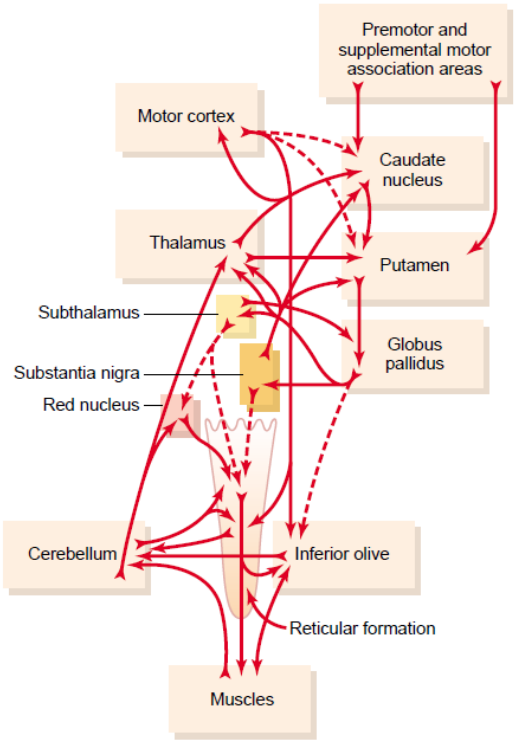

Figure A.1: Relation of BG neuronal circuit with the corticospinalcerebellar system, for movement control.

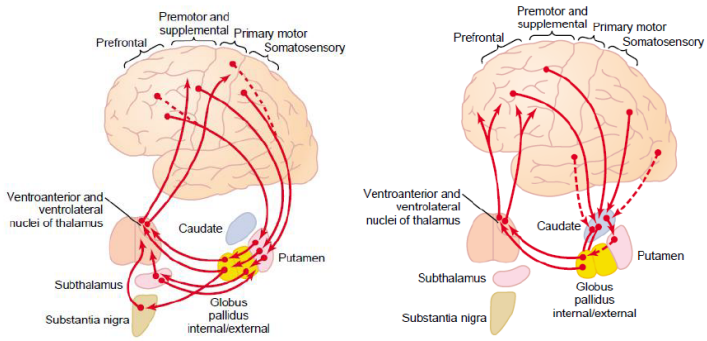

Figure A.2: Putamen and caudate circuit through the BG.

A.2 Epilepsy dataset

A brief diagnosis and treatment plan provided by Dr. Ricardo Rego, for each patient.

Patient 1

"26 year-old right-handed male with focal refractory epilepsy starting at age 24. Etiology was a low-grade tumor, located at the left inferior temporal gyrus; the center of this lesion was 6 cm posterior to the temporal pole. During video-EEG monitoring multiple dialeptic or automotor seizures were recorded, with lateralizing signs to the dominant hemisphere. Ictal patterns were consistently left temporal, with a maximum at the middle temporal region. In order to better delineate the seizure onset zone and its relation with neighboring language areas, we implanted a 4x8 subdural electrode grid over the left temporal convexity (superior, middle and inferior temporal gyrus) and 2 subtemporal strips, each with 8 contacts: strip 1 was on the basal surface of the inferior temporal gyrus, below the tumour; strip 2 was directed antero-medially, close to the amygdala and hippocampus. The invasively recorded seizures originated on the inferior surface of the tumour (strip 1) with rapid propagation to postero-inferior grid electrodes, behind the lesion. Cortical mapping by electrical stimulation disclosed language functions over the superior and middle temporal gyrus. Reading was interrupted upon stimulation of the 2 lateral contacts of strip 1. An extended lesionectomy was performed, including the visible tumor and adjacent inferior and posterior cortex. Post-operatively he had transient alexia, which resolved entirely after a few days. He has been seizure -free for 7 months. The pathological specimen showed features indicative of a ganglioglioma."

Patient 2

"24 year-old right-handed male with focal epilepsy starting at age 15. Shortly after seizures began, investigation with MRI disclosed a left temporal pole tumor, which was ressected at another institution. The pathological diagnosis was ganglioglioma. Seizures persisted throughout subsequent years and were refractory to multiple AED. Follow-up imaging excluded tumor recurrence and showed a clastic region on the temporal pole, with a posterior gliotic margin, as well as atrophy and gliosis of the amygdala/ anterior hippocampal region. He was referred to perform pre-

surgical epilepsy investigation. During video-EEG monitoring several automotor seizures were recorded, with lateralizing signs to the dominant hemisphere and seizure patterns over the left fronto-temporal region, with very rapid contralateral propagation. For the invasive recordings, we implanted a 4x8 subdural electrode grid over the left anterior temporal convexity (superior, middle and inferior temporal gyrus) and 2 subtemporal strips: strip 1 had 8 contacts and aimed the hippocampal region (although final placement showed displacement towards the lateral pole); strip 2 had 4 contacts at the basal surface of the inferior temporal gyrus. Interictal spiking was very prominent on both strips, specially strip 1. Cortical mapping by electrical stimulation showed language functions on several postero-superior contacts of the grid. No seizures were recorded after 11 days, at which time invasive monitoring was interrupted and surgery anticipated due to meningitis. The surgical procedure consisted of a temporal pole resection behind the gliotic margin (sparing language areas defined by electrical stimulation) and amygdalo-hippocampectomy. The patient has been seizure-free for 5 months."

Patient 3

"32 year-old left-handed female with refractory epilepsy starting at age 8. Etiology was probably perinatal ischemia, as suggested by clinical history and an MRI showing bilateral atrophy of the parietal cortices. Seizures consisted of a somatossensory and complex visual aura (she reported seeing "funny colors" as well as a "tingling" sensation on the left side of the body), followed by loss of consciousness and predominantly right-sided automatisms. The patient was referred for presurgical evaluation. During video-EEG we recorded several of the habitual seizures, which had a right temporo-parieto-occipital EEG onset. For the invasive study, an 8x6 subdural electrodes grid was implanted on the temporo-parieto-occipital junction (the more anterior electrodes also reached the rolandic cortex), as well as a 2x4 grid on the basal surface of the inferior temporal gyrus and an 8-contact strip aiming the hippocampal region. Seizure onsets and predominant interictal epileptiform discharges were located on the parietal opercular region, also extending postero-inferiorly to the temporo-occipital cortex; electrical stimulation of some electrodes on this region evoked the patient's habitual auras. Surgery consisted of a corticectomy delineated according to these results. The patienty has been seizure-free since surgery (performed only one month ago, precluding a more reliable evaluation of the procedure's success)."

A.3 Epilepsy methods - Workflow

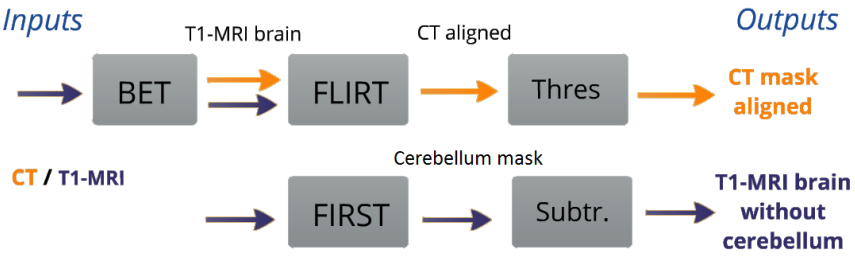

Figure A.3: Workflow applied for the segmentation of the subdural electrodes and for the extraction of the structural image without skull and cerebellum, using FSL.

A.4 Validation of Epilepsy results

SÃO JOÃO

Serviço de Neurologia | Unidade de Neurofisiologia

Porto, June 21st 2013

It is estimated that one third of patients with epilepsy are refractory to anti-epileptic drugs. Ongoing seizures have highly deleterious effects on individual health and quality of life. A substantial proportion of these patients are candidates for epilepsy surgery, which can dramatically improve seizure control and even render some patients completely seizure-free.

Presurgical investigation of refractory epilepsies is a challenging and complex field, requiring expertise and a multidisciplinary approach. At our institution, the epilepsy surgery group includes experts in six medical subfields, who collaborate in order to appropriately investigate and select patients for epilepsy surgery. A subset of these patients needs to be investigated invasively, i.e., implanting subdural or intracerebral electrodes in order do precisely define the cortical areas that need to be removed (and the ones that need to be spared!).

When using subdural electrodes, one of the main challenges is to obtain reliable 3-D images of the cortical surface and its relation with the implanted electrodes, in order to correctly visualize and plan the resection. However, this cannot be achieved with standard imaging resources. We were therefore delighted to benefit from the cooperation of Eng. Nádia Moreira, under the guidance of Prof. João Paulo Cunha, from FEUP, who actively and effectively engaged in finding a solution for this limitation. They delivered post-processed images clearly displaying the 3-dimensional relation of the subdural electrodes with the cortical surface. So far, three of our recent epilepsy surgery patients already benefited from this cooperation. We do hope this collaboration continues and extends into other fields of clinical/bioengineering overlap.

On behalf of the epilepsy surgery team at Hospital de São João,

Ricardo Rego
(Neurologist, coordinator of the Epilepsy Monitoring Unit)

CENTRO HOSPITALAR DE SÃO JOÃO, E.P.E.
Alameda Professor Hernâni Monteiro 4202-451 Porto
T +351 225 512 199 | F +351 225 025 766 | E geral@hsjoao.min-saude.pt | W www.hsjoao.min-saude.pt

A.5 DBS methods - Workflow

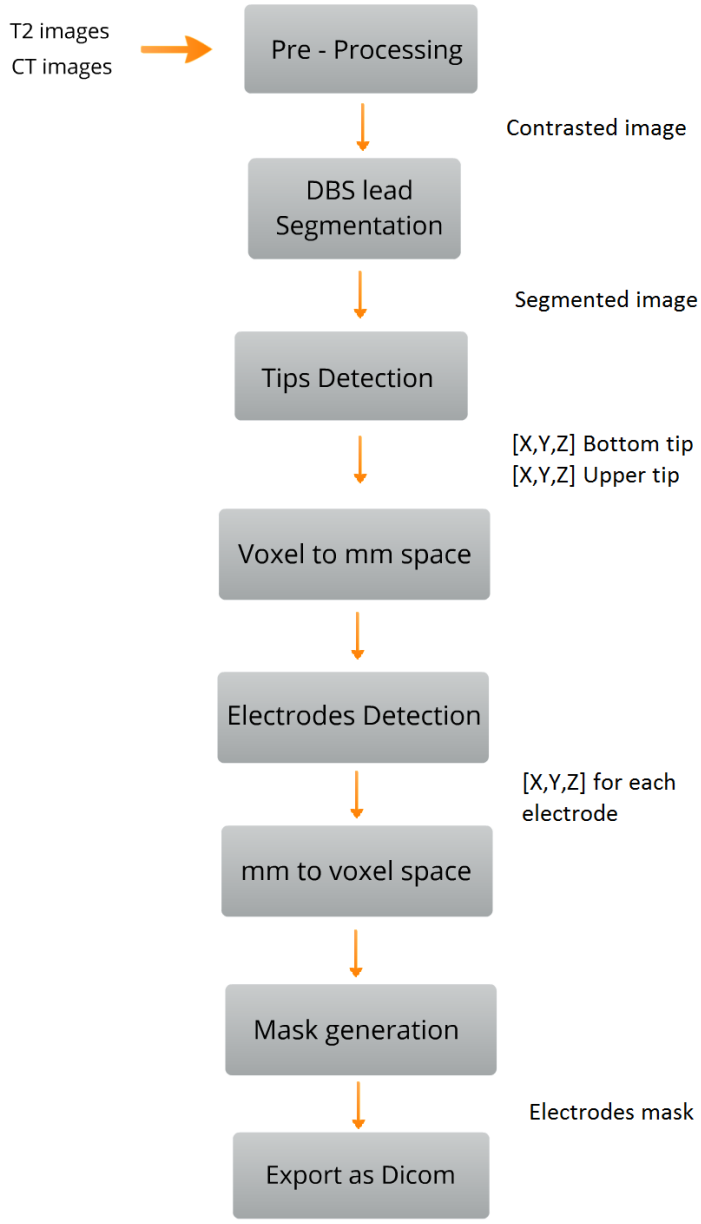

Figure A.4: Workflow applied for the segmentation of the DBS electrodes in MATLAB.

Figure A.5: Workflow applied for the segmentation of DBs and the estimation of their centroid, using FSL.

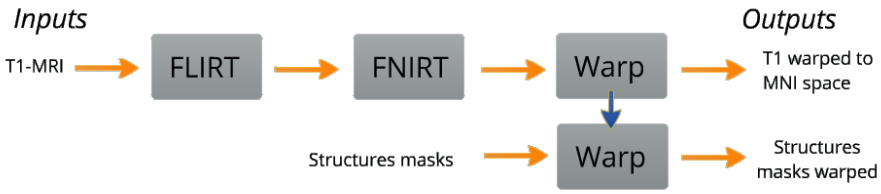

Figure A.6: Workflow applied to warp the structural images and the corresponding structures masks to the MNI space, using FSL.

A.6 Electrodes Positions

In this section is presented all the normalized distances in relation to the BT obtained with MATLAB and by Dr. Verena Rozanski for each electrode, E1, E2, E3 and E4.

A.6.1 Parkinson

- Patient 1;

Left Side

Normalized distances for patient 1 in the left side.

	Matlab					Verena				
	BT	|BT-E1|	|BT-E2|	|BT-E3|	|BT-E4|	BT	|BT-E1|	|BT-E2|	|BT-E3|	|BT-E4|
x	-10,78	0,94	1,88	2,81	3,75	-11,72	0,95	1,80	2,64	3,49
y	25,85	0,94	1,88	2,81	3,75	25,85	1,06	2,00	2,93	3,87
z	11,61	2,00	4,00	5,00	7,00	12,61	2,04	3,85	5,66	7,48

Right Side

Normalized distances for patient 1 in the right side.

	Matlab					Verena				
	BT	|BT-E1|	|BT-E2|	|BT-E3|	|BT-E4|	BT	|BT-E1|	|BT-E2|	|BT-E3|	|BT-E4|
x	9,84	0,94	1,88	2,82	3,75	8,91	0,95	1,80	2,64	3,49
y	26,79	0,94	1,87	2,81	3,75	23,73	1,45	2,73	4,02	5,30
z	12,61	2,00	4,00	5,00	7,00	13,61	2,04	3,85	5,66	7,48

- Patient 6;

Left Side

Normalized distances for patient 6 in the left side.

	Matlab					Verena				
	BT	|BT-E1|	|BT-E2|	|BT-E3|	|BT-E4|	BT	|BT-E1|	|BT-E2|	|BT-E3|	|BT-E4|
x	18,57	0,00	0,94	0,94	0,94	18,57	0,20	0,37	0,54	0,72
y	56,67	0,94	0,94	1,88	2,81	56,42	1,29	2,44	3,58	4,73
z	-11,20	2,00	3,00	5,00	6,00	-12,20	2,24	4,23	6,23	8,22

Right Side

Normalized distances for patient 6 in the right side.

	Matlab					Verena				
	BT	|BT-E1|	|BT-E2|	|BT-E3|	|BT-E4|	BT	|BT-E1|	|BT-E2|	|BT-E3|	|BT-E4|
x	40,13	0,00	0,94	1,88	2,81	38,26	0,95	1,80	2,64	3,49
y	50,11	0,94	1,87	1,87	2,81	49,86	0,95	1,80	2,64	3,49
z	-14,20	2,00	3,00	4,00	6,00	-13,20	2,04	3,85	5,66	7,48

- Patient 7;

Left Side

Normalized distances for patient 7 in the left side.

	Matlab					Verena				
	BT	|BT-E1|	|BT-E2|	|BT-E3|	|BT-E4|	BT	|BT-E1|	|BT-E2|	|BT-E3|	|BT-E4|
x	5,92	0,00	0,00	0,93	0,93	8,74	0,77	1,45	2,14	2,82
y	85,04	1,88	2,81	3,75	5,63	86,30	1,29	2,44	3,58	4,73
z	12,48	2,00	3,00	5,00	7,00	11,48	2,11	3,99	5,87	7,75

Right Side

Normalized distances for patient 7 in the right side.

	Matlab					Verena				
	BT	|BT-E1|	|BT-E2|	|BT-E3|	|BT-E4|	BT	|BT-E1|	|BT-E2|	|BT-E3|	|BT-E4|
x	28,42	0,94	0,94	1,88	2,82	29,87	0,77	1,45	2,14	2,82
y	85,98	1,87	2,81	3,75	4,69	88,79	0,95	1,80	2,64	3,49
z	8,48	2,00	3,00	5,00	6,00	8,48	2,11	3,99	5,87	7,75

- Patient 11;

Left Side

Normalized distances for patient 11 in the left side.

	Matlab					Verena				
	BT	|BT-E1|	|BT-E2|	|BT-E3|	|BT-E4|	BT	|BT-E1|	|BT-E2|	|BT-E3|	|BT-E4|
x	-11,72	0,94	0,94	0,94	1,87	-12,45	0,51	0,96	1,41	1,86
y	24,16	0,94	1,87	1,87	2,81	28,98	0,95	1,80	2,64	3,49
z	-39,83	2,00	3,00	5,00	6,00	-39,83	2,19	4,14	6,09	8,04

Right Side

Normalized distances for patient 11 in the right side.

	Matlab					Verena				
	BT	|BT-E1|	|BT-E2|	|BT-E3|	|BT-E4|	BT	|BT-E1|	|BT-E2|	|BT-E3|	|BT-E4|
x	9,48	0,00	0,00	0,94	0,94	10,78	0,43	0,81	1,19	1,57
y	27,91	0,00	0,94	1,87	1,87	33,12	0,95	1,80	2,64	3,49
z	-43,83	2,00	3,00	5,00	6,00	-41,83	2,21	4,17	6,14	8,10

- Patient 15;

Left Side

Normalized distances for patient 15 in the left side.

	Matlab					Verena				
	BT	|BT-E1|	|BT-E2|	|BT-E3|	|BT-E4|	BT	|BT-E1|	|BT-E2|	|BT-E3|	|BT-E4|
x	4,50	0,93	0,98	1,87	1,87	4,50	0,47	0,88	1,30	1,72
y	73,72	1,87	4,68	4,68	5,62	73,72	1,59	3,01	4,42	5,83
z	19,93	2,00	3,00	5,00	6,00	21,93	2,20	4,16	6,11	8,07

Right Side

Normalized distances for patient 15 in the right side.

	Matlab					Verena				
	BT	|BT-E1|	|BT-E2|	|BT-E3|	|BT-E4|	BT	|BT-E1|	|BT-E2|	|BT-E3|	|BT-E4|
x	26,07	0,93	0,93	0,93	1,87	27,00	0,84	1,59	2,34	3,09
y	70,90	0,94	2,82	3,75	4,69	72,78	1,29	2,44	3,58	4,73
z	19,93	2,00	3,00	5,00	6,00	21,93	2,09	3,94	5,79	7,65

- Patient 16;

Left Side

Normalized distances for patient 16 in the left side.

	Matlab					Verena				
	BT	|BT-E1|	|BT-E2|	|BT-E3|	|BT-E4|	BT	|BT-E1|	|BT-E2|	|BT-E3|	|BT-E4|
x	-7,97	0,94	0,94	0,94	0,94	-7,97	0,39	0,74	1,09	1,43
y	27,43	0,94	1,87	2,81	3,75	28,37	1,06	2,00	2,93	3,87
z	-20,39	3,00	4,00	6,00	8,00	-19,39	2,22	4,19	6,16	8,12

Right Side

Normalized distances for patient 16 in the right side.

	Matlab					Verena				
	BT	|BT-E1|	|BT-E2|	|BT-E3|	|BT-E4|	BT	|BT-E1|	|BT-E2|	|BT-E3|	|BT-E4|
x	16,41	1,87	1,87	2,81	3,75	17,34	0,70	1,31	1,93	2,55
y	25,55	0,94	1,88	2,82	3,75	25,55	0,95	1,80	2,64	3,49
z	-19,39	2,00	4,00	5,00	7,00	-18,39	2,14	4,04	5,94	7,85

- Patient 17;

Left Side

Normalized distances for patient 17 in the left side.

	Matlab					Verena				
	BT	|BT-E1|	|BT-E2|	|BT-E3|	|BT-E4|	BT	|BT-E1|	|BT-E2|	|BT-E3|	|BT-E4|
x	-14,53	0,94	1,88	2,81	3,75	-14,53	0,70	1,31	1,93	2,55
y	32,96	0,00	0,94	0,94	1,88	32,96	0,47	0,88	1,30	1,72
z	-12,17	2,00	4,00	6,00	8,00	-11,17	2,14	4,04	5,94	7,85

Right Side

Normalized distances for patient 17 in the right side.

	Matlab					Verena				
	BT	|BT-E1|	|BT-E2|	|BT-E3|	|BT-E4|	BT	|BT-E1|	|BT-E2|	|BT-E3|	|BT-E4|
x	7,97	0,00	0,94	0,94	1,87	8,91	0,47	0,88	1,30	1,72
y	31,09	0,00	0,00	0,93	0,93	31,09	0,70	1,31	1,93	2,55
z	-11,17	2,00	4,00	6,00	8,00	-10,17	2,20	4,16	6,11	8,07

- Patient 19;

Left Side

Normalized distances for patient 19 in the left side.

	Matlab					Verena				
	BT	|BT-E1|	|BT-E2|	|BT-E3|	|BT-E4|	BT	|BT-E1|	|BT-E2|	|BT-E3|	|BT-E4|
x	-4,72	0,94	1,88	1,88	1,88	-4,72	0,39	0,74	1,09	1,43
y	31,31	0,94	1,88	1,88	2,82	34,13	0,58	1,10	1,62	2,14
z	52,43	2,00	4,00	6,00	8,00	55,43	2,22	4,19	6,16	8,12

Right Side

Normalized distances for patient 19 in the right side.

	Matlab					Verena				
	BT	|BT-E1|	|BT-E2|	|BT-E3|	|BT-E4|	BT	|BT-E1|	|BT-E2|	|BT-E3|	|BT-E4|
x	19,65	0,94	1,88	2,82	3,75	20,59	0,95	1,80	2,64	3,49
y	32,25	0,94	0,94	1,88	2,81	33,19	0,95	1,80	2,64	3,49
z	52,43	2,00	3,00	5,00	7,00	55,43	2,04	3,85	5,66	7,48

A.6.2 Dystonia

- Patient 2;

Left Side

Normalized distances for patient 2 in the left side.

	Matlab					Verena				
	BT	|BT-E1|	|BT-E2|	|BT-E3|	|BT-E4|	BT	|BT-E1|	|BT-E2|	|BT-E3|	|BT-E4|
x	-16,84	0,94	0,94	1,87	1,87	-13,90	0,95	1,80	2,64	3,49
y	45,74	0,94	1,88	1,88	2,82	45,74	0,77	1,45	2,14	2,82
z	12,85	2,00	4,00	6,00	8,00	12,85	2,04	3,85	5,66	7,48

Right Side

Normalized distances for patient 2 in the right side.

	Matlab					Verena				
	BT	|BT-E1|	|BT-E2|	|BT-E3|	|BT-E4|	BT	|BT-E1|	|BT-E2|	|BT-E3|	|BT-E4|
x	21,60	0,00	0,94	1,87	2,81	20,54	0,58	1,10	1,62	2,14
y	41,06	0,93	1,87	1,87	2,81	41,06	0,95	1,80	2,64	3,49
z	14,85	2,00	4,00	6,00	8,00	17,85	2,17	4,11	6,04	7,37

- Patient 3;

Left Side

Normalized distances for patient 3 in the left side.

	Matlab					Verena				
	BT	|BT-E1|	|BT-E2|	|BT-E3|	|BT-E4|	BT	|BT-E1|	|BT-E2|	|BT-E3|	|BT-E4|
x	-15,47	0,00	0,94	0,94	1,87	-16,41	0,27	0,52	0,76	1,01
y	44,10	0,00	0,00	0,94	0,00	44,10	0,52	0,76	1,01	0,00
z	18,85	2,00	4,00	6,00	8,00	-20,85	2,23	4,22	6,20	8,19

Right Side

Normalized distances for patient 3 in the right side.

	Matlab					Verena				
	BT	|BT-E1|	|BT-E2|	|BT-E3|	|BT-E4|	BT	|BT-E1|	|BT-E2|	|BT-E3|	|BT-E4|
x	28,59	0,00	0,00	0,94	0,94	27,66	0,39	0,74	1,09	1,43
y	39,41	0,00	0,00	0,00	0,00	37,53	0,35	0,66	0,98	1,29
z	17,85	2,00	4,00	6,00	8,00	18,85	2,22	4,19	6,16	8,12

- Patient 4;

Left Side

Normalized distances for patient 4 in the left side.

	Matlab					Verena				
	BT	|BT-E1|	|BT-E2|	|BT-E3|	|BT-E4|	BT	|BT-E1|	|BT-E2|	|BT-E3|	|BT-E4|
x	-18,58	0,94	0,00	0,00	0,00	-17,64	0,39	0,74	1,09	1,43
y	41,51	0,94	1,88	2,82	3,75	43,39	1,13	2,13	3,13	4,13
z	12,78	2,00	4,00	6,00	7,00	14,78	2,22	4,19	6,16	8,12

Right Side

Normalized distances for patient 4 in the right side.

	Matlab					Verena				
	BT	|BT-E1|	|BT-E2|	|BT-E3|	|BT-E4|	BT	|BT-E1|	|BT-E2|	|BT-E3|	|BT-E4|
x	24,55	0,00	0,00	0,00	0,00	23,68	0,58	1,10	1,62	2,14
y	51,83	0,93	1,87	1,87	2,81	53,70	0,95	1,80	2,64	3,49
z	13,78	2,00	4,00	6,00	8,00	15,78	2,17	4,11	6,04	7,97

- Patient 5;

Left Side

Normalized distances for patient 5 in the left side.

	Matlab					Verena				
	BT	|BT-E1|	|BT-E2|	|BT-E3|	|BT-E4|	BT	|BT-E1|	|BT-E2|	|BT-E3|	|BT-E4|
x	-11,81	0,94	0,94	1,87	2,81	-11,81	0,77	1,45	2,14	2,82
y	38,27	0,00	0,93	1,87	2,81	38,27	1,13	2,13	3,13	4,13
z	23,04	2,00	4,00	5,00	7,00	23,04	1,95	3,68	5,41	7,14

Right Side

Normalized distances for patient 5 in the right side.

	Matlab					Verena				
	BT	|BT-E1|	|BT-E2|	|BT-E3|	|BT-E4|	BT	|BT-E1|	|BT-E2|	|BT-E3|	|BT-E4|
x	22,88	0,94	0,94	1,87	1,87	22,88	0,58	1,10	1,62	2,14
y	28,89	0,94	1,88	2,81	3,75	28,89	0,95	1,80	2,64	3,49
z	23,04	2,00	4,00	5,00	7,00	23,04	2,17	4,11	6,04	7,97

- Patient 9;

Left Side

Normalized distances for patient 9 in the left side.

	Matlab					Verena				
	BT	|BT-E1|	|BT-E2|	|BT-E3|	|BT-E4|	BT	|BT-E1|	|BT-E2|	|BT-E3|	|BT-E4|
x	-26,72	0,94	0,94	1,87	1,87	-27,66	0,20	0,37	0,54	0,72
y	30,67	0,00	0,94	0,94	0,94	30,67	0,39	0,74	1,09	1,43
z	-3,22	2,00	4,00	6,00	8,00	-3,22	2,24	4,23	6,23	8,22

Right Side

Normalized distances for patient 9 in the right side.

	Matlab					Verena				
	BT	|BT-E1|	|BT-E2|	|BT-E3|	|BT-E4|	BT	|BT-E1|	|BT-E2|	|BT-E3|	|BT-E4|
x	22,84	0,00	0,00	0,94	0,00	24,84	0,08	0,15	0,22	0,29
y	28,80	0,00	0,00	0,94	0,94	28,80	0,20	0,37	0,54	0,72
z	-3,22	2,00	4,00	6,00	8,00	-3,22	2,25	4,25	6,25	8,24

- Patient 10;

Left Side

Normalized distances for patient 10 in the left side.

	Matlab					Verena				
	BT	|BT-E1|	|BT-E2|	|BT-E3|	|BT-E4|	BT	|BT-E1|	|BT-E2|	|BT-E3|	|BT-E4|
x	-17,34	0,00	0,00	0,94	0,94	-18,34	0,27	0,52	0,76	1,01
y	35,34	0,94	0,94	1,87	1,87	36,28	0,58	1,10	1,62	2,14
z	9,53	2,00	4,00	6,00	8,00	9,53	2,23	4,22	6,20	8,19

Right Side

Normalized distances for patient 10 in the right side.

	Matlab					Verena				
	BT	|BT-E1|	|BT-E2|	|BT-E3|	|BT-E4|	BT	|BT-E1|	|BT-E2|	|BT-E3|	|BT-E4|
x	21,09	0,00	0,94	0,94	0,94	20,58	0,47	0,88	1,30	1,72
y	32,53	0,00	0,93	1,87	2,81	32,53	0,95	0,00	0,08	0,16
z	8,53	2,00	4,00	6,00	7,00	9,53	2,20	4,16	6,11	8,07

- Patient 12;

Left Side

Normalized distances for patient 12 in the left side.

	Matlab					Verena				
	BT	|BT-E1|	|BT-E2|	|BT-E3|	|BT-E4|	BT	|BT-E1|	|BT-E2|	|BT-E3|	|BT-E4|
x	-19,74	0,94	0,94	0,94	1,88	-21,62	0,39	0,74	1,09	1,43
y	41,90	0,00	0,94	0,94	1,88	42,23	0,84	1,59	2,34	3,09
z	14,92	2,00	4,00	6,00	8,00	17,92	2,22	4,19	6,16	8,12

Right Side

Normalized distances for patient 12 in the right side.

	Matlab					Verena				
	BT	|BT-E1|	|BT-E2|	|BT-E3|	|BT-E4|	BT	|BT-E1|	|BT-E2|	|BT-E3|	|BT-E4|
x	25,26	0,00	0,93	0,93	1,87	24,35	0,58	1,10	1,62	2,14
y	36,28	0,93	0,93	1,87	1,87	38,21	0,39	0,74	1,09	1,43
z	14,92	2,00	4,00	6,00	8,00	15,92	2,17	4,11	6,04	7,97

- Patient 14;

Left Side

Normalized distances for patient 14 in the left side.

	Matlab					Verena				
	BT	|BT-E1|	|BT-E2|	|BT-E3|	|BT-E4|	BT	|BT-E1|	|BT-E2|	|BT-E3|	|BT-E4|
x	-11,89	0,00	0,00	0,00	0,94	-14,20	0,20	0,37	0,54	0,72
y	33,96	0,94	0,94	1,87	2,81	31,02	0,84	1,59	2,34	3,09
z	53,19	2,00	4,00	6,00	8,00	54,19	2,24	4,23	6,23	8,22

Right Side

Normalized distances for patient 14 in the right side.

	Matlab					Verena				
	BT	|BT-E1|	|BT-E2|	|BT-E3|	|BT-E4|	BT	|BT-E1|	|BT-E2|	|BT-E3|	|BT-E4|
x	26,54	0,94	0,94	1,88	1,88	24,67	0,51	0,96	1,41	1,86
y	25,52	0,00	0,00	0,94	0,94	24,58	0,77	1,45	2,14	2,82
z	52,19	2,00	4,00	6,00	8,00	52,19	2,19	4,14	6,09	8,04

A.7 Distance of electrodes to Deep Brain Structures

In this section it is presented the electrodes position and their distance to hippocampus (Hippo.), pallidum (Pall.), thalamus (Thal.), nucleus accubens (N.Acc), amygdala (Amyg.), caudate nucleus (Caud.) and STN.

A.7.1 Parkinson

- Patient 1;

Left Side

Distance of each electrode to the deep brain structures previous segmented, for patient 1 in the left side.

Electrodes	x	y	z	Hippo.	Pall.	Put.	Thal.	N.Acc	Amyg.	Caud.	STN
1	-11,72	26,79	13,61	15,09	12,53	20,09	12,53	25,87	15,04	27,15	7,54
2	-12,66	27,73	15,61	15,77	10,37	18,02	11,51	24,78	15,19	25,09	8,94
3	-13,59	28,66	16,61	16,14	8,76	16,41	11,48	23,92	14,97	23,72	10,19
4	-14,53	29,60	18,61	17,34	6,82	14,48	11,08	23,15	15,74	21,78	12,08

Right Side

Distance of each electrode to the deep brain structures previous segmented, for patient 1 in the right side.

Electrodes	x	y	z	Hippo.	Pall.	Put.	Thal.	N.Acc	Amyg.	Caud.	STN
1	10,78	27,73	14,61	18,23	14,70	22,07	11,29	26,40	18,22	28,77	4,57
2	11,72	28,66	16,61	18,62	12,77	20,21	9,66	25,47	18,41	26,82	6,91
3	12,66	29,60	17,61	18,72	11,23	18,69	9,24	24,70	18,16	25,47	8,52
4	13,59	30,54	19,61	19,60	9,59	17,02	8,39	24,09	18,86	23,64	10,89

- Patient 6;

Left Side

Distance of each electrode to the deep brain structures previous segmented, for patient 6 in the left side.

Electrodes	x	y	z	Hippo.	Pall.	Put.	Thal.	N.Acc	Amyg.	Caud.	STN
1	18,57	57,61	-9,2	15,39	16,60	24,37	16,78	25,82	15,46	30,27	5,69
2	17,63	57,61	-8,2	14,43	15,72	23,53	15,95	25,96	15,13	29,83	6,51
3	19,51	58,55	-6,2	16,49	14,01	22,26	13,99	24,19	16,01	27,45	6,88
4	19,51	59,48	-5,2	16,73	12,70	21,02	13,34	23,23	15,72	26,13	8,12

Right Side

Distance of each electrode to the deep brain structures previous segmented, for patient 6 in the right side.

Electrodes	x	y	z	Hippo.	Pall.	Put.	Thal.	N.Acc	Amyg.	Caud.	STN
1	40,13	51,05	-12,20	12,86	15,82	22,99	15,59	26,04	15,74	30,92	5,17
2	41,07	51,98	-11,20	13,27	14,19	21,42	14,68	24,77	15,29	29,29	4,93
3	42,01	51,98	-10,20	13,17	13,01	20,35	13,68	24,45	15,42	28,31	5,46
4	42,94	52,92	-8,20	14,44	10,97	18,55	12,06	23,23	16,06	26,16	6,11

- Patient 7;

Left Side

Distance of each electrode to the deep brain structures previous segmented, for patient 7 in the left side.

Electrodes	x	y	z	Hippo.	Pall.	Put.	Thal.	N.Acc	Amyg.	Caud.	STN
1	5,92	86,92	14,48	17,39	15,58	23,58	14,28	20,30	18,43	28,56	4,89
2	5,92	87,85	15,48	17,95	14,39	22,43	13,76	25,23	18,31	27,20	5,78
3	4,99	88,79	17,48	18,20	12,16	20,26	12,63	24,20	18,06	25,22	7,86
4	4,99	90,67	19,48	19,85	9,94	18,06	12,40	22,28	18,43	22,50	10,19

Right Side

Distance of each electrode to the deep brain structures previous segmented, for patient 7 in the right side.

Electrodes	x	y	z	Hippo.	Pall.	Put.	Thal.	N.Acc	Amyg.	Caud.	STN
1	29,36	87,85	10,48	17,74	14,29	21,85	16,34	23,69	13,57	28,52	7,61
2	29,36	88,79	11,48	18,63	13,28	20,84	15,90	22,55	13,82	27,18	8,21
3	30,30	89,73	13,48	19,41	11,09	18,73	14,74	21,34	14,25	24,97	9,53
4	31,24	90,67	14,48	19,90	9,49	17,12	14,61	20,41	14,24	23,47	10,99

- Patient 11;

Left Side

Distance of each electrode to the deep brain structures previous segmented, for patient 11 in the left side.

Electrodes	x	y	z	Hippo.	Pall.	Put.	Thal.	N.Acc	Amyg.	Caud.	STN
1	-12,66	25,10	-37,83	15,53	14,68	23,68	13,82	25,71	18,03	27,98	2,31
2	-12,66	26,03	-36,83	16,14	13,60	22,69	12,94	24,82	18,08	26,65	3,62
3	-12,66	26,03	-34,83	16,86	12,91	22,15	10,98	25,02	19,26	25,56	5,10
4	-13,59	26,97	-33,83	16,92	11,38	20,65	10,35	24,29	18,94	24,18	6,42

Right Side

Distance of each electrode to the deep brain structures previous segmented, for patient 11 in the right side.

Electrodes	x	y	z	Hippo.	Pall.	Put.	Thal.	N.Acc	Amyg.	Caud.	STN
1	9,84	27,91	-41,83	15,99	15,62	22,16	17,66	23,98	13,91	28,32	4,89
2	9,84	28,85	-40,83	16,51	14,41	21,05	16,91	22,93	13,86	26,95	4,49
3	10,78	29,78	-38,83	16,56	12,12	19,00	15,35	22,07	14,03	24,86	5,08
4	10,78	29,78	-37,83	16,81	11,52	18,61	14,42	22,05	14,72	24,18	5,11

- Patient 15;

Left Side

Distance of each electrode to the deep brain structures previous segmented, for patient 15 in the left side.

Electrodes	x	y	z	Hippo.	Pall.	Put.	Thal.	N.Acc	Amyg.	Caud.	STN
1	3,57	75,59	21,93	13,17	11,36	11,43	15,17	23,13	11,21	22,41	8,74
2	3,57	78,40	22,93	15,57	8,93	14,87	15,67	20,33	10,76	22,71	11,31
3	2,63	78,40	24,93	15,85	7,15	13,38	14,34	20,49	12,02	21,50	12,33
4	2,63	79,34	25,93	17,02	5,84	12,21	14,25	19,61	12,71	20,16	13,47

Right Side

Distance of each electrode to the deep brain structures previous segmented, for patient 15 in the right side.

Electrodes	x	y	z	Hippo.	Pall.	Put.	Thal.	N.Acc	Amyg.	Caud.	STN
1	27,00	71,84	21,93	14,00	14,39	20,20	15,40	24,05	14,10	26,83	4,20
2	27,00	73,72	22,93	15,36	12,74	18,57	15,06	22,03	13,78	24,78	4,98
3	27,00	74,65	24,93	16,51	11,04	17,06	13,69	20,88	14,64	22,74	5,89
4	27,94	75,59	25,93	16,90	9,39	15,42	13,50	19,92	14,42	21,30	7,48

- Patient 16;

Left Side

Distance of each electrode to the deep brain structures previous segmented, for patient 16 in the left side.

Electrodes	x	y	z	Hippo.	Pall.	Put.	Thal.	N.Acc	Amyg.	Caud.	STN
1	-8,91	28,37	-18,39	15,74	13,80	21,37	13,90	23,75	15,17	28,95	5,42
2	-8,91	29,30	-16,39	16,80	11,85	19,54	12,66	22,33	15,33	26,82	4,80
3	-8,91	30,24	-14,39	18,07	10,01	17,79	11,70	21,03	15,79	24,70	5,14
4	-8,91	31,18	-12,39	19,51	8,34	16,16	11,11	19,89	16,54	22,60	6,28

Right Side

Distance of each electrode to the deep brain structures previous segmented, for patient 16 in the right side.

Electrodes	x	y	z	Hippo.	Pall.	Put.	Thal.	N.Acc	Amyg.	Caud.	STN
1	18,28	26,49	-17,39	16,25	12,68	20,81	10,20	24,06	16,63	26,15	5,73
2	18,28	27,43	-15,39	17,90	11,33	19,47	9,00	22,81	17,21	24,11	6,25
3	19,22	28,37	-14,39	18,37	9,77	17,90	8,89	21,86	16,91	22,60	7,21
4	20,16	29,30	-12,39	19,76	8,11	16,09	8,55	21,00	17,55	20,46	9,15

- Patient 17;

Left Side

Distance of each electrode to the deep brain structures previous segmented, for patient 17 in the left side.

Electrodes	x	y	z	Hippo.	Pall.	Put.	Thal.	N.Acc	Amyg.	Caud.	STN
1	-15,47	32,96	-10,17	15,48	14,75	21,70	14,62	25,20	14,81	29,83	
2	-16,41	33,90	-8,17	16,09	12,36	19,37	13,80	23,46	14,12	27,59	
3	-17,34	33,90	-6,17	16,75	10,36	17,49	12,64	22,67	14,51	25,81	
4	-18,28	34,84	-4,17	17,92	7,98	15,21	12,56	21,22	14,55	23,64	

Right Side

Distance of each electrode to the deep brain structures previous segmented, for patient 17 in the right side.

Electrodes	x	y	z	Hippo.	Pall.	Put.	Thal.	N.Acc	Amyg.	Caud.	STN
1	7,97	31,09	-9,17	18,65	16,99	23,56	13,50	24,70	18,04	29,52	1,39
2	8,91	31,09	-7,17	18,55	14,95	21,60	13,63	23,69	17,60	27,61	1,93
3	8,91	32,02	-5,17	19,74	13,32	20,01	12,89	21,95	17,53	25,42	3,49
4	9,84	32,02	-3,17	20,10	11,41	18,16	11,65	22,23	17,61	23,55	5,63

- Patient 19;

Left Side

Distance of each electrode to the deep brain structures previous segmented, for patient 19 in the left side.

Electrodes	x	y	z	Hippo.	Pall.	Put.	Thal.	N.Acc	Amyg.	Caud.	STN
1	-5,66	32,25	54,43	18,34	14,56	21,97	12,75	24,24	17,55	26,72	4,12
2	-6,60	33,19	56,43	18,27	12,20	19,67	11,82	22,71	16,87	24,57	6,05
3	-6,60	33,19	58,43	19,15	10,91	18,48	10,44	22,12	17,68	22,95	7,43
4	-6,60	34,13	60,43	20,34	9,28	16,89	10,10	20,74	18,10	20,79	9,20

Right Side

Distance of each electrode to the deep brain structures previous segmented, for patient 19 in the right side.

Electrodes	x	y	z	Hippo.	Pall.	Put.	Thal.	N.Acc	Amyg.	Caud.	STN
1	20,59	33,19	54,43	17,38	11,61	19,60	11,85	21,55	17,67	22,94	9,88
2	21,53	33,19	55,43	17,47	10,40	18,46	11,22	21,23	17,71	22,89	11,15
3	22,47	34,13	57,43	18,71	8,50	16,57	11,04	19,82	17,88	20,54	13,42
4	23,40	35,06	59,43	20,16	6,94	14,84	11,36	18,62	18,38	18,23	15,72

A.7.2 Dystonia

- Patient 2;

Left Side

Distance of each electrode to the deep brain structures previous segmented, for patient 2 in the left side.

Electrodes	x	y	z	Hippo.	Pall.	Put.	Thal.	N.Acc	Amyg.	Caud.	STN
1	-17,78	46,68	14,85	18,31	4,70	8,98	18,51	20,27	12,84	20,82	
2	-17,78	47,62	16,85	19,92	3,16	7,54	17,97	20,08	15,02	19,10	
3	-18,71	47,62	18,85	20,68	3,89	7,20	17,45	21,36	16,96	18,67	
4	-18,71	48,56	20,85	22,52	4,55	6,77	17,40	21,59	19,13	17,25	

Right Side

Distance of each electrode to the deep brain structures previous segmented, for patient 2 in the right side.

Electrodes	x	y	z	Hippo.	Pall.	Put.	Thal.	N.Acc	Amyg.	Caud.	STN
1	21,60	41,99	16,85	18,59	4,94	10,49	17,51	19,59	12,53	20,91	
2	22,54	42,93	18,85	19,93	2,71	8,35	17,42	19,60	14,42	19,26	
3	23,47	42,93	20,85	20,63	1,88	7,08	17,07	20,68	16,16	18,61	
4	24,41	43,87	22,85	22,32	2,79	5,57	17,59	21,20	18,26	17,37	

- Patient 3;

Left Side

Distance of each electrode to the deep brain structures previous segmented, for patient 3 in the left side.

Electrodes	x	y	z	Hippo.	Pall.	Put.	Thal.	N.Acc	Amyg.	Caud.	STN
1	-15,47	44,10	20,85	15,81	6,46	12,60	17,21	21,88	11,58	23,18	
2	-16,41	44,10	22,85	16,51	5,13	11,07	16,74	22,12	13,13	22,11	
3	-16,41	43,16	24,85	17,32	4,57	10,77	15,31	22,69	15,32	21,34	
4	-17,34	44,10	26,85	18,94	4,18	8,99	16,12	22,58	16,63	20,02	

Right Side

Distance of each electrode to the deep brain structures previous segmented, for patient 3 in the right side.

Electrodes	x	y	z	Hippo.	Pall.	Put.	Thal.	N.Acc	Amyg.	Caud.	STN
1	28,59	39,41	18,85	16,32	6,66	9,18	20,10	22,25	10,73	22,56	
2	28,59	39,41	21,85	17,44	5,43	7,82	19,27	21,90	12,59	21,08	
3	29,53	39,41	23,85	18,73	6,64	6,50	19,33	22,24	14,60	20,01	
4	29,53	39,41	25,85	20,12	5,73	5,93	18,89	22,26	16,51	18,75	

- Patient 4;

Left Side

Distance of each electrode to the deep brain structures previous segmented, for patient 4 in the left side.

Electrodes	x	y	z	Hippo.	Pall.	Put.	Thal.	N.Acc	Amyg.	Caud.	STN
1	-17,64	42,45	14,78	18,74	8,63	12,77	19,56	23,02	10,55	25,56	
2	-18,58	43,39	16,78	20,12	6,84	10,44	19,34	22,39	12,38	23,86	
3	-18,58	44,33	18,78	21,88	4,93	8,38	18,82	21,55	14,51	21,91	
4	-18,58	45,26	19,78	23,16	4,01	7,08	18,96	20,80	17,71	20,66	

Right Side

Distance of each electrode to the deep brain structures previous segmented, for patient 4 in the right side.

Electrodes	x	y	z	Hippo.	Pall.	Put.	Thal.	N.Acc	Amyg.	Caud.	STN
1	24,55	52,76	15,78	20,69	6,30	8,97	21,61	21,17	12,59	22,33	
2	24,55	53,70	17,78	22,50	5,02	6,94	21,34	20,40	14,69	20,36	
3	24,55	53,70	19,78	23,65	3,89	5,79	20,53	20,47	16,67	18,94	
4	24,55	54,64	21,78	25,60	4,29	4,36	20,68	20,12	18,79	17,09	

- Patient 5;

Left Side

Distance of each electrode to the deep brain structures previous segmented, for patient 5 in the left side.

Electrodes	x	y	z	Hippo.	Pall.	Put.	Thal.	N.Acc	Amyg.	Caud.	STN
1	-12,75	38,27	25,04	17,80	3,94	10,94	14,56	20,75	13,76	19,44	
2	-12,75	39,20	27,04	19,55	2,24	9,67	14,23	20,40	15,54	17,65	
3	-13,68	40,14	28,04	20,47	1,20	8,26	14,91	20,42	16,26	16,75	
4	-14,62	41,08	30,04	22,10	2,73	7,07	15,46	20,96	18,12	15,57	

Right Side

Distance of each electrode to the deep brain structures previous segmented, for patient 5 in the right side.

Electrodes	x	y	z	Hippo.	Pall.	Put.	Thal.	N.Acc	Amyg.	Caud.	STN
1	23,82	29,83	25,04	14,16	8,07	12,31	14,32	24,14	14,42	23,11	
2	23,82	30,77	27,04	16,13	6,65	10,98	13,50	23,67	15,89	21,40	
3	24,75	31,70	28,04	17,42	5,83	9,58	14,12	23,38	16,42	20,30	
4	24,75	32,64	30,04	19,46	5,35	8,73	13,86	23,23	18,15	18,75	

- Patient 9;

Left Side

Distance of each electrode to the deep brain structures previous segmented, for patient 9 in the left side.

Electrodes	x	y	z	Hippo.	Pall.	Put.	Thal.	N.Acc	Amyg.	Caud.	STN
1	-27,66	30,67	-1,22	17,71	5,03	8,61	17,07	22,64	15,44	20,98	
2	-27,66	31,61	0,78	19,90	4,49	6,99	17,13	22,19	17,16	19,08	
3	-28,59	31,61	2,78	21,63	5,93	6,58	17,49	23,23	19,16	18,33	
4	-28,59	31,61	4,78	23,42	7,02	6,87	17,41	23,82	21,13	17,32	

Right Side

Distance of each electrode to the deep brain structures previous segmented, for patient 9 in the right side.

Electrodes	x	y	z	Hippo.	Pall.	Put.	Thal.	N.Acc	Amyg.	Caud.	STN
1	24,84	28,80	-1,22	15,24	7,41	11,08	17,92	23,45	13,17	23,85	
2	24,84	28,80	0,78	16,79	6,54	9,86	17,20	23,57	15,02	22,57	
3	25,78	29,74	2,78	18,91	6,43	8,12	17,98	23,78	16,65	21,28	
4	24,84	29,74	4,78	20,61	5,97	7,47	16,97	23,62	18,57	19,73	

- Patient 10;

Left Side

Distance of each electrode to the deep brain structures previous segmented, for patient 10 in the left side.

Electrodes	x	y	z	Hippo.	Pall.	Put.	Thal.	N.Acc	Amyg.	Caud.	STN
1	-17,34	36,28	11,53	15,74	6,49	12,24	12,24	19,67	10,22	21,80	
2	-17,34	36,28	11,53	16,62	4,73	11,10	15,49	19,78	12,13	20,53	
3	-18,28	37,21	11,53	18,11	3,01	9,08	15,59	19,81	13,84	18,99	
4	-18,28	37,21	17,53	19,30	2,29	8,49	14,81	20,33	15,82	17,96	

Right Side

Distance of each electrode to the deep brain structures previous segmented, for patient 10 in the right side.

Electrodes	x	y	z	Hippo.	Pall.	Put.	Thal.	N.Acc	Amyg.	Caud.	STN
1	21,09	32,53	10,53	13,48	7,74	13,04	15,96	22,63	10,33	23,48	
2	22,03	33,46	12,53	15,00	5,90	10,95	15,64	22,15	11,85	21,76	
3	22,03	34,40	14,53	16,84	4,09	9,31	15,08	21,44	13,59	19,89	
4	22,03	35,34	15,53	18,17	3,01	8,18	15,22	20,76	14,46	18,61	

- Patient 12;

Left Side

Distance of each electrode to the deep brain structures previous segmented, for patient 12 in the left side.

Electrodes	x	y	z	Hippo.	Pall.	Put.	Thal.	N.Acc	Amyg.	Caud.	STN
1	-20,68	41,90	16,92	17,36	4,61	12,58	16,55	22,55	14,75	22,07	
2	-20,68	42,84	18,92	19,31	2,97	11,17	16,27	22,00	16,28	20,12	
3	-20,68	42,84	20,92	20,71	3,28	10,82	15,48	22,43	18,16	18,92	
4	-21,62	43,78	22,92	22,54	4,17	9,54	16,16	22,78	19,74	17,49	

Right Side

Distance of each electrode to the deep brain structures previous segmented, for patient 12 in the right side.

Electrodes	x	y	z	Hippo.	Pall.	Put.	Thal.	N.Acc	Amyg.	Caud.	STN
1	25,26	37,21	16,92	16,58	5,05	11,75	18,34	23,99	11,57	23,10	
2	26,19	37,21	18,92	17,70	3,60	10,10	17,88	24,47	13,29	22,05	
3	26,19	38,15	20,92	19,74	1,92	8,58	17,64	23,89	15,06	20,17	
4	27,13	38,15	22,92	21,12	2,99	7,45	17,68	24,73	16,95	19,42	

- Patient 14;

Left Side

Distance of each electrode to the deep brain structures previous segmented, for patient 14 in the left side.

Electrodes	x	y	z	Hippo.	Pall.	Put.	Thal.	N.Acc	Amyg.	Caud.	STN
1	-11,89	34,90	55,19	19,65	1,43	7,81	15,53	18,95	15,87	16,94	
2	-11,89	34,90	57,19	20,98	1,70	7,35	14,96	19,54	17,83	16,02	
3	-11,89	35,83	59,19	22,94	3,45	6,53	15,53	19,77	19,83	14,66	
4	-12,83	36,77	61,19	24,62	5,80	6,19	16,65	20,89	20,75	14,23	

Right Side

Distance of each electrode to the deep brain structures previous segmented, for patient 14 in the right side.

Electrodes	x	y	z	Hippo.	Pall.	Put.	Thal.	N.Acc	Amyg.	Caud.	STN
1	27,48	25,52	54,19	20,01	2,50	5,45	17,08	17,72	14,18	14,95	
2	27,48	25,52	56,19	21,28	2,89	4,99	16,42	18,26	16,15	13,86	
3	28,42	26,46	58,19	23,41	5,17	4,16	17,31	18,56	18,28	12,32	
4	28,42	26,46	60,19	24,82	6,70	5,33	17,14	19,49	20,25	11,69	

Annex

References

[1] A.C. Guyton and J.E. Hall. *Tratado de Fisiologia médica*. Guanabara Koogan S.A., 10th edition, 2002.

[2] Medtronic. DBS lead model 3389 for deep brain stimulation. Available in http://professional.medtronic.com/pt/neuro/dbs-md/prod/dbs-lead-model-3389/index.htm#.UcW9fE1dbVI, last accessed on June 22, 2013, 2013.

[3] Advanced Neuroscience class of Spring 2000. Pathophysiology. Available in http://www.davidson.edu/academic/psychology/ramirezsite/neuroscience/psy324/stcourchesne/pathophysiology.html, last accessed on June 4, 2013, 2013.

[4] M.F. Penholate P. Brugières J.-M. Gurruchaga M. Shin, J.-P. Lefaucheur and J.-P. Nguyen. Subthalamic nucleus stimulation in parkinson's disease: Postoperative CT—MRI fusion images confirm accuracy of electrode placement using intraoperative multi-unit recording. *Neurophysiol Clin.*, 37(6):457–66, 2007.

[5] John C. Mazziotta Arthur W. Toga. *Brain Mapping: The Methods*. Academic Press, 2nd edition, 2002.

[6] V. Fonov N. Guizard P. Jannin-X. Morandi C. Haegelen, P. Coupé and D. L. Collins. Automated segmentation of basal ganglia and deep brain structures in MRI of parkinson's disease. *International Journal of Computer Assisted Radiology and Surgery*, 8(1):99–110, March 2012.

[7] Brian Patenaude. *Bayesian Statistical Models of Shape and Appearance for Subcortical Brain Segmentation*. PhD thesis, University of Oxford, 2007.

[8] Victor Alves José M. Soares, Paulo Marques and Nuno Sousa. A hitchhiker's guide to diffusion tensor imaging. *Front Neurosci.*, 7(31), March 2013.

[9] Christoph Baecker Christiane Zechlin Lars Friege-Sabine Pohle Henning Stolze, Stephan Klebe and Gunther Deuschl. Prevalence of gait disorders in hospitalized neurological patients. *Movement Disorders*, 20(1), 2005.

[10] Andres M. Lozano and Neil Mahant. Deep brain stimulation surgery for parkinson's disease: mechanisms and consequences. *Parkinsonism & Related Disorders*, 10, Supplement 1(0):S49 – S57, 2004. Proceeding of the 8th International Symposium on the Treatment of Parkinson's Disease.

[11] Peter A. Winkler, Christian Vollmar, Kartik G. Krishnan, Thomas Pfluger, Hartmut Brückmann, and Soheyl Noachtar. Usefulness of 3-D reconstructed images of the human cerebral cortex for localization of subdural electrodes in epilepsy surgery. *Epilepsy Research*, 41(2):169 – 178, 2000.

[12] E.L. So. Integration of EEG,MRI and SPECT in localizing the seizure focus for epilepsy surgery, mayo medical school. *Epilepsia*, 41 Suppl 3:S48–54, 2000.

[13] James X. Tao, Susan Hawes-Ebersole, Maria Baldwin, Sona Shah, Robert K. Erickson, and John S. Ebersole. The accuracy and reliability of 3D CT/MRI co-registration in planning epilepsy surgery. *Clinical Neurophysiology*, 120(4):748 – 753, 2009.

[14] Common neurological disorders. Available in http://www.livestrong.com/article/98547-common-neurological-disorders/#ixzz2RVGzYPX8, last accessed on May 10, 2013, 2013.

[15] S. Palmer F. Beyer J. Minton-A. Marson U. Wieshmann N. Woolacott J. Burch, S. Hinde and M. Soares. The clinical effectiveness and cost-effectiveness of technologies used to visualise the seizure focus in people with refractory epilepsy being considered for surgery: a systematic review and decision-analytical model. *Health Technol Assess*, 16(34):1–157, 2012.

[16] IRCM (International Group of Researchers and Development for Complementary Medicine). Incidence, prevalence and cost of parkinson's disease. Available in http://eng.ircminternational.com/2011/04/incidence-prevalence-and-cost-of-parkinsons-disease/, last accessed on May 10, 2013, 2013.

[17] Current world population. Available in http://geography.about.com/od/obtainpopulationdata/a/worldpopulation.htm, last accessed on May 10, 2013, 2013.

[18] Mandel M Alho EJ Teixeira MJ. Fonoff ET, Campos WK. Bilateral subthalamic nucleus stimulation for generalized dystonia after bilateral pallidotomy. *Mov Disord.*, 27(12):1559–63, Oct 2012.

[19] Dystonia. Available in http://www.netdoctor.co.uk/diseases/facts/dystonia.htm, last accessed on June 5, 2013, 2013.

[20] Eric Bardinet, Manik Bhattacharjee, Didier Dormont, Bernard Pidoux, Grégoire Malandain, Michael Schüpbach, Nicholas Ayache, Philippe Cornu, Yves Agid, and Jérôme Yelnik. A three-dimensional histological atlas of the human basal ganglia. II. Atlas deformation strategy and evaluation in deep brain stimulation for Parkinson disease. *Journal of Neurosurgery*, 110(2):208–219, February 2009.

[21] M. Mallar Chakravarty, Gilles Bertrand, Charles P. Hodge, Abbas F. Sadikot, and D. Louis Collins. The creation of a brain atlas for image guided neurosurgery using serial histological data. *NeuroImage*, 30(2):359 – 376, 2006.

[22] Florent Lalys, Claire Haegelen, Jean-Christophe Ferre, Omar El-Ganaoui, and Pierre Jannin. Construction and assessment of a 3-T MRI brain template. *NeuroImage*, 49(1):345 – 354, 2010.

[23] Parrent AG Peters TM Guo T, Finnis KW. Visualization and navigation system development and application for stereotactic deep-brain neurosurgeries. *Comput Aided Surg.*, 11(5):231–9, 2006.

[24] Han-Joon Kim Daehee Kang Yong Hoon Lim Mi Ryoung Kim Cheolyoung Kim Beom Seok Jeon Sun Ha Paek, Jee-Young Lee and Dong Gyu Kim. Electrode position and the clinical outcome after bilateral subthalamic nucleus stimulation. *J Korean Med Sci.*, 26(10):1344–1355, 2011.

[25] M.J. Koepp and F.G. Woermann. Imaging structure and function in refractory focal epilepsy. *The Lancet Neurology*, 4(1):42 – 53, 2005.

[26] D. Hasboun S.Clémenceau E.Dezamis-S. Lehéricy D.Dormont J.Chiras M.Baulac L. Thivard, C.Adam and S.Dupont. Interictal diffusion MRI in partial epilepsies explored with intracerebral electrodes. *Brain*, 129(Pt 2):375–85, 2006.

[27] Tohru Kamida, Mitsuo Anan, Kazunori Shimotaka, Tatsuya Abe, Minoru Fujiki, and Hidenori Kobayashi. Visualization of subdural electrodes with fusion CT /scan MRI during neuronavigation-guided epilepsy surgery. *Journal of Clinical Neuroscience*, 17(4):511 – 513, 2010.

[28] B.M. Ellingson M. Raghavan S.M. Lew K.M. Schmainda W. Mueller P.S. LaViolette, S.D. Rand. 3D visualization of subdural electrode shift as measured at craniotomy reopening. *Epilepsy Res*, 94(1-2):102–9, 2011.

[29] J.S. Duncan. Imaging in the surgical treatment of epilepsy, university college london institute of neurology. *Nat Rev Neurol*, 6(10):537–50, 2010.

[30] Drug treatments for Parkinson's. Available in http://www.parkinsons.org.uk/about-parkinsons/treating-parkinsons/drugs.aspx, last accessed on May 12, 2013, 2013.

[31] Mendes A. Garrett C. Linhares P. Chamadoira C. Basto M.A. Sousa A. Fonseca R. Vaz R. Rosas, M.J. Results of the first 24 patients with parkinson disease submitted to deep brain stimulation in Hospital S. João from 2002 a 2005. *Sinapse*, 5(2):4–10, November 2005.

[32] F. Kopper J.Volkmann, J. Herzog and G. Deuschl. Introduction to the programming of deep brain stimulators. *Mov Disord.*, 17 Suppl 3:S181–7, 2002.

[33] Fraix V Mendes A Moro E Chabardes S Benabid AL Pollak P, Krack P. Intraoperative micro- and macrostimulation of the subthalamic nucleus in parkinson's disease. *Mov Disord.*, 17 Suppl 3:S155–61, 2002.

[34] D. Hasboun S.Clémenceau E.Dezamis S. Lehéricy D.Dormont J.Chiras M.Baulac L. Thivard, C.Adam and S.Dupont. The tremor network targeted by successful VIM deep brain stimulation in humans. *Neurology*, 78(11):787–95, 2012.

[35] Madhusudanan M. Dystonia : emerging concepts in pathophysiology. *Neurol India.*, 47(4):263–7, 1999.

[36] J. Müller T. Trottenberg G.H. Schneider W. Poewe W. Eisner A. Wolters J.U. Müller G. Deuschl M.O. Pinsker I.M. Skogseid G.K. Roeste J. Vollmer-Haase A. Brentrup M. Krause

V. Tronnier A. Schnitzler J. Voges G. Nikkhah J. Vesper M. Naumann A. Kupsch, R. Benecke and J. Volkmann. Pallidal deep-brain stimulation in primary generalized or segmental dystonia. *N Engl J Med*, 355:1978–90, 2006.

[37] Krauss J.K Capelle, H.-H. Neuromodulation in dystonia: Current aspects of deep brain stimulation. *Neuromodulation*, 12(1):8–21, January 2009.

[38] Kai Bötzel Joao Paulo Cunha Verena Rozanski, Christian Vollmar. Connectivity patterns of pallidal dbs (deep brain stimulation) electrodes in focal dystonia. In *International Conference on Deep Brain Stimulation*, 2013.

[39] Arthur W. Toga. *Brain Warping*. Academic Press, 1st edition, 1998.

[40] X. Han Y. Bai and J. L. Prince. Super-resolution reconstruction of MR brain images. In *Proc. of 38th Annual Conference on Information Sciences and Systems*, 2004.

[41] N. Moore J. W. Chi, M. Brady and J. A. Schnabel. Fusion of perpendicular anisotropic MRI sequences. In *Biomedical Imaging: From Nano to Macro, 2011 IEEE International Symposium on*, pages 1455 – 1458, 2011.

[42] E. Yacoub G. Sapiro N. Harel I. Aganj, C. Lenglet. A 3D wavelet fusion approach for the reconstruction of isotropic-resolution MR images from orthogonal anisotropic-resolution scans. *Magn Reson Med*, 67(4):1167–72, 2012.

[43] Rashima Mahajana Pravat K. Mandala and Ivo D. Dinovc. Structural brain atlases: Design, rationale, and applications in normal and pathological cohorts. *Journal of Alzheimer's Disease*, 31:1–20, 2012.

[44] Joseph T. Devlin and Russell A. Poldrack. In praise of tedious anatomy. *NeuroImage*, 37(4):1033–1041, Oct 2007.

[45] 3D Slicer. Available in http://www.slicer.org/, last accessed on May 12, 2013, 2013.

[46] Pedro B.P. Amaral. Aplicação para visualização multimodal e manipulação de dados de electrocorticografia. Master's thesis, Universidade de Aveiro, 2008.

[47] BrainVoyager. Available in http://www.brainvoyager.com/, last accessed on May 12, 2013, 2013.

[48] Osirix. Available in http://www.osirix-viewer.com/, last accessed on May 12, 2013, 2013.

[49] MRIcro. Available in http://www.mccauslandcenter.sc.edu/mricro/, last accessed on May 12, 2013, 2013.

[50] FSL. Available in http://www.fmrib.ox.ac.uk/fsl/, last accessed on May 10, 2013, 2013.

[51] SPM8. Available in http://www.fil.ion.ucl.ac.uk/spm/software/spm8/, last accessed on May 12, 2013, 2013.

[52] *Understanding MRI: An interactive guide to MRI principles and applications CD-ROM*. Philips Medical Systems, Andover, MA 2001.

[53] E.M.Leidholdt J.T.Bushberg, J.A.Seibert and J. M. Boone. *The Essential Physics of Medical Imaging*. Lippincott Williams & Wilkins, 2nd edition, 2002.

[54] Michael Samuel Chris Clough Richard P. Selway Ruth L. O'Gorman, Josef M. Jarosz and Keyoumars Ashkan. CT/MR image fusion in the postoperative assessment of electrodes implanted for deep brain stimulation. *Stereotact Funct Neurosurg*, (87):205–10, 2009.

[55] S.H.Paek Y. H. Lim M. R. Kim C. Kim J.-Y. Lee, B. S. Jeon. Reprogramming guided by the fused images of MRI and CT in subthalamic nucleus stimulation in parkinson disease. *Clin Neurol Neurosurg.*, 112(1):47–53, 2010.

[56] A. Bari E. Behnke A. Frew I. Gevorkyan N. Pouratian M. Sedrak, A. Gorgulho and A. De-Salles. Diffusion tensor imaging (DTI) and colored fractional anisotropy (FA) mapping of the subthalamic nucleus (STN) and the globus pallidus interna (GPi). *Acta Neurochir (Wien)*, 152(12):2079–2084, 2010.

[57] W.-Z. Zhu C.-Y. Wang J.-W. Hu H.-G.Shu, J.-P. Qi and D.-Y Feng. Diffusion tensor imaging study of parkinson disease. *Chinese Journal of Medical Imaging Technology*, (4), 2010.

[58] K. L. Miller S.Deoni-S. Jbabdi P. M. Matthews R. A. Menke, J. Scholz and M. Zarei. MRI characteristics of the substantia nigra in parkinson's disease: A combined quantitative T1 and DTI study. *NeuroImage*, 47(2):435 – 441, 2009.

[59] Booij J. Nederveen A.J. Dijk J.M. Zoons, E. and M.A.J. Tijssen. Structural, functional and molecular imaging of the brain in primary focal dystonia-A review. *NeuroImage*, 56(3):1011–1020, June 2011.

[60] Vladimir Fonov Jens Pruessner-Montserrat Robles D. Louis Collins Pierrick Coupé, José V. Manjón. Patch-based segmentation using expert priors: Application to hippocampus and ventricle segmentation. *NeuroImage*, 54:940–954, 2011.

[61] FMRIB's integrated registration and segmentation tool. Available in http://fsl.fmrib.ox.ac.uk/fsl/fsl-4.1.9/first/index.html, last accessed on May 10, 2013, 2013.

[62] Kennedy DN Jenkinson M. Patenaude B, Smith SM. A bayesian model of shape and appearance for subcortical brain segmentation. *Neuroimage.*, 56(3):907–22, 2011.

[63] Stephen M. Smith. Fast robust automated brain extraction. *Human Brain Mapping*, (17):143–155, 2012.

[64] Nathan D. Cahill. Normalized measures of mutual information with general definitions of entropy for multimodal image registration. In *WBIR'10 Proceedings of the 4th international conference on Biomedical image registration*, pages 258–268. Springer-Verlag, 2010.

[65] Functional Imaging Laboratory. Spatial pre-processing. Available in http://www.fil.ion.ucl.ac.uk/spm/doc/manual/spatial.htm, last accessed on June 7, 2013, 2013.

[66] Mattay VS Weinberger DR Levin RL Frank JA Ostuni JL, Santha AK. Analysis of interpolation effects in the reslicing of functional MR images. *J Comput Assist Tomogr.*, 21(5):803–10, 1997.

[67] Pierre-Michel Llorca Philippe Derost Jean-Jacques Lemaire Isabelle Chereau-Boudet Ingrid de Chazeron Audrey Schmitt Bénédicte Ballanger Emmanuel Broussolle Franck Durif Miguel Ulla, Stéphane Thobois. Contact dependent reproducible hypomania induced by deep brain stimulation in Parkinson's disease: clinical, anatomical and functional imaging study. *J Neurol Neurosurg Psychiatry*, (82):607–614, 2011.

[68] Thobois S. Lemaire-J.-J. Schmitt A. Derost-P. Broussolle E. Llorca-P.-M. Ulla, M. and F. Durif. Manic behaviour induced by deep-brain stimulation in Parkinson's disease: Evidence of substantia nigra implication? *Journal of Neurology, Neurosurgery and Psychiatry*, 77(12):1363–1366, December 2006.

[69] Mark K. Lyons. Deep brain stimulation: Current and future clinical applications. *Mayo Clin Proc.*, 86(7):662–672, July 2011.

[70] Grace AA. Ewing SG. Deep brain stimulation of the ventral hippocampus restores deficits in processing of auditory evoked potentials in a rodent developmental disruption model of schizophrenia. *Schizophr Res.*, 143(2-3):377–83, December 2012.

[71] Jean-Philippe Langevin. The amygdala as a target for behavior surgery. 3 Suppl S1:S40–6, 2012.